



저작자표시-비영리-변경금지 2.0 대한민국

이용자는 아래의 조건을 따르는 경우에 한하여 자유롭게

- 이 저작물을 복제, 배포, 전송, 전시, 공연 및 방송할 수 있습니다.

다음과 같은 조건을 따라야 합니다:



저작자표시. 귀하는 원저작자를 표시하여야 합니다.



비영리. 귀하는 이 저작물을 영리 목적으로 이용할 수 없습니다.



변경금지. 귀하는 이 저작물을 개작, 변형 또는 가공할 수 없습니다.

- 귀하는, 이 저작물의 재이용이나 배포의 경우, 이 저작물에 적용된 이용허락조건을 명확하게 나타내어야 합니다.
- 저작권자로부터 별도의 허가를 받으면 이러한 조건들은 적용되지 않습니다.

저작권법에 따른 이용자의 권리는 위의 내용에 의하여 영향을 받지 않습니다.

이것은 [이용허락규약\(Legal Code\)](#)을 이해하기 쉽게 요약한 것입니다.

[Disclaimer](#)

Dissertation for the degree of Doctor of Philosophy

The Multi-target Approach of Marine
Polyphenolic Compounds Against SARS-
CoV-2; Attenuates SARS-CoV-2 Cell Entry,
Proliferation, and Subsequent Cytokine Storm
in the Host.

Dineth Pramuditha Nagahawatta

Department of Marine Life Sciences

The Graduate School

Jeju National University

August, 2023

**The multi-target approach of marine polyphenolic compounds
against SARS-CoV-2; attenuates SARS-CoV-2 cell entry,
proliferation, and subsequent cytokine storm in the host.**

D.P. Nagahawatta

(Supervised by Professor You-Jin Jeon)

A thesis submitted in partial fulfilment of the requirement for the degree
of

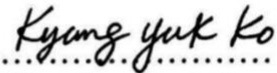
DOCTOR OF PHILOSOPHY

August 2023

The thesis has been examined and approved by



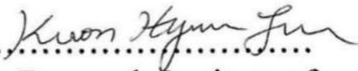
.....
Thesis director, Young Sang Kim (PhD), Research Professor of Marine life
sciences, Jeju National University



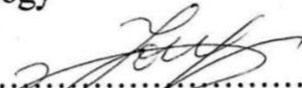
.....
Kyung Yuk Ko (PhD), Research Professor of Marine life sciences, Jeju
National University



.....
Fengqi Yang (PhD), Researcher of Marine life sciences, Jeju National
University



.....
Hyung-Jun Kwon (PhD), Senior Researcher of Korea Research Institute of
Bioscience and Biotechnology



.....
You-Jin Jeon (PhD), Professor of Marine Life Sciences, Jeju National
University

2023/08

Date

Department of Marine Life Sciences

GRADUATE SCHOOL

JEJU NATIONAL UNIVERSITY



Contents

Summary	vi
List of figures	ix
List of Tables	xviii
Part I: Polyphenolic Compounds Isolated from Marine Algae Attenuate the Replication of SARS-CoV-2 in the Host Cell through a Multi-Target Approach of 3CL ^{pro} and PL ^{pro}	1
1. Introduction.....	2
2. Methods and Materials.....	6
2.1 Chemicals and reagents	6
2.2 Preparation of Receptors	6
2.3. Preparation of ligands	7
2.4 Molecular docking	9
2.5 Sample collection and extraction	9
2.6 Isolation of Dieckol.....	11
2.7 Isolation of Eckmaxol	12
2.8 3CL ^{pro} <i>in-vitro</i> cleavage inhibition assay	14
2.9 Isolation of Ishophloroglucin A (IPA) and Diphlorethohydroxycarmalol (DPHC)	14
2.10 PL ^{pro} <i>in-vitro</i> cleavage inhibition assay	17
2.11 Enzyme Kinetic Evaluation.....	17
2.12 Cell-based inhibition assay	18
2.12.1 Cell culture maintenance	18
2.12.2 Cell-based in-vitro evaluation	18

2.13 Cytopathic Effect (CPE) Reduction Evaluation.....	21
2.14 Statistical analysis	21
3. Results.....	22
3.1 Receptor and ligand preparation	22
3.1.1. Structure of 3CL ^{pro} receptor protein preparation.....	22
3.1.2 Structure of PL ^{pro} receptor protein preparation	24
3.1.3 Ligand preparation.....	26
3.2 Molecular docking	28
3.2.1. 3CL ^{pro} enzyme	30
3.2.2. PL ^{pro} enzyme	34
3.3 In-vitro inhibition of marine algal compounds	38
3.4 Line-weaver Burk Plot	41
3.5 Cell-Based Inhibition of 3CL ^{pro} and PL ^{pro}	43
3.6 Cytopathic Effect (CPE) Reduction potential	45
4. Discussion.....	47
5. Conclusion	50
Part II: Polyphenolic Compounds Isolated from Marine Algae inhibit the SARS-CoV-2 cell entry mechanism via disturbing SARS-CoV-2 spike proteins and angiotensin converting enzyme interaction.....	51
1. Introduction	52
2. Methods and Materials.....	56
2.1 Chemicals and reagents.....	56
2.2 Preparation of Receptors	56
2.3. Preparation of ligands	57
2.4 Molecular docking	58
2.5 Sample collection and extraction	58

2.6	Inhibition assay in binding of ACE-2 receptor and SARS-CoV-2 spike protein	58
2.7	SARS-CoV-2 pseudovirus production	59
2.7.1	Cell culture	59
2.7.2	Gene transfection for the development of pseudovirus	59
2.7.3	Evaluating of the titter of the pseudovirus	62
2.7.4	Infection of the pseudovirus to the HEK293T-ACE-2 cells	64
2.8	In-vivo evaluation of the inhibitory potential of polyphenolic compounds against SARS-CoV-2 cell entry	64
2.8.1	RNA extraction, reverse transcription and RT-qPCR	66
2.9	Statistical analysis	66
3.	Results	67
3.1	Receptor and ligand preparation	67
3.1.1.	Structure of ACE-2 receptor protein preparation	67
3.1.2	Ligand preparation	69
3.2	Molecular docking	69
3.2.1.	ACE-2 enzyme	71
3.3	In-vitro inhibition of marine algal compounds	74
3.4	Inhibition of SARS-CoV-2 pseudovirus cell entry	75
3.4.1	Determination of pseudovirus production and virus titter	75
3.5	Inhibition of SARS-CoV-2 pseudovirus cell entry in in-vivo	78
4.	Discussion	80
5.	Conclusion	85
Part III: Polyphenolic Compounds Isolated from Marine Algae inhibit the SARS-CoV-2 spike protein-induced cytokine storm in the host		86
1.	Introduction	87
2.	Methods and Materials	89
2.1	Chemicals and reagents	89
2.2	Cell culture and maintenance	89

2.3 Maintenance of zebrafish and larvae.....	90
2.4 Gene transfection to the A549 and HEK293T cells.....	90
2.5 Determination of Cell Viability	91
2.6 Evaluation of the Production of Cytokines	91
2.7 Gene expression analysis	91
2.8 Western blot evaluation.....	94
2.9 Spike protein microinjection to zebrafish	95
2.10 Neutral red staining	95
2.11 Sudan black staining	95
2.12 Statistical analysis	96
3. Results.....	97
3.1 Pro-inflammatory cytokine production in SARS-CoV-2 spike protein transfected A549 and HEK293T cells	97
3.2 Pro-inflammatory cytokine production in SARS-CoV-2 spike protein transfected A549 and HEK293T cells	100
3.3 Evaluation of SARS-CoV-2 spike protein-induced protein expression of NF- κ B and MAPK signalling pathways.....	105
3.4 Evaluation of the effect of SARS-CoV-2 spike protein structure and ACE-2 expression in host cell to stimulatory potential of spike protein to develop inflammatory cytokines.....	108
3.5 Polyphenolic compounds inhibited the inflammatory cytokine production in the SARS-CoV-2 spike protein-induced A549 and MHS cells	110

3.6 Polyphenolic compounds inhibited the inflammatory cytokine and chemokine gene expression in the SARS-CoV-2 spike protein-induced A549 and MHS cells	111
3.7 Polyphenolic compounds inhibited the inflammatory cytokine and chemokine protein expression in the SARS-CoV-2 spike protein-induced A549 and MHS cells	113
3.8 In-vivo evaluation of the anti-inflammatory potential of polyphenolic compounds against SARS-CoV-2 spike protein-induced inflammation	116
4. Discussion	122
5. Conclusion	127
References	128
Concluding remarks	134
Acknowledgment	136
요약	137

Summary

Global health concerns have been raised by the most recent coronavirus pandemic of 2019 (COVID-19) brought on by the SARS-CoV-2 virus. The coronavirus had notable distinctions from other respiratory infections like influenza, adenovirus, and avian influenza and the severe acute respiratory syndrome coronavirus (SARS-CoV), Middle East respiratory syndrome coronavirus (MERS-CoV), and SARS-CoV. SARS-CoV-2's real mode of infection still needs to be fully understood, including why humans are the virus' primary host and how it bypasses the innate immune system. The viral entry mechanism has been found, and it involves respiratory droplets from sneezing and coughing to enter the body through the respiratory system.

SARS-CoV-2 consists of a protein capsid covered by glycoprotein with anchored spike proteins. These spike proteins initiate the viral entry into target cells. Entry of SARS-CoV-2 into the host cell is an essential factor in determining infectivity and pathogenesis. SARS-CoV-2 spike protein initially binds to the cell surface receptor called angiotensin-converting enzyme 2 (ACE-2), known as viral attachment. Subsequently, it enters the endosome, and finally viral membrane fuses with the lysosomal membrane. Thus, if some particular compound can interfere with the interaction of ACE-2: RBD of the spike protein of SARS-CoV-2, it has the potential for use against the SARS-CoV-2 cell entry mechanism.

Among the excellent drug targets of SARS-CoV-2 are its proteases (NSP 3 and NSP 5), which play a vital role in polyprotein processing, giving rise to functional non-structural proteins essential for viral replication and survival. Nsp5 (also known as 3CLpro) hydrolyzes replicase polyprotein (1ab) at eleven different sites. The resulting products are necessary for the survival and replication of the virus in the host cell. The

papain-like protease (PLpro) cleaves the viral polyprotein and reverses inflammatory and anti-viral ubiquitin-like ISG15 protein modifications. Therefore, drugs targeting SARS-CoV-2 PLpro are effective as treatments or prophylaxis for covid-19, reducing viral load and reinstating innate immune responses.

The SARS-CoV-2 infection and replication are complex mechanisms, suggesting that COVID-19 therapy with a multi-targeting approach is the right way. Bioactive components from marine algae have provided new insight into natural product research. The present study aims to inhibit SARS-CoV-2 through 3CLpro, PLpro, and SARS-CoV-2 cell entry mechanisms by natural products isolated from marine algae. Molecular docking was utilized to initially screen selected natural products based on the 3CLpro, PLpro, and ACE-2 protein structures. Moreover, the resulting compounds were isolated and used for biological assays to confirm the inhibition activity. Initially, the inhibitory potential of compounds against the viral cell entry mechanism was evaluated using an in-vitro assay kit. Then these results were further confirmed using a cell-based assay. Here, authors developed an ACE-2 overexpressed HEK293T cell and SARS-CoV-2 pseudovirus that consists of spike protein on the viral envelope and mCherry and firefly luciferase genes. The author introduced a rapid method to calculate the viral titer using an absolute quantification method in qPCR. These results were further solidified using a zebrafish in-vivo model. The inhibitory potential of these compounds against 3CLpro and PLpro was also evaluated using an in-vitro assay kit and further confirmed through a novel cell-based rapid method. Finally, the inhibitory potential of these compounds against spike protein-induced inflammation was also evaluated using in-vitro and in-vivo models. In this study, we report for the first time the potential of polyphenolic compounds isolated from brown marine algae as inhibitors against SARS-CoV-2 through the main

three drug targets. These results show that IPA, Dieckol, DPHC, and Eckmaxol showed remarkable inhibitory potential.

Keywords: SARS-CoV-2; 3CL^{pro}; PL^{pro}; ACE-2; Marine algae, Molecular docking; inflammation.

List of figures

- Fig. 1. Chemical structures of ligand.**8
- Fig. 2. Extraction and isolation procedure of Ishophloroglucinol A (IPA) and Diploretrohydroxycarmalol (DPHC) from *Ishige okamurae*,** (a) Extraction protocol, (b) High Performance Liquid Chromatography (HPLC) analysis of IPA, and (c) DPHC.16
- Fig. 3. Extraction and isolation procedure of *Ecklonia cava*.** (a) Extraction protocol and (b) High Performance Liquid Chromatography (HPLC) analysis of Dieckol.11
- Fig. 4. Extraction and isolation procedure of *Ecklonia maxima*.** (a) Extraction protocol and (b) High Performance Liquid Chromatography (HPLC) analysis of Eckmaxol.13
- Fig. 5. Cell based 3CL^{pro} and PL^{pro} cleavage inhibition assay.** (a) principle of the assay, (b) Plasmid that contain 3CL^{pro} and PL^{pro} genes, and (c) vector that contain firefly Luciferase and renilla luciferase.20
- Fig. 6. Receptor preparation of 3CL^{pro}.** a) Surface representation 3CL^{pro} and N3 inhibitor ligand complex 3CL^{pro} receptor protein is in yellow color and N3 inhibitor in red color. b) Cartoon representation of 3CL^{pro} and N3 inhibitor ligand complex. 3CL^{pro} receptor protein is in yellow color and N3 inhibitor is in red color. c) 2D representation of ligand interaction between 3CL^{pro} and N3 inhibitor. d) 3D representation of ligand interaction between 3CL^{pro} and N3 inhibitor. e) Prepared active site of 3CL^{pro}.23
- Fig. 7. Receptor preparation of PL^{pro}.** a) Surface representation PL^{pro} and GRL0617 inhibitor ligand complex 3CL^{pro} receptor protein is in yellow color and GRL0617 inhibitor in red color. b) Cartoon representation of PL^{pro} and GRL0617 inhibitor ligand complex. PL^{pro} receptor protein is in yellow color and GRL0617 inhibitor is in red color.

c) 2D representation of ligand interaction between PL^{pro} and GRL0617 inhibitor. d) 3D representation of ligand interaction between PL^{pro} and GRL0617 inhibitor. e) Prepared active site of PL^{pro}.25

Fig. 8. Three-dimensional structures of prepared ligand using Discovery studio..27

Fig. 9. In-silico analysis of 3CL^{pro} with Ishophloroglucinol A (IPA). a) 3D representation of docking pose of IPA with 3CL^{pro}. b) Cartoon representation of docking pose of IPA with 3CL^{pro}. c) 2D representation of Ligand interaction of IPA with 3CL^{pro}. d) 3D representation of Ligand interaction of IPA with 3CL^{pro}.30

Fig 10. In-silico analysis of 3CL^{pro} with Diphlorethohydroxycarmalol (DPHC), a) 3D representation of docking pose of DPHC with 3CL^{pro}. b) Cartoon representation of docking pose of DPHC with 3CL^{pro}. c) 2D representation of Ligand interaction of DPHC with 3CL^{pro}. d) 3D representation of Ligand interaction of DPHC with 3CL^{pro}.31

Fig. 11. In-silico analysis of 3CL^{pro} with Dieckol. a) 3D representation of docking pose of Dieckol with 3CL^{pro}. b) Cartoon representation of docking pose of Dieckol with 3CL^{pro}. c) 2D representation of Ligand interaction of Dieckol with 3CL^{pro}. d) 3D representation of Ligand interaction of Dieckol with 3CL^{pro}.32

Fig. 12. In-silico analysis of 3CL^{pro} with Eckmaxol. a) 3D representation of docking pose of Eckmaxol with 3CL^{pro}. b) Cartoon representation of docking pose of Eckmaxol with 3CL^{pro}. c) 2D representation of Ligand interaction of Eckmaxol with 3CL^{pro}. d) 3D representation of Ligand interaction of Eckmaxol with 3CL^{pro}.33

Fig. 13. In-silico analysis of PL^{pro} with Ishophloroglucinol A (IPA). a) 3D representation of docking pose of IPA with PL^{pro}. b) Cartoon representation of docking pose of IPA with PL^{pro}. c) 2D representation of Ligand interaction of IPA with PL^{pro}. d) 3D representation of Ligand interaction of IPA with PL^{pro}.34

Fig. 14. In-silico analysis of PL^{pro} with Diphlorethohydroxycarmalol (DPHC),	
a) 3D representation of docking pose of DPHC with PL ^{pro} .	
b) Cartoon representation of docking pose of DPHC with PL ^{pro} .	
c) 2D representation of Ligand interaction of DPHC with PL ^{pro} .	
d) 3D representation of Ligand interaction of DPHC with PL ^{pro} .	35
Fig. 15. In-silico analysis of PL^{pro} with Dieckol.	
a) 3D representation of docking pose of Dieckol with PL ^{pro} .	
b) Cartoon representation of docking pose of Dieckol with PL ^{pro} .	
c) 2D representation of Ligand interaction of Dieckol with PL ^{pro} .	
d) 3D representation of Ligand interaction of Dieckol with PL ^{pro} .	36
Fig. 16. In-silico analysis of PL^{pro} with Eckmaxol.	
a) 3D representation of docking pose of Eckmaxol with PL ^{pro} .	
b) Cartoon representation of docking pose of Eckmaxol with PL ^{pro} .	
c) 2D representation of Ligand interaction of Eckmaxol with PL ^{pro} .	
d) 3D representation of Ligand interaction of Eckmaxol with PL ^{pro} .	37
Fig. 17. In-vitro evaluation of 3CL^{pro}. Effect of (a) Ishophloroglucin A (IPA), (b) Dieckol, (c) Eckmaxol, and (d) Diphlorethohydroxycarmalol (DPHC) on the activity of SARS-CoV-2 3CL ^{pro} and enzyme kinetic activity.	39
Fig. 18. In-vitro evaluation of PL^{pro}. Effect of (a) Ishophloroglucin A (IPA), (b) Dieckol, (c) Eckmaxol, and (d) Diphlorethohydroxycarmalol (DPHC) on the activity of SARS-CoV-2 PL ^{pro} and enzyme kinetic activity.	40
Fig. 19. Line-weaver Burk plot of (a) Ishophloroglucin A (IPA), (b) Diphlorethohydroxycarmalol (DPHC), (c) Eckmaxol, and (d) Dieckol on the activity of SARS-CoV-2 3CL ^{pro} .	41
Fig. 20. Line-weaver Burk plot of (a) Ishophloroglucin A (IPA), (b) Diphlorethohydroxycarmalol (DPHC), (c) Eckmaxol, and (d) Dieckol on the activity of SARS-CoV-2 PL ^{pro} .	42

Fig 21. Cell-based 3CL^{pro} inhibitory activity of (a) Ishophloroglucin A (IPA), (b) Dieckol, (c) Eckmaxol, and (d) Diphlorethohydroxycarmalol (DPHC) **and Cell-based PL^{pro} inhibitory activity of** (e) Ishophloroglucin A (IPA), (f) Dieckol, (g) Eckmaxol, and (h) Diphlorethohydroxycarmalol (DPHC).44

Fig 22. Inhibitory activity of Cytopathic effect induced by SARS-CoV-2 (a) Ishophloroglucin A (IPA), (b) Dieckol, (c) Eckmaxol, and (d) Diphlorethohydroxycarmalol (DPHC).46

Fig. 1. Experimental procedure of SARS-CoV-2 pseudovirus production.61

Fig. 2. Experimental procedure for evaluating virus titter. (a) dilution series of mCherry gene and (b) standard curve of mCherry gene, and (c) standard curve.63

Fig. 3. Experimental procedure of in-vivo evaluation of SARS-CoV-2 pseudovirus cell entry......65

Fig. 4. Receptor preparation of ACE-2. a) Surface representation ACE-2: RBD of SARS-CoV-2 spike protein complex ACE-2. ACE-2 receptor protein is in yellow colour and RBD of SARS-CoV-2 is in red colour. b) Cartoon representation of ACE-2: RBD of SARS-CoV-2 spike protein complex. ACE-2 receptor protein is in yellow colour and RBD of SARS-CoV-2 is in red colour. c) Prepared active site of ACE-2.68

Fig. 5. In-silico evaluation of 3CL^{pro} with Ishophloroglucinol A (IPA). a) 3D representation of docking pose of IPA with ACE-2. b) Cartoon representation of docking pose of IPA with ACE-2. c) 2D representation of Ligand interaction of IPA with ACE-2. d) 3D representation of Ligand interaction of IPA with ACE-2.....71

Fig. 6. In-silico evaluation of 3CL^{pro} with Diphlorethohydroxycarmalol (DPHC) .a) 3D representation of docking pose of DPHC with ACE-2. b) Cartoon representation of docking pose of DPHC with ACE-2. c) 2D representation of Ligand interaction of DPHC with ACE-2. d) 3D representation of Ligand interaction of DPHC with ACE-2.....72

Fig. 7. In-silico evaluation of 3CL^{Pro} with Eckmaxol. a) 3D representation of docking pose of Eckmaxol with ACE-2. b) Cartoon representation of docking pose of Eckmaxol with ACE-2. c) 2D representation of Ligand interaction of Eckmaxol with ACE-2. d) 3D representation of Ligand interaction of Eckmaxol with ACE-2. 73

Fig. 8. In-vitro inhibition assay of the interaction between ACE-2: SARS-CoV-2 a) Ishophloroglucin A and b) Diphlorethohydroxycarmalol (DPHC), and c) Eckmaxol. .. 74

Fig. 9. Optimization of pseudovirus production. 75

Fig. 10. Evaluation of the cell entry mechanism of SARS-CoV-2 pseudovirus. (a) Optimization of the SARS-CoV-2 pseudovirus mCherry fluorescence expression time, (b) Inhibitory potential of Ishophloroglucin A (IPA), Diphlorethohydroxycarmalol (DPHC), Eckmaxol, and (c) fluorescence quantification. Triplicate experiments were used to evaluate the data and the mean value is expressed with \pm SD. * $p < 0.05$, ** $p < 0.01$, against spike-treated group or ## $p < 0.01$, against control (ANOVA, Duncan's multiple range test). 77

Fig. 11. In-vivo evaluation of SARS-CoV-2 pseudovirus cell entry. (a) ACE-2 expression of zebrafish with age, (b) optimization of the effect of viral media amount for mCherry expression in zebrafish, and (c) inhibitory potential of Ishophloroglucin A (IPA), Diphlorethohydroxycarmalol (DPHC), and Eckmaxol, against SARS-CoV-2 pseudovirus cell entry. Triplicate experiments were used to evaluate the data and the mean value is expressed with \pm SD. * $p < 0.05$, ** $p < 0.01$, against spike-treated group or ## $p < 0.01$, against control (ANOVA, Duncan's multiple range test). 79

Fig. 1. Confirmation of the SARS-CoV-2 spike protein transfection. (a) GFP expression in SARS-CoV-2 spike protein transfected A549 (S-A549) and HEK293T (S-HEK293T) cells, (b) Western blot evaluation of SARS-CoV-2 spike protein in A549 and HEK293T cells. 97

Fig. 2. Evaluation of inflammatory cytokine production in SARS-CoV-2 spike protein transfected A549 (S-A549) and HEK293T (S-HEK293T) cell. (a) inflammatory cytokine production in S-A549 cells, (c) inflammatory cytokine production in S-HEK-293T cells, (c) inflammatory cytokine production in S-A549 cell media-induced MHS cells, and (d) inflammatory cytokine production in S-HEK293T cell media-induced RAW 264.7 cells.99

Fig. 3. Evaluation of SARS-CoV-2 spike protein-induced cytotoxicity in A549, MHS, HEK293T, and ACE-2 over-expressed HEK293T (HEK293T-ACE-2). Triplicate experiments were used to evaluate the data, and the mean value is expressed with \pm SD. * $p < 0.05$, ** $p < 0.01$, against spike-treated group or ## $p < 0.01$, against control (ANOVA, Duncan's multiple-range test) 101

Fig. 4. Evaluation of SARS-CoV-2 spike protein-induced pro-inflammatory cytokine and chemokine gene expression in A549 cells. (a) SARS-CoV-2 spike protein-induced inflammatory cytokine gene expression from different spike protein concentrations at 4hr and 24hr in A549 cells, (b) SARS-CoV-2 spike protein-induced inflammatory chemokine gene expression from different spike protein concentrations at 4hr and 24hr in A549 cells. Triplicate experiments were used to evaluate the data, and the mean value is expressed with \pm SD. * $p < 0.05$, ** $p < 0.01$, against spike-treated group or ## $p < 0.01$, against control (ANOVA, Duncan's multiple-range test). 102

Fig. 5. Evaluation of SARS-CoV-2 spike protein-induced pro-inflammatory cytokine and chemokine gene expression in MHS cells. (a) SARS-CoV-2 spike protein-induced inflammatory cytokine gene expression from different spike protein concentrations at 4hr and 24hr in MHS cells, (b) SARS-CoV-2 spike protein-induced inflammatory chemokine gene expression from different spike protein concentrations at 4hr and 24hr in MHS cells. Triplicate experiments were used to evaluate the data, and the

mean value is expressed with \pm SD. * $p < 0.05$, ** $p < 0.01$, against spike-treated group or ## $p < 0.01$, against control (ANOVA, Duncan's multiple-range test)..... 104

Fig. 6. Evaluation of SARS-CoV-2 spike protein-induced protein expression in NF- κ B and MAPK signalling pathways at different time points in A549 cells. Triplicate experiments were used to evaluate the data, and the mean value is expressed with \pm SD. * $p < 0.05$, ** $p < 0.01$, against spike-treated group or ## $p < 0.01$, against control (ANOVA, Duncan's multiple-range test)..... 106

Fig. 7. Evaluation of SARS-CoV-2 spike protein-induced protein expression in NF- κ B and MAPK signalling pathways at different time points in MHS cells. Triplicate experiments were used to evaluate the data, and the mean value is expressed with \pm SD. * $p < 0.05$, ** $p < 0.01$, against spike-treated group or ## $p < 0.01$, against control (ANOVA, Duncan's multiple-range test)..... 107

Fig. 8. Evaluation of the effect of SARS-CoV-2 spike protein structure and ACE-2 expression in host cell to stimulatory potential of spike protein to develop inflammatory cytokines. (a) SARS-CoV-2 spike protein-induced inflammatory cytokine production HEK-293T and ACE-2 over-expressed HEK293T (HEK293T-ACE-2) and (b) inflammatory cytokine production in A549 cells induced by heat-inactivated spike protein (HI spike) and spike protein. Triplicate experiments were used to evaluate the data, and the mean value is expressed with \pm SD. * $p < 0.05$, ** $p < 0.01$, against spike-treated group or ## $p < 0.01$, against control (ANOVA, Duncan's multiple-range test)..... 109

Fig 9. Cytotoxicity evaluation of (a) Ishophloroglucin A (IPA), Diphlorethohydroxycarmalol (DPHC), Eckmaxol and Dieckol in A549 cells and (b) MHS cells. Triplicate experiments were used to evaluate the data, and the mean value is

expressed with \pm SD. * $p < 0.05$, ** $p < 0.01$, against spike-treated group or ## $p < 0.01$, against control (ANOVA, Duncan's multiple-range test). 110

Fig 10. Inhibitory effect of Ishophloroglucin A (IPA), Diploretrohydroxycarmalol (DPHC), Eckmaxol and Dieckol on (a) SARS-CoV-2 spike protein-induced inflammatory cytokine and (b) chemokine gene expression in A549 cells, (c) SARS-CoV-2 spike protein-induced inflammatory cytokine and (d) chemokine gene expression in MHS cells. Triplicate experiments were used to evaluate the data, and the mean value is expressed with \pm SD. * $p < 0.05$, ** $p < 0.01$, against spike-treated group or ## $p < 0.01$, against control (ANOVA, Duncan's multiple-range test)..... 112

Fig 11. Evaluation of the inhibitory potential of Ishophloroglucin A (IPA), Diploretrohydroxycarmalol (DPHC), Eckmaxol, and Dieckol against protein expression SARS-CoV-2 spike protein-induced NF- κ B signalling pathway in A549 cells. Triplicate experiments were used to evaluate the data and the mean value is expressed with \pm SD. * $p < 0.05$, ** $p < 0.01$, against spike-treated group or ## $p < 0.01$, against control (ANOVA, Duncan's multiple range test)..... 114

Fig 12. Evaluation of the inhibitory potential of Ishophloroglucin A (IPA), Diploretrohydroxycarmalol (DPHC), Eckmaxol, and Dieckol against protein expression SARS-CoV-2 spike protein-induced NF- κ B signalling pathway in MHS cells. Triplicate experiments were used to evaluate the data and the mean value is expressed with \pm SD. * $p < 0.05$, ** $p < 0.01$, against spike-treated group or ## $p < 0.01$, against control (ANOVA, Duncan's multiple range test)..... 115

Fig 13. In-vivo evaluation of SARS-CoV-2 spike protein-induced inflammation. (a) toxicity of the Ishophloroglucin A (IPA), Diploretrohydroxycarmalol (DPHC), Eckmaxol, and Dieckol and (b) spike protein in zebrafish, (c) SARS-CoV-2 spike protein

induced inflammatory cytokine production in zebrafish at different time points after microinjection. Triplicate experiments were used to evaluate the data and the mean value is expressed with \pm SD. * $p < 0.05$, ** $p < 0.01$, against spike-treated group or ## $p < 0.01$, against control (ANOVA, Duncan's multiple range test)..... 117

Fig 14. Anti-inflammatory effect of Ishophloroglucin A (IPA), Diploretrohydroxycarmalol (DPHC), Eckmaxol, and Dieckol in SARS-CoV-2 spike protein-induced zebrafish. (a) heart beating rate evaluation, (b) SARS-CoV-2 spike protein induced inflammatory cytokine and (c) chemokine gene expression in zebrafish and evaluation of the inhibitory potential of Ishophloroglucin A (IPA), Diploretrohydroxycarmalol (DPHC), Eckmaxol, and Dieckol. Triplicate experiments were used to evaluate the data and the mean value is expressed with \pm SD. * $p < 0.05$, ** $p < 0.01$, against spike-treated group or ## $p < 0.01$, against control (ANOVA, Duncan's multiple range test). 119

Fig 15. Macrophage and neutrophil migration in SARS-CoV-2 spike protein-induced zebrafish. (a) macrophage and neutrophil staining in zebrafish, (b) quantification of macrophage accumulation in yolks sac and (c) quantification of neutrophils in posterior blood island (PBI) area of zebrafish. Triplicate experiments were used to evaluate the data and the mean value is expressed with \pm SD. * $p < 0.05$, ** $p < 0.01$, against spike-treated group or ## $p < 0.01$, against control (ANOVA, Duncan's multiple range test). 121

List of Tables

Table 1. The cDock interaction energies and free binding energies (Kcal/ mol) of selected ligands from marine algae with 3CL ^{pro} receptor protein.....	28
Table 2. The cDock interaction energies and free binding energies (Kcal/ mol) of selected ligands from marine algae with PL ^{pro} receptor protein.	29
Table 3. Inhibitory activity of isolated compounds on the cell free cleavage of 3CL ^{pro} , PL ^{pro} and interactions of ACE-2: SARS-CoV-2 spike protein.	38
Molecular docking was performed between all ligands and ACE-2 receptor proteins. The corresponding dock scores are summarized in Table 1. According to the flexible docking, binding energy, and DS visualizer results, Ishophloroglucin A (IPA), Diphlorethohydroxycarmalol (DPHC), and Eckmaxol were selected for further studies.	69
Table 1. The cDock interaction energies and free binding energies (Kcal/ mol) of selected ligands from marine algae with ACE-2 receptor protein.....	69
Table 2. Inhibitory activity of isolated compounds on the interactions of ACE-2: SARS-CoV-2 spike protein.....	75
Table 1. Primer sequences used in the study.....	92

**Part I: Polyphenolic Compounds Isolated from Marine Algae Attenuate the
Replication of SARS-CoV-2 in the Host Cell through a Multi-Target Approach of
3CL^{pro} and PL^{pro}**

1. Introduction

An unknown series of pneumonia cases were identified in December 2019 and emerged in Wuhan, Hubei Province, China. According to the World Health Organization (WHO) office in China, the infected clusters were initially reported on 31 December 2019. A novel type of coronavirus was identified by Chinese authorities on 7 January 2020, which caused a new, infectious respiratory disease called severe acute respiratory syndrome coronavirus 2 (SARS-CoV-2). The identified coronavirus expressed significant differences from other respiratory pathogens, such as severe acute respiratory coronavirus (SARS-CoV) and Middle East respiratory syndrome coronavirus (MERS-CoV), influenza, adenovirus, and avian influenza. The origin of SARS-CoV-2 remains unclear, but RaTG13, the coronavirus isolated from bats, expressed a genetic similarity to SARS-CoV-2. Therefore, bats are considered the origin of this disease [1]. However, the transmission mechanism of the virus from bats to human beings remains unclear.

Coronaviruses that belong to the Coronaviridae family are enveloped, non-segmented, positive-sense, and single-stranded RNA viruses in the Nidovirales order [2]. The abovementioned viruses infect humans and other mammals to a considerable extent. Furthermore, Chinese horseshoe bats were identified as natural reservoir hosts for SARS-CoV [3]. SARS-CoV was therefore controlled using conventional methods such as travel restrictions and the isolation of patients. The infection mechanism of SARS-CoV-2 still needs to be fully understood, including why human beings are the principal hosts of the virus and how it escapes their innate immune systems.

Moreover, the interaction between the human Toll-like receptor (TLR), viral antigens, the mechanism of pro-inflammatory cytokine production, and its effect on critical human organs still need to be fully understood. However, the viral entry mechanism has been

identified in the literature, and it invades the human body through the respiratory system using respiratory droplets via sneezing and coughing [4]. SARS-CoV-2 consists of a protein capsid covered by glycoprotein with anchored spike proteins. These spike proteins initiate viral entry into the target cells. The entry of SARS-CoV-2 into the host cell is an essential factor required to determine the infectivity and pathogenesis of the virus [5]. Therefore, it is determined to be a key target for host immune monitoring and human intervention strategies [6]. The SARS-CoV-2 spike protein initially binds to the cell surface receptor called angiotensin-converting enzyme 2 (ACE-2), and this is known as a viral attachment; subsequently, it enters the endosome and, finally, the viral membrane fuses with the lysosomal membrane [7]. However, the continuous mutation of the SARS-COV-2 spike protein has made the development of an antiviral drug for viral infections using a spike protein inhibition strategy challenging. Therefore, in the present study, we identified that viral replication occurring in the host cell is the most successful way to control the viral load in the host.

Coronaviruses contain RNA viral genomes that are 26 to 32 kb in length. The newly sequenced SARS-CoV-2 genome was submitted to the NCBI genome database under accession number NC_045512.2, and the size was ~29.9 kb [8]. SARS-CoV-2 comprises 13 to 15 open reading frames (ORFs), including 12 functioning ORFs. The ORFs are arranged as nucleocapsid proteins. When considering the whole genome of SARS-CoV-2, it encodes for polyproteins that consist of ~7096 residues. It contains many structural and non-structural proteins (NSPs), as well as ORF1a and ORF1b, which encode for non-structural proteins and are mainly responsible for the nucleotide content of the genome. ORFs 1a and 1b encode the polyproteins pp1a and pp1b, respectively, and gene 1b employs the ribosomal frameshift mechanism to encode pp1ab. The virally encoded proteases cleave these polyproteins, producing 16 NSPs and the rest of the genomes

responsible for creating structural proteins. These proteins play a pivotal role in viral entry fusion, replication, and survival in host cells. Thus, these gene products are considered the primary drug or vaccine targets [9]. Polyprotein processing is mainly conducted by the 3-chymotrypsin-like protease (3CLpro) and papain-like protease (PLpro). The polyprotein is cleaved at 11 distinct sites by 3CLpro. This leads to the production of NSPs that are important in the process of viral replication [10]. 3CLpro plays a key role in SARS-CoV-2 replication in the host cell. According to the previous studies, high-throughput studies and structure-based activity analysis confirmed the value of the potential inhibitors of the activity of 3CLpro against SARS-CoV and MERS-CoV, which successfully inhibited virus replication activity [11-13]. Therefore, the 3CLpro of SARS-CoV-2 is considered a potential drug candidate. The PLpro of SARS-CoV and SARS-CoV-2 expresses an 83% sequence identity and diverges from MERS-CoV. However, the host substrate preference of PLpro is the difference between these two strains. Furthermore, the PLpro of SARS-CoV-2 cleaves the ubiquitin-like interferon-stimulated gene 15 protein (ISG15), and the PLpro of SARS-CoV predominantly targets the ubiquitin chain [14]. ISG15 regulates various cellular signaling pathways and host immune responses. Therefore, 3CLpro and PLpro are identified as potential drug targets for the inhibition of SARS-CoV-2.

Marine algae confront extreme environmental conditions, and their metabolism consists of a biochemical process that absorbs nutrients and converts them into essential materials for survival in these conditions [15]. These accumulated defense metabolites express a high potential to develop novel therapeutic agents [16]. Among these secondary metabolites, phlorotannins, such as polyphenolic compounds, have been identified in the research as potential antiviral agents for various types of viruses, including enveloped

[17-19] and non-enveloped viruses [20-22], which exert their antiviral activity through inhibiting vital viral proteins.

Thus, the present study aims to inhibit SARS-CoV-2 through 3CLpro and PLpro using marine natural products isolated from marine algae. Molecular docking was utilized to initially screen selected marine natural products based on the 3CLpro and PLpro protein structures. Moreover, the resulting compounds were isolated and used for biological assays to confirm the inhibition activity further. In the present study, we utilize an in vitro assay kit and introduce a simplified method to determine the inhibitory activity of the compounds using a cell-based assay. To the best of our knowledge, this is the first study that assesses the function of marine natural products concerning 3CLpro and PLpro of SARS-CoV-2 as a multi-target approach.

2. Methods and Materials

2.1 Chemicals and reagents

Dimethylsulfoxide (DMSO) and all the organic solvents (HPLC grade) used in the experiments were purchased from Sigma-Aldrich (St Louis, MO, USA). The in vitro inhibition assay kits for 3CLpro and PLpro were purchased from the AMSBIO company (Madrid, Spain). Dulbecco's modified Eagle's medium (DMEM) was purchased from Gibco/BRL (Burlington, ON, Canada), 10% fetal bovine serum (FBS) and 5% penicillin/streptomycin were purchased from WELGENE (Gyeongsan, Korea), and 3-(4,5-Dimethylthiazol-2-yl)-2,5-diphenyltetrazolium bromide (MTT) was purchased from Sigma Aldrich (St. Lois, MO, USA). The Nano-Glo® Dual-Luciferase® Reporter Assay System was purchased from Promega (Madison, Wisconsin, USA), the genes were purchased from Sino Biological (Beijing, China), and the pcDNA3 RLUC POLIRES FLUC vector was purchased from addgene (Watertown, Massachusetts, USA). The Vero E6 cell line was purchased from the American Type Culture Collection (ATCC, Manassas, VA, USA).

2.2 Preparation of Receptors

Discovery Studio (DS-Client v18.1.100.18065). Briefly, the crystal structure of each protein was downloaded from the PDB and opened in the DS. The water molecules and heteroatoms were removed, and the "Clean protein" tool was used to correct minor problems, such as missing-side chain atoms, which were added in an extended confirmation.

The "Prepare protein" tool was utilized to solve the most common problems, such as removing alternate conformations and heteroatoms, adding hydrogens, and correcting

missing or incorrectly specified residues. The energy minimization of target receptor proteins was performed using the "Protein minimization" tool. DS provides three options to prepare the binding site of the receptor protein, "based on the PDB site records", "from receptor cavities", and "current form selection". The present study used the last tool based on the available ligands of the crystal structures and previously published data. The crystal structure of 3CLpro was available in the PDB as a complex with an inhibitor called Michael acceptor inhibitor or N3 inhibitor. The binding site of 3CLpro was determined based on the mentioned inhibitor and previous studies[23]. PLpro was available in the PDB as a complex with an inhibitor GRL0617. Therefore, the binding site of PLpro was determined using GRL0617 and previous studies [24]. Briefly, the binding site was prepared as a grid in the crystal structure's ligand binding site, and the target proteins' prepared binding sites were identified by specifying a sphere of a given radius located in the active site. The geometric center of the ligand in the crystal structure was used as the center of the sphere. Python-enhanced molecular graphics tool (PyMOL, version 2.4.1) was used to calculate the root-mean-square deviation of atomic position (RMSD) value of the prepared 3CLpro or PLpro and raw 3CLpro or PLpro to determine any significant difference between them.

2.3. Preparation of ligands

The ligands were 16 compounds from marine algae. The 3D structure of each compound was generated, and hydrogen atoms were added. The energy of the ligand was minimized using the "Clean geometry" tool and applied CHARMM force field. The final ligand structure generated by the "Prepare ligand" tool was optimized using DS ligand optimization. The summary of the ligands used in this study is shown in Fig. 1. The ligands that were selected for validation were 16 compounds from marine algae.

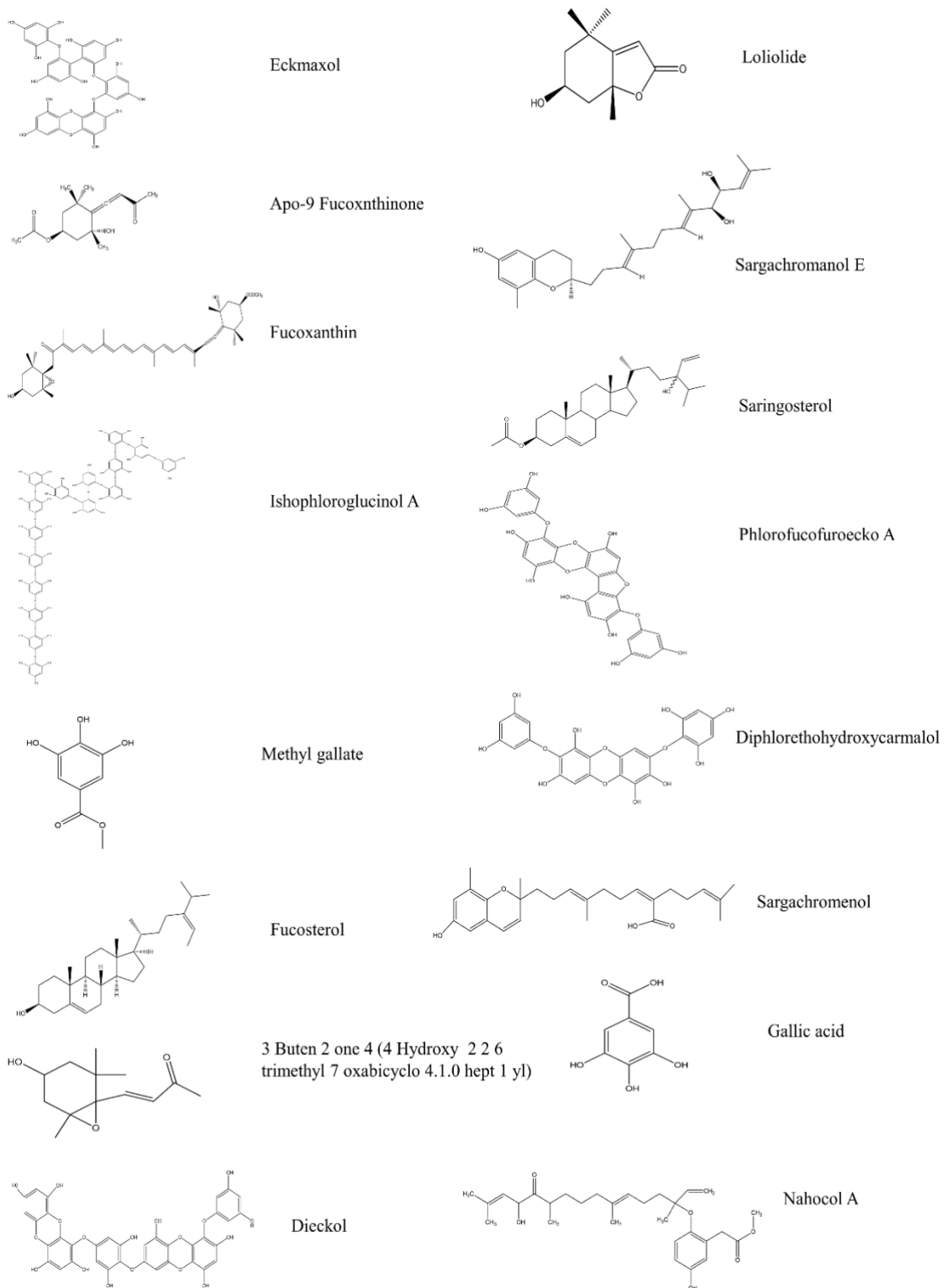


Fig. 1. Chemical structures of ligand.

2.4 Molecular docking

Docking of the selected ligands with prepared proteins was performed using DS. The crystal structure of 3CLpro bound with N3 inhibitor and PLpro bound with GRI0617 were reproduced, and the RMSD value between the raw crystal structure and docking results were calculated to confirm the accuracy of the process. Initially, Flexible docking experiments were performed using the 3D crystal structure of 3CLpro and PLpro. Flexible docking is a fully automated workflow. The flexible docking protocol allows for receptor flexibility during the docking of flexible ligands. The side chains of specified amino acids in the target receptor protein are allowed to move during docking.

Moreover, the receptor was adapted to different ligands in an induced-fit model. Therefore, flexible docking was performed to determine the ligand's suitable orientation in each receptor protein's active site. The results from the flexible docking were used to calculate the binding energy between each ligand and receptor proteins using CHARMM-based energy. The free energy of the complex, the ligand, and the receptor was used to calculate the free energy of binding.

$$\text{Energy binding} = \text{Energy Complex} - (\text{Energy Ligand} + \text{Energy Receptor})$$

The four ligands (IPA, DPHC, Eckmaxol, and Dieckol) were selected for biological assays based on molecular docking results.

2.5 Sample collection and extraction

Brown algae *Ishige okamurae* (IO) and *Ecklonia cava* (EC) were collected from Seongsan, Jeju, South Korea's coastal area, in February 2019. *Ecklonia maxima* were collected from the coast of cape town, South Africa, in February 2019. Samples were washed four times immediately after harvest with running water to remove salt, attached

sand, and epiphytes. The washed seaweeds were stored under -70°C . The frozen seaweeds were lyophilized using a freeze dryer, and dried seaweeds were ground into powder. Sample extraction was initiated using 70% ethanol three times under room temperature. The subsequent solution was evaporated using a rotary evaporator and obtained powder of ethanol extract of IO (IOE), EC (ECE), and EM (EME). IOE, ECE, and EME were dissolved in deionized water and successfully fractionated using n-hexane, chloroform, ethyl acetate, and butanol, respectively. Each resulting fraction was evaporated, and ethyl acetate fraction of IO (IOEA), EC (ECEA), and EM (EMEA) was utilized to isolate the interested compounds. The centrifugal partition chromatography (CPC 240, Tokyo, Japan) and the ODS cartridge in the FlashPrep system (C-850 FlashPrep, BUCHI, Switzerland) were utilized to further separation of IOEA, ECEA, and EMEA.

2.6 Isolation of Dieckol

The Dieckol was isolated from ECEA using an ODS cartridge in the Flashprep system (C-850 FlashPrep, BUCHI, Switzerland) equipped with PDA and ELSD detectors. The packing PREP C18, 55-105 μ m, 125 \AA (Waters, Milford, USA) column was used with a 20ml/min flow rate. The mobile phase consisted of water and acetonitrile with a gradient method (0 min 90:10 v/v, 0-12 min 90:10 v/v, 12-36 min 85:15 v/v, 36-68 min 80:20 v/v, 68-80 min 0:100 v/v). The fractions were collected based on the results at 230nm (Fig. 2).

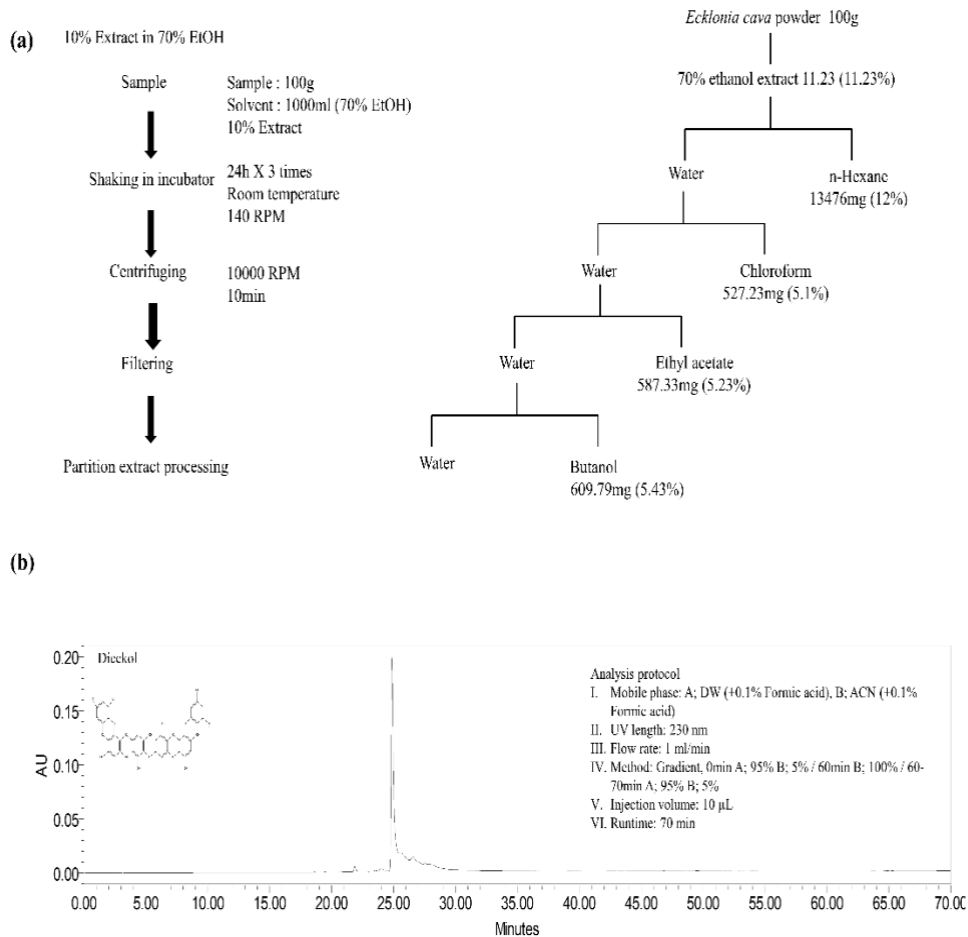


Fig. 2. Extraction and isolation procedure of *Ecklonia cava*. (a) Extraction protocol and (b) High Performance Liquid Chromatography (HPLC) analysis of Dieckol.

2.7 Isolation of Eckmaxol

The Eckmaxol was isolated from EMEA using the centrifugal partition chromatography (CPC 240, Tokyo, Japan) method comprising n-hexane: ethyl acetate: methanol: water with 3: 7: 4: 6: v/v ratio. The mentioned solvents were vigorously mixed and equilibrated to separate two phases at room temperature. The upper organic phase was used as a stationary phase, and the lower aqueous phase was used as a mobile phase. The organic stationary phase was filled into the CPC column and rotated at 1000 rpm, and the aqueous mobile phase was pumped into the column in a descending mode at a flow rate of 2 ml/min. The hydrodynamic equilibrium was maintained before injecting the sample, and 500mg of EMEA that dissolved in 6ml of 1:1 v/v water: methanol was injected through the injection valve. The automatic fraction collector was utilized to collect fractions (6ml for each tube) under a 230nm UV detection range. The HPLC system equipped with a PDA detector was used for further purification. YMC-Pack ODS-A 10mm × 250mm, 5μm column with acetonitrile + 0.1% formic acid and deionized water + 0.1% formic acid was used as a mobile phase, and the flow rate was 2ml/ min [25] (Fig. 3).

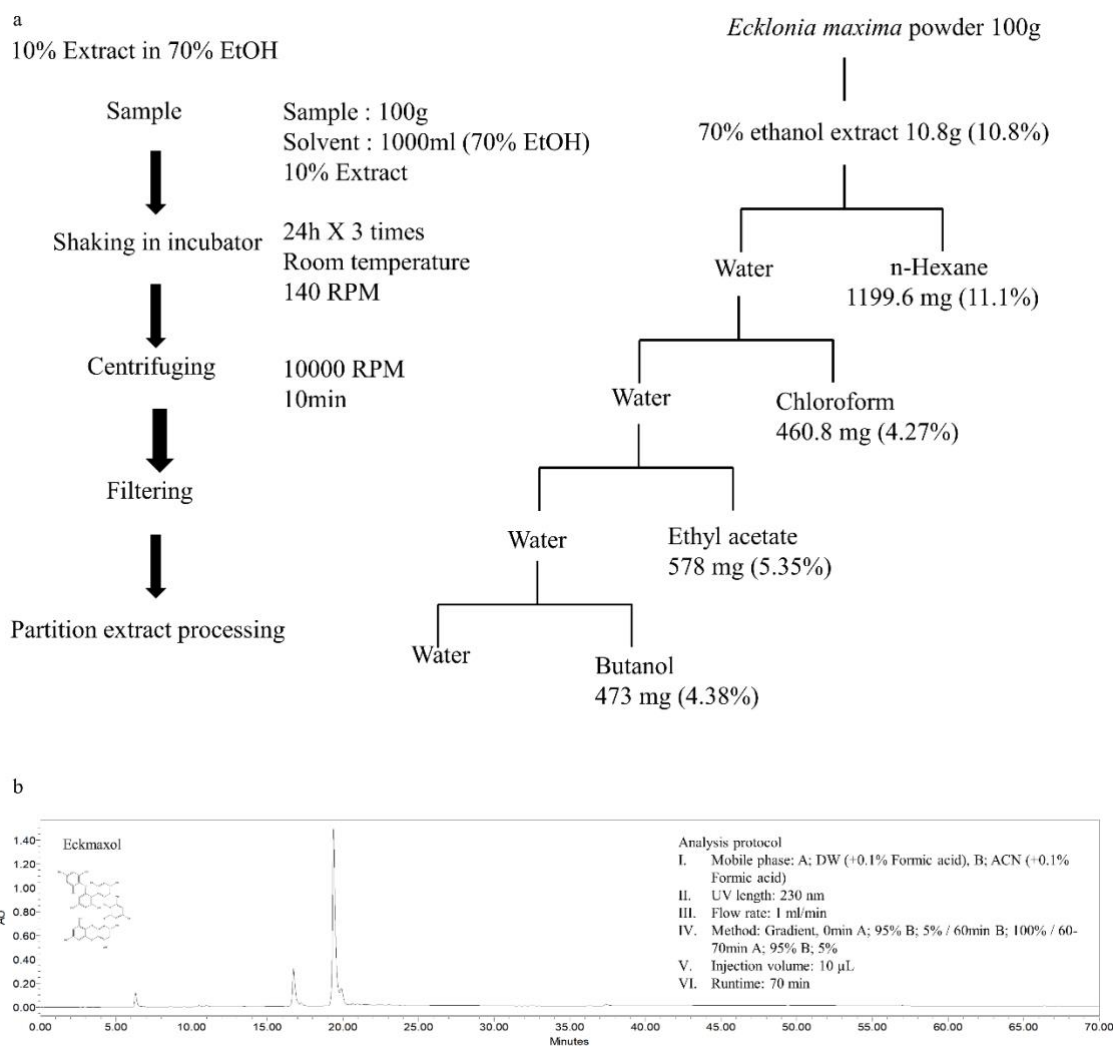


Fig. 3. Extraction and isolation procedure of *Ecklonia maxima*. (a) Extraction protocol and (b) High Performance Liquid Chromatography (HPLC) analysis of Eckmaxol.

2.8 3CL^{pro} *in-vitro* cleavage inhibition assay

The inhibitory activity of interested compounds was measured using a “3CL protease (SARS-CoV-2)” assay kit. The interested compounds were dissolved in Dimethyl sulfoxide (DMSO) and diluted into the assay buffer available with the kit. The final DMSO concentration of the highest concentration of each compound used in the assay was less than 1%. IPA, Dieckol, and Eckmaxol were incubated with 120 ng of 3CL^{pro} enzyme for 30 min under room temperature with slow shaking. The broad-spectrum antiviral medication GC376 was used as a test inhibitor in the assay, and 50 μM of the fluorogenic substrate was added to each well. The experiment was performed in 96-well plates. The positive control was well that contained only 3CL^{pro} enzyme and fluorogenic substrate used to measure the enzyme activity, and the blank well contained only substrate. The enhanced fluorescence emission due to substrate cleavage was monitored at excitation (360nm) and emission (460nm) using Synergy HTX multi-mode microplate reader (Vermont, USA)

The IC₅₀ value of each compound was calculated, and the experimental data were fit to a logistic curve with the below-mentioned equation.

$$\text{Enzyme activity \%} = [S - B] / [P - B] * 100\%$$

“B” is the fluorescence of control (substrate and assay buffer), “P” is the fluorescence of positive control (substrate and enzyme), and “S” is the fluorescence of the tested sample.

2.9 Isolation of Ishophloroglucin A (IPA) and Diphlorethohydroxycarmalol (DPHC)

Centrifugal partition chromatography (CPC 240, Tokyo, Japan) was utilized to isolate IPA and DPHC. The rotor volume was 1 L. The method was continued in a two-phase solvent system, which consisted of n-hexane: ethyl acetate: methanol: water at a

1:9:4.5:6.5 v/v ratio. These solvents were thoroughly mixed and equilibrated in a separatory funnel. The upper organic phase acted as a stationary phase and the lower aqueous phase acted as a mobile phase. The CPC instrument was conditioned until it attained hydrostatic equilibrium, and 500 mg of IOEA was dissolved in 6 mL of a 1:1 v/v water: methanol ratio of the CPC solvent system and injected using an isocratic pump (Kromaton). The effluent was monitored at 230 nm and the fractions were collected into test tubes using a fraction collector (3 min for each tube). All the fractions collected from the same compounds were pooled to continue further purification processes. The high-performance liquid chromatography (HPLC) system (Milford, Massachusetts, USA) equipped with a PDA detector was used for further purification. The semi-preparative column HPLC column YMC-Pack ODS-A 10 mm × 250 mm, 5 μm (YMC Co., Ltd.,

Kyoto, Japan) was used in an isocratic solvent mode (32% acetonitrile with 1% formic acid), and the flow rate was 2 mL/min [26, 27] (Fig 4).

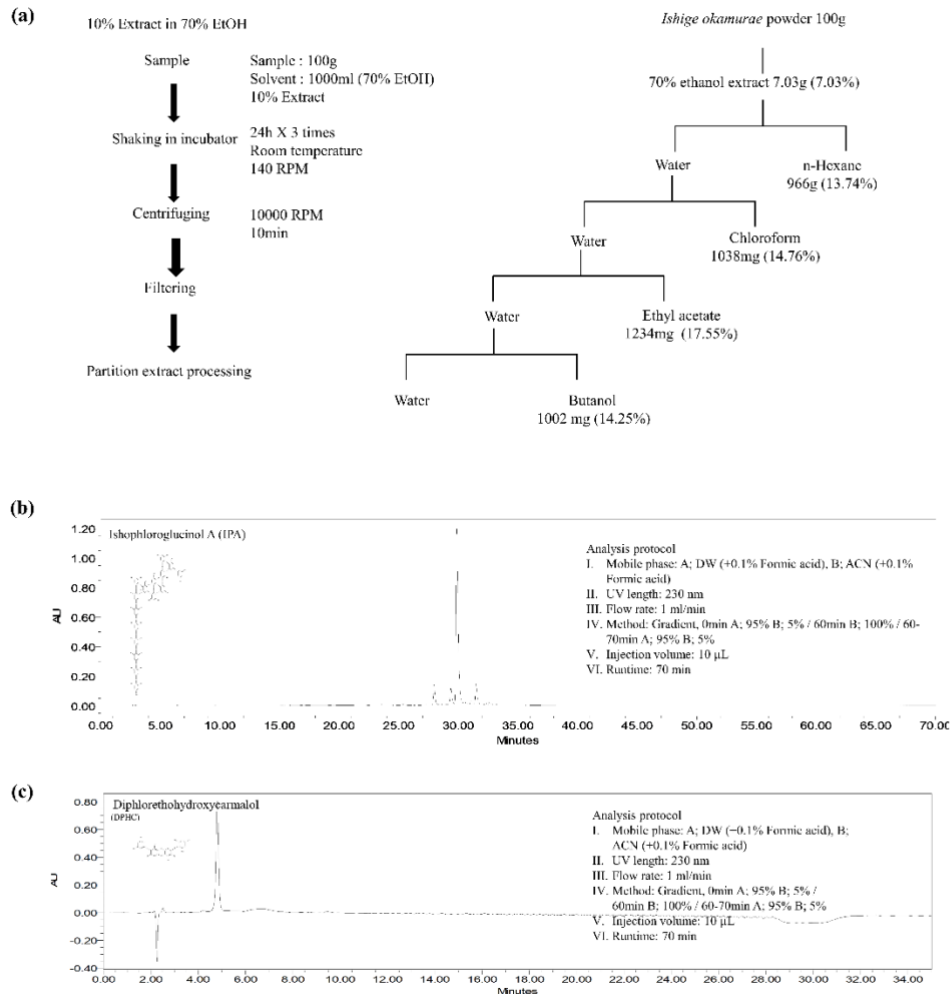


Fig. 4. Extraction and isolation procedure of Ishophloroglucinol A (IPA) and Diploretrohydroxycarmalol (DPHC) from *Ishige okamurae*, (a) Extraction protocol, (b) High Performance Liquid Chromatography (HPLC) analysis of IPA, and (c) DPHC.

2.10 PL^{pro} *in-vitro* cleavage inhibition assay

PL^{pro} enzyme inhibition activity of isolated compounds was evaluated using a “Papain-like protease (SARS-CoV-2)” assay kit (AMSBIO, Madrid, Spain). The isolated compounds were dissolved in DMSO and diluted into an assay buffer with less than 1% DMSO concentration in the assay buffer. The diluted concentrations of IPA, Dieckol, and Eckmaxol were treated into each well that contained 1.2 ng of PL^{pro} enzyme and incubated for 30 min with slow shaking under room temperature. The blank well was treated with only 25 μM fluorogenic substrate, and the positive control well contained only PL^{pro} enzyme and fluorogenic substrate. The experiment was performed in 96-well plates, and positive control well was used to evaluate the enzyme activity. The enhanced fluorescence emission due to substrate cleavage was monitored at excitation (360nm) and emission (460nm) using Synergy HTX multi-mode microplate reader (Vermont, USA), The IC₅₀ value of each compound was calculated and the experimental data were fit to a logistic curve with the below-mentioned equation.

$$\text{Enzyme activity \%} = [S - B] / [P - B] * 100\%$$

“B” is the fluorescence of control (substrate and assay buffer), “P” is the fluorescence of positive control (substrate and enzyme), and “S” is the fluorescence of the tested sample.

2.11 Enzyme Kinetic Evaluation

The enzyme kinetic mechanism of these isolated compounds was studied with a series of substrate concentrations with various concentrations of inhibitors. The data were plotted in the graph (y axis—1/V and x axis—1/[S]).

2.12 Cell-based inhibition assay

2.12.1 Cell culture maintenance

Vero-E6 cells were purchased from the American Type Culture Collection (ATCC, Manassas, VA, USA). Cells were cultured using Dulbecco's modified Eagle's medium (DMEM) (Gibco/BRL; Burlington, ON, Canada) containing 10% FBS and 1% antibiotics under 37 °C and 5% CO₂.

2.12.2 Cell-based in-vitro evaluation

The 3CLpro gene was amplified using PCR with designed forward and reverse primers 5'-GAGAGAGCGGCCGCATGGCATTCCCATCTGGTAAAGTTGAGG- 3' and 5'-GAGAGAGGATCCCCTTCCTGAAGCCGCTCTGCAGCACGGCGCTTTGGAAAGTAACACCTGAGCATTGTCTAACAAC-3', respectively. The PLpro gene was amplified using PCR with designed forward and reverse primers 5'-GAGAGAGCGGCCGCATGGAAGTGAGGACTATTAAGGTGTTTACAACAG-3' and 5'-GAGAGAGGATCCCGCACATGGCGCCGCCCTCAGCCTAACTGGTTTTATGGTTGTTGTGTAAGTGTCTTTCTTTG, respectively.

The forward primer consisted of a NotI restriction site, and the reverse primer contained a BamHI restriction site and in-frame gene encoding for the 3CLpro-cleavage site (AGCGCCGTGCTGCAGAGCGGCTTCAGGAAG) luciferase gene and PLpro-cleavage site (AGGCTGAGGGGCGGCGCCATGTGC) luciferase gene. The plasmid that contained the 3CLpro gene was amplified by PCR using the abovementioned primers and cloned into the NotI/BamHI restriction sites of the pcDNA RLUC POLIRES FLUC vector (addgene, Watertown, MA, USA). The recombinant plasmid was transfected into Vero-E6 cells using an X-tremeGENE HP DNA transfection reagent (Sigma-Aldrich, St. Louis, MO, USA). Vero-E6 cells at 80–90% confluence in 24-well plates were

transfected with 0.25 μg of total plasmid per 1 well that contained DMEM with 0% FBS and 0% antibiotics. The media was replaced with DMEM that contained 10% FBS and 1% antibiotics following 23 h of incubation (37 °C and 5% CO₂) and the samples were treated. The dual-luciferase reporter assay system (Promega) was utilized to evaluate the expression of firefly luciferase activity after an 18–20 h incubation (37 °C and 5% CO₂) period. The expression level of firefly and renilla luciferases was measured by a Luminometer (Fig. 5).

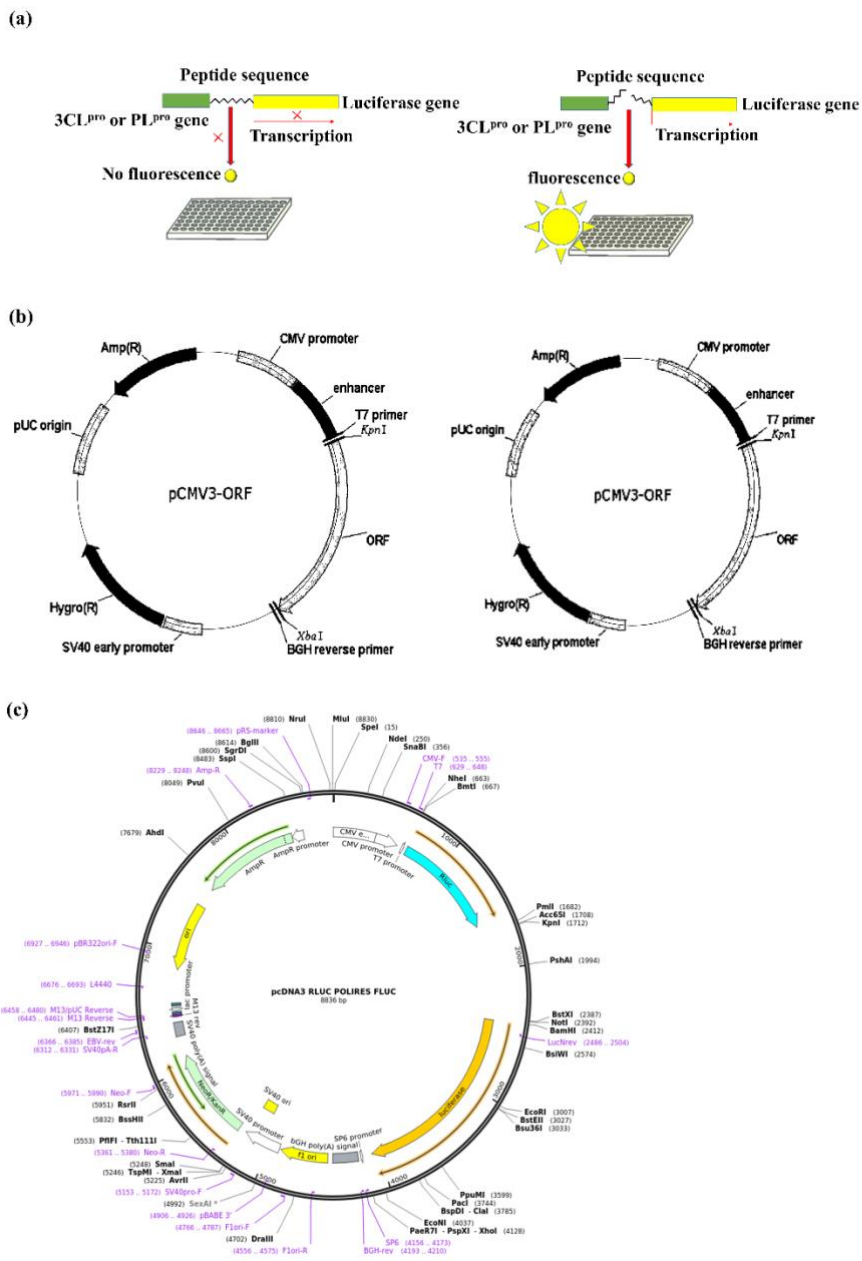


Fig. 5. Cell based 3CL^{pro} and PL^{pro} cleavage inhibition assay. (a) principle of the assay, (b) Plasmid that contain 3CL^{pro} and PL^{pro} genes, and (c) vector that contain firefly Luciferase and renilla luciferase.

2.13 Cytopathic Effect (CPE) Reduction Evaluation

The CPE reduction assay was performed according to the previously reported method [36]. Briefly, the cells were seeded with 5×10^4 cells/well in a 96-well plate and incubated at 37 °C for 48 h. A total of 100 μ L of the virus was treated in each well using DMEM media that was FBS free and 1% antibiotic to infect a 0.01 multiplicity of infection (MOI) and incubated for an additional 1 h at 37 °C. Subsequently, the infected cells were treated with samples after removing the virus, and 72 h of incubation was performed. The MTT solution was added and allowed to stand for a 4 h incubation period. The formazan crystals were dissolved, and the absorbance was measured. The cytotoxicity ratio was calculated according to the following equation:

$$\text{Virus inhibition rate (\%)} = ((\text{Test OD} - \text{Virus OD}) / (\text{Control OD} - \text{Virus OD})) \times 100\%$$

2.14 Statistical analysis

All compounds were examined in the set of triplicate experiments. IC₅₀ (50% inhibitory concentration) values of compounds represent the concentration that caused 50% enzyme activity loss. Using a minimum of three samples, the standard deviation was calculated in all experiments. The inhibition mechanism of the compounds was determined by comparing the statistical results, including Akaike's information criterion values, of different inhibition models and selecting the one with the best fit [28].

3. Results

3.1 Receptor and ligand preparation

3.1.1. Structure of 3CL^{pro} receptor protein preparation

The previously resolved X-ray crystallography of SARS-CoV-2 3CL^{pro} at a high resolution of 2.16Å was obtained from PDB (PDB ID 6LU7) in complex with the N3 inhibitor (ID PRD_002214) (Fig. 6a). The total structure weight was 34.4kDa. The N3 inhibitor was bound to the present structure by conventional hydrogen bonds with PHE140, GLY143, HIS164, GLU166, GLN189, THR189 residues, carbon-hydrogen bonds with ASN142, Met165, HIS172, and Alkyl bonds with HIS41, MET49, LEU167, PRO168, and ALA191 (Fig. 6b, 6c, and 6d). The radius of the prepared binding site sphere was 13.82Å and HIS41, MET49, PHE140, ASN142, GLY143, HIS164, MET165, GLU166, LEU167, PRO168, HIS 172, GLN189, THR190, and ALA191 (Fig. 6e). The prepared 3CL^{pro} was superimposed with the original 3CL^{pro} available in PDB PyMOL and the calculated RMSD value was 0.185.

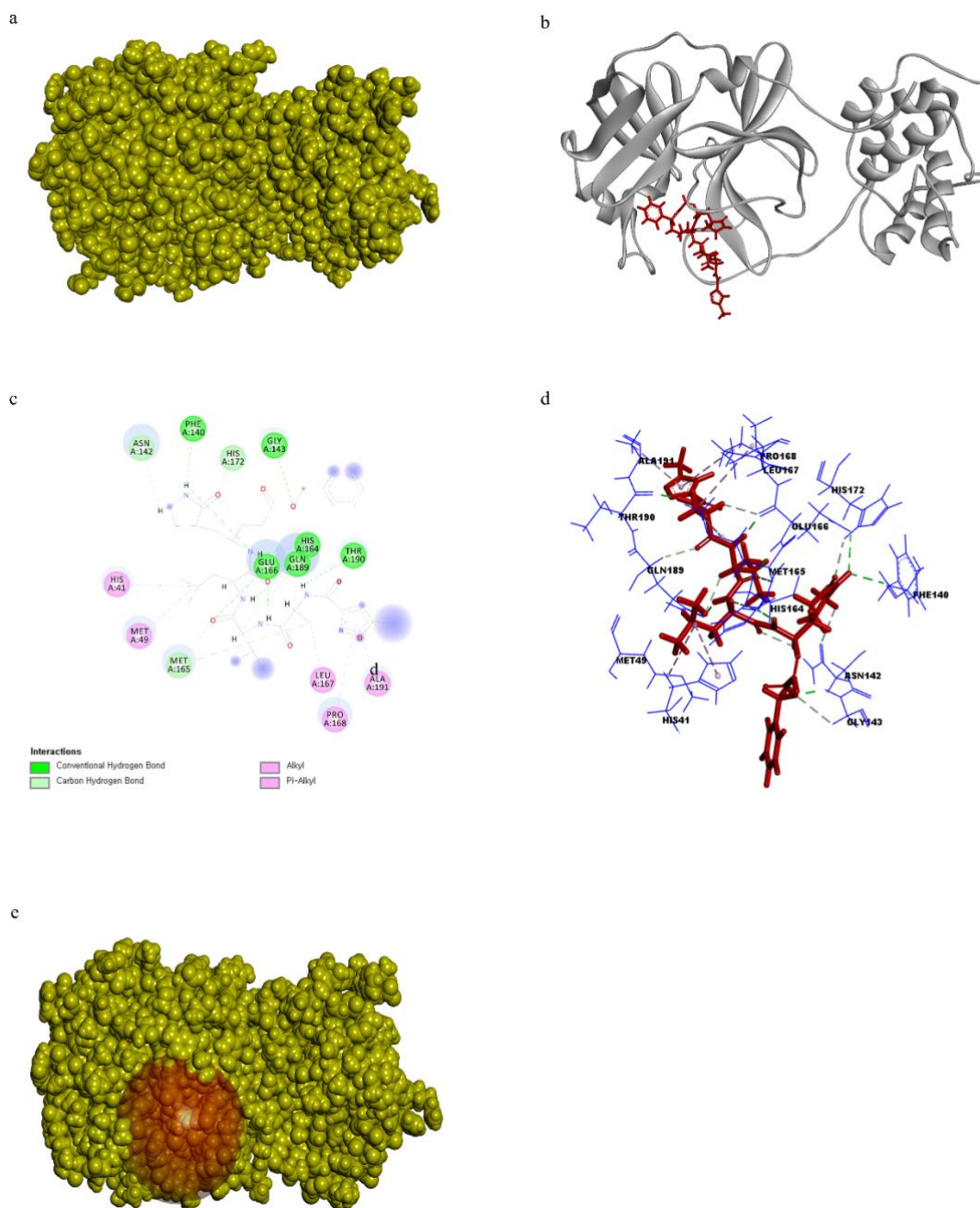


Fig. 6. Receptor preparation of 3CL^{PRO}. a) Surface representation 3CL^{PRO} and N3 inhibitor ligand complex 3CL^{PRO} receptor protein is in yellow color and N3 inhibitor in red color. b) Cartoon representation of 3CL^{PRO} and N3 inhibitor ligand complex. 3CL^{PRO} receptor protein is in yellow color and N3 inhibitor is in red color. c) 2D representation of ligand interaction between 3CL^{PRO} and N3 inhibitor. d) 3D representation of ligand interaction between 3CL^{PRO} and N3 inhibitor. e) Prepared active site of 3CL^{PRO}.

3.1.2 Structure of PL^{pro} receptor protein preparation

The X-ray crystallography of SARS-CoV-2 3CL^{pro} (PDB ID 7CMD) was obtained from PDB as a complex with GRO0617 at a high resolution of 2.59Å and total structure weight was 145.97kDa (Fig. 7a). The GRL0617 was bound with PL^{pro} enzyme using conventional hydrogen bonds with ASP164 and GLN269, residues, carbon-hydrogen bond with TYR268 residue, and alkyl bonds with LEU162, PRO247, PRO248, TYR264, and TYR273 residues (Fig. 7b, 7c, and 7d). The ligand-binding site was defined using a binding site sphere with a 15.9Å radius including PRO247, PRO248, LEU162, ASP164, TYR268, GLU269, and TYR273 (Fig. 7e). The prepared PL^{pro} was superimposed with the original PL^{pro} available in PDB using PyMOL and the calculated RMSD value was 0.235.

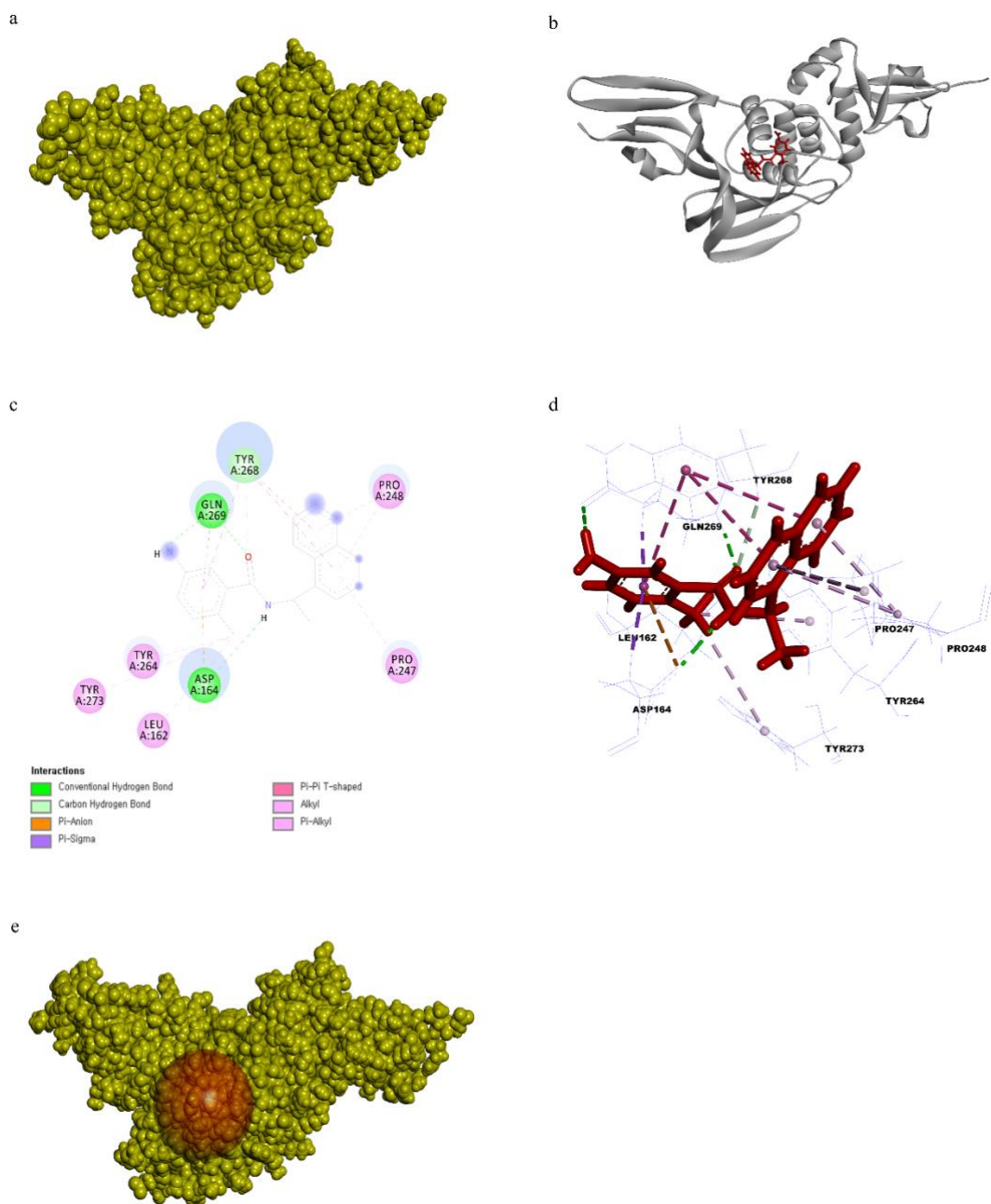


Fig. 7. Receptor preparation of PL^{pro}. a) Surface representation PL^{pro} and GRL0617 inhibitor ligand complex 3CL^{pro} receptor protein is in yellow color and GRL0617 inhibitor in red color. b) Cartoon representation of PL^{pro} and GRL0617 inhibitor ligand complex. PL^{pro} receptor protein is in yellow color and GRL0617 inhibitor is in red color. c) 2D representation of ligand interaction between PL^{pro} and GRL0617 inhibitor. d) 3D representation of ligand interaction between PL^{pro} and GRL0617 inhibitor. e) Prepared active site of PL^{pro}.

3.1.3 Ligand preparation

Sixteen ligands were prepared using DS “Prepare ligand”, and all the prepared ligand structures were summarized in (Fig. 8). The most stable ligand conformation was used for molecular docking.

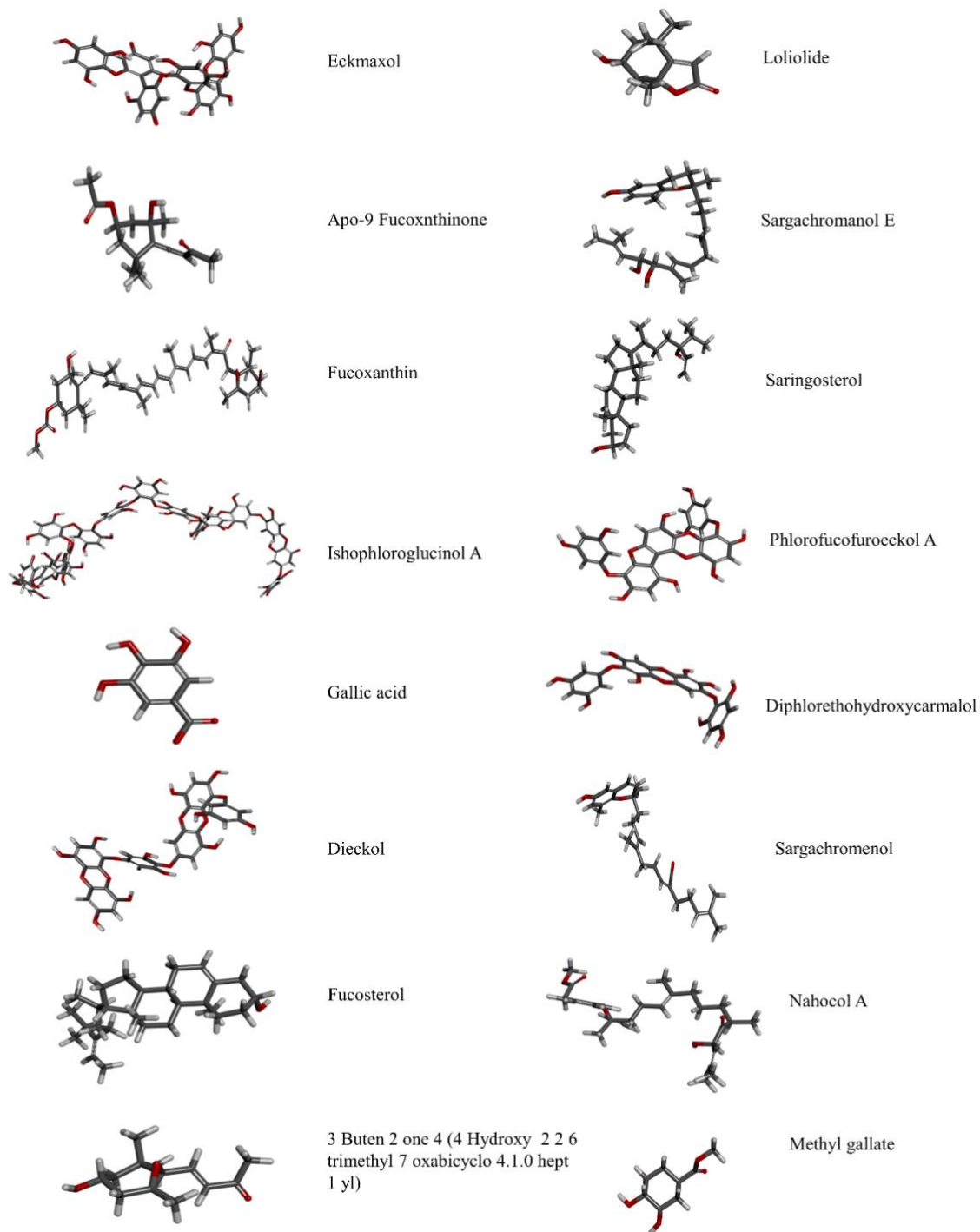


Fig. 8. Three-dimensional structures of prepared ligand using Discovery studio.

3.2 Molecular docking

Molecular docking was performed between all ligands and 3CLpro, and PLpro receptor proteins separately. The corresponding dock scores are summarized in Tables 1 and 2, respectively. According to the flexible docking, binding energy, and DS visualizer results, IPA, DPHC, Dieckol, and Eckmaxol were selected for further studies.

Table 1. The cDock interaction energies and free binding energies (Kcal/ mol) of selected ligands from marine algae with 3CL^{pro} receptor protein.

No	Sample Name	cDock interaction energy (Kcal/mol)	Binding energy (Kcal/ mol)
1	GC376	-58.7189	-182.685
2	N3 inhibitor	-72.5369	-185.054
3	Ishophloroglucinol A	-63.1128	-186.875
4	Diphlorethohydroxycarmalol	-63.1128	-158.462
5	Dieckol	-68.0895	-257.388
6	Phlorofuofureckol-A	-	-
7	Nahocol A	-48.4205	-119.254
8	Saringosterol	-51.1228	-100.977
9	Sargacromanol E	-54.4594	-118.902
10	Fucoxanthin	-	-
11	Eckmaxol	-7.9218	-235.86
12	Fucosterol	-51.7309	-93.9243
13	Gallic acid	-28.1739	-141.556
14	Methyl gallate	-39.1007	-98.995
15	Apo-9 fucoxanthinone	-	-
16	3-Buten-2-one,4-(4-hydroxy-2,2,6-trimethyl-7-oxabicyclo [4.1.0]hept-1-yl)-	-27.7698	-62.684
17	Loliolide	-21.163	-93.869
18	Sargachromenol	-64.3135	-91.963

Table 2. The cDock interaction energies and free binding energies (Kcal/ mol) of selected ligands from marine algae with PL^{pro} receptor protein.

No	Sample name	cDock interaction energy (Kcal/mol)	Binding energy (Kcal/ mol)
1	GRL0617	-74.2579	-133.288
2	Ishophloroglucinol A	-43.5452	-271.055
3	Diphlorethohydroxycarmalol	-114.898	-146.253
4	Dieckol	-65.5972	-191.131
5	Phlorofucofuroeckol-A	-74.2645	-110.355
6	Nahocol A	-44.5236	-110.496
7	Saringosterol	-41.3209	-77.7694
8	Sargacromanol E	-54.1180	-15.2530
9	Fucoxanthin	-	-
10	Eckmaxol	-72.3064	-169.8830
11	Fucosterol	-34.7463	-71.5172
12	Gallic acid	-31.6026	-63.3519
13	Methyl gallate	-35.2097	-35.6745
14	Apo-9 fucoxanthinone	-	-
15	3-Buten-2-one,4-(4-hydroxy-2,2,6-trimethyl-7-oxabicyclo [4.1.0]hept-1-yl)-	-33.9821	-74.9392
16	Loliolide	-21.1630	-93.8690
17	Sargachromenol	-47.2003	-115.477

3.2.1. 3CL^{pro} enzyme

IPA was bound to the binding site of 3CL^{pro} through THR26, ASN119, PHE140, ASN142, GLY143, PRO168, and THR190 residues via conventional hydrogen bonds with the length of 2.35 Å, 2.30 Å, 1.92 Å, 1.99 Å, 2.93 Å, 2.96 Å, 2.31Å respectively and GLU166 made 3 hydrogen bonds with 1.94Å, 1.97Å, and 1.94Å length. Further, there is a 5.08 Å length one pi-sulfur bond with MET49 and a 5.43 Å length pi-alkyl bond with LEU141(Fig. 9).

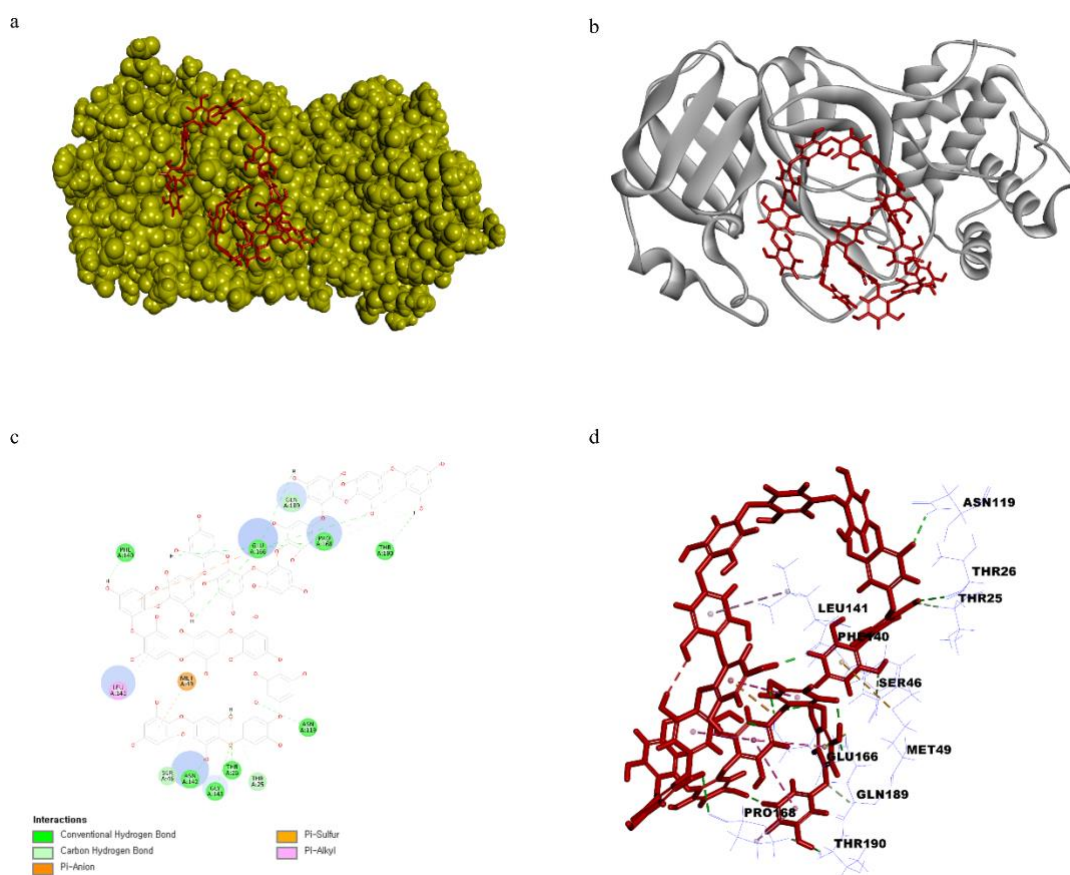


Fig. 9. In-silico analysis of 3CL^{pro} with Ishophloroglucinol A (IPA). a) 3D representation of docking pose of IPA with 3CL^{pro}. b) Cartoon representation of docking pose of IPA with 3CL^{pro}. c) 2D representation of Ligand interaction of IPA with 3CL^{pro}. d) 3D representation of Ligand interaction of IPA with 3CL^{pro}.

DPHC was stabilized in the active site of 3CLpro through three conventional hydrogen bonds with CYS44, CYS 145, and GLU166; five carbon-hydrogen bonds with THR24, THR 25, MET165, ASN142, and ASN143; and one salt bridge with HIS163. The bond lengths of conventional hydrogen bonds were 1.89 Å–2.3 Å, the lengths of the carbon–hydrogen bonds were 2.56 Å–2.67 Å; and the length of the salt bridge was 5.82 Å (Fig. 10).

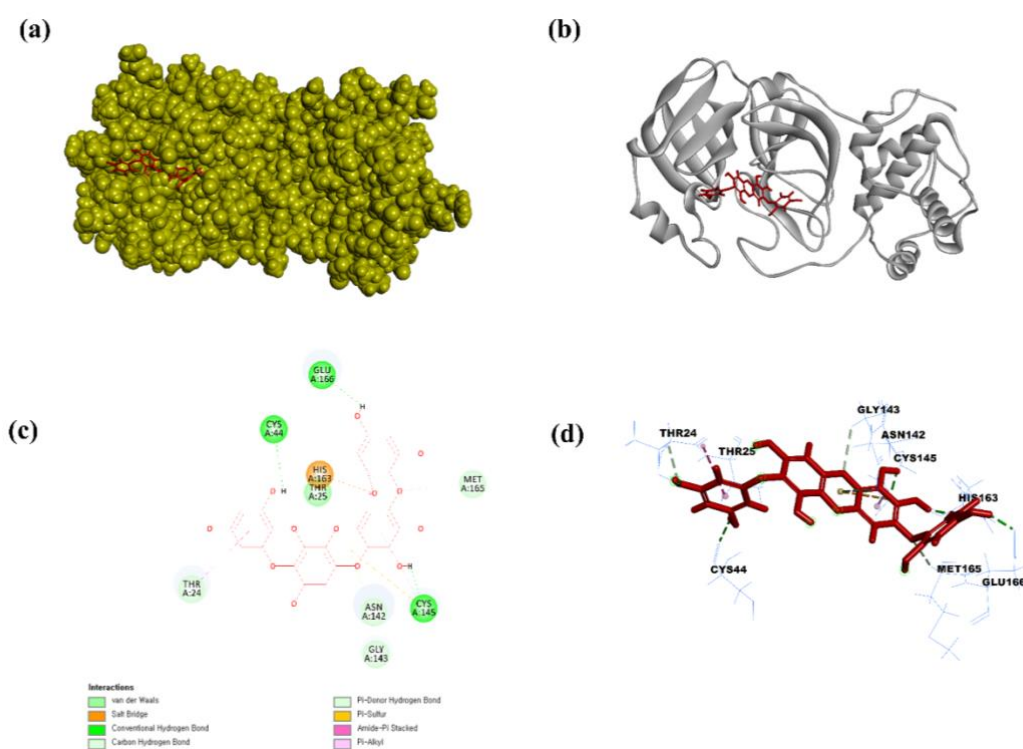


Fig 10. In-silico analysis of 3CLpro with Diphlorethohydroxycarmalol (DPHC), a) 3D representation of docking pose of DPHC with 3CLpro. b) Cartoon representation of docking pose of DPHC with 3CLpro. c) 2D representation of Ligand interaction of DPHC with 3CLpro. d) 3D representation of Ligand interaction of DPHC with 3CLpro.

Dieckol was bound to the 3CL^{PRO} through five conventional hydrogen bonds with PHE140, ASN142, GLU166, PRO168, and ARG188, and the length of bonds were 2.91 Å, 2.88 Å, 3.97 Å, 2.01 Å, and 2.21 Å respectively. Further, there are three pi-pi T-shaped bonds with HIS41, LEU141, and HIS164 residues, and the length of each bond was 6.87 Å, 4.19Å5.33 Å respectively, and 4 pi-anion bonds. Among these bonds, binding takes place between 5.28 Å length to CYS145, 5.33 Å length to HIS164, 4.41 Å length to MET165, and 5.64 Å, 5.22 Å length to GLU166 residue, and finally, two pi-alkyl bonds with MET165 residue. The length of each bond was 4.67 Å and 5.09 Å (Fig. 11).

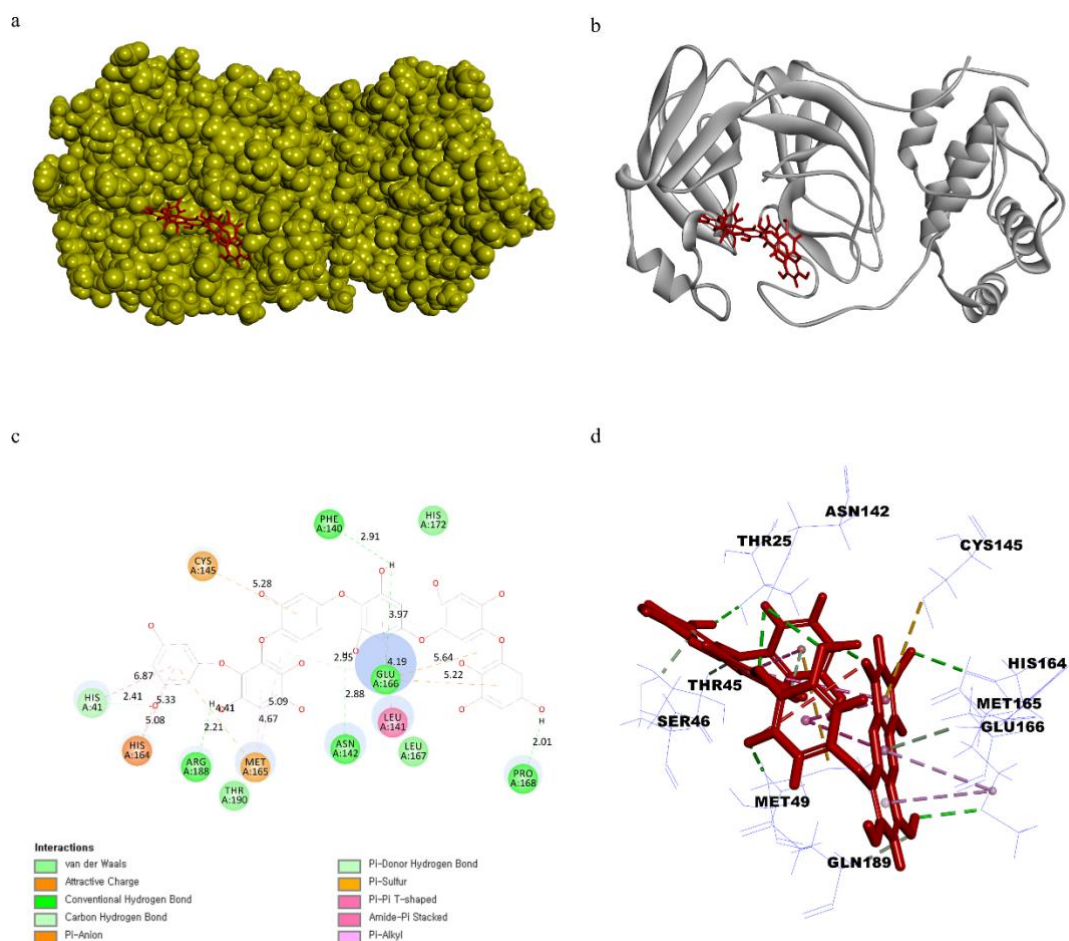


Fig. 11. In-silico analysis of 3CL^{PRO} with Dieckol. a) 3D representation of docking pose of Dieckol with 3CL^{PRO}. b) Cartoon representation of docking pose of Dieckol with 3CL^{PRO}. c) 2D representation of Ligand interaction of Dieckol with 3CL^{PRO}. d) 3D representation of Ligand interaction of Dieckol with 3CL^{PRO}.

Eckmaxol was bound to the 3CL^{pro} using ASN142, GLY143, SER144, HIS164, GLU166, ASP187, and GLN189 residues via conventional hydrogen bonds with 2.34 Å, 1.78 Å, 4.17 Å, 2.09 Å, 2.82 Å, 2.10 Å, 1.88Å length respectively. Further, there are four carbon-hydrogen bonds, PHE140, LEU141, MET165, and LEU167, with 2.47 Å, 2.58 Å, and 2.7 Å length, respectively and two pi-alkyl bonds with MET49 and CYS145 residues with 4.62 Å and 4.77 Å length (Fig. 12).

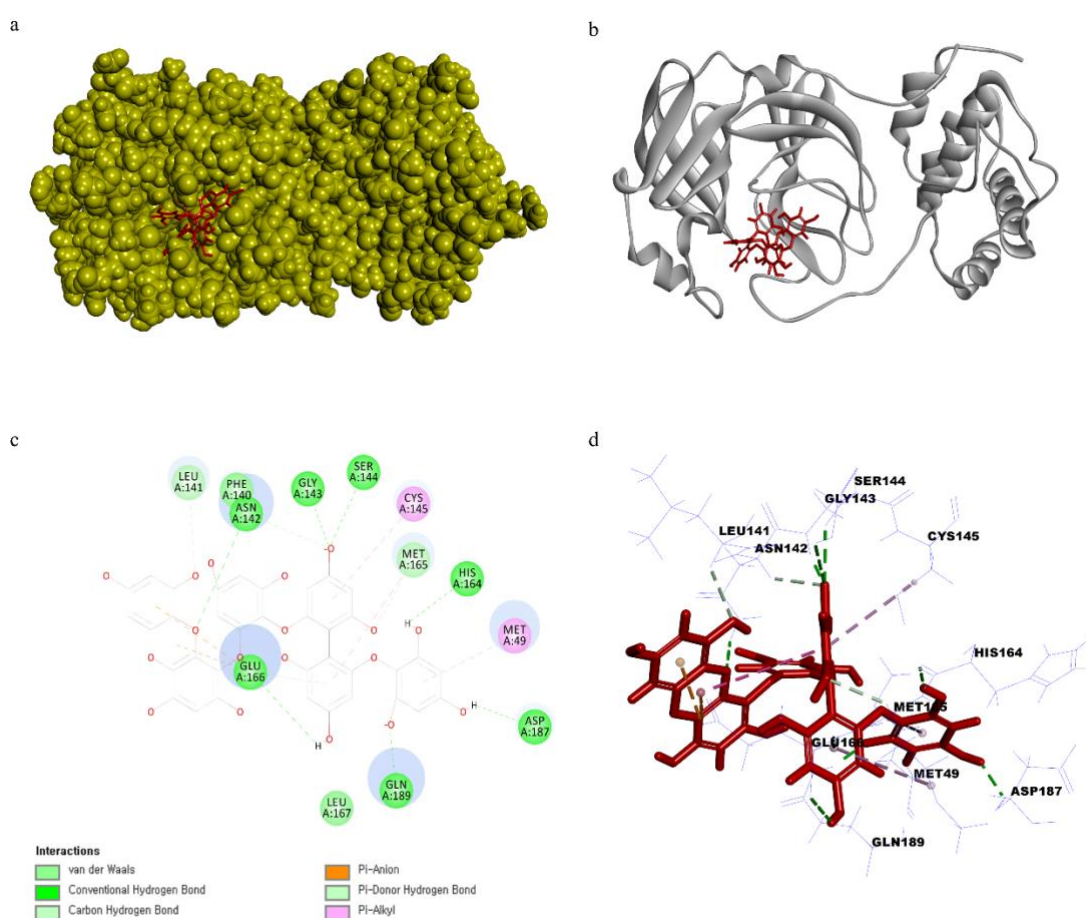


Fig. 12. In-silico analysis of 3CL^{pro} with Eckmaxol. a) 3D representation of docking pose of Eckmaxol with 3CL^{pro}. b) Cartoon representation of docking pose of Eckmaxol with 3CL^{pro}. c) 2D representation of Ligand interaction of Eckmaxol with 3CL^{pro}. d) 3D representation of Ligand interaction of Eckmaxol with 3CL^{pro}.

3.2.2. PL^{pro} enzyme

IPA was bound to the PL^{pro} by five conventional hydrogen bonds through ASP164, ASN267, GLN250, TYR268, and TYR273 with 2.33 Å, 1.93 Å, 1.86 Å, 1.91 Å, and 1.91 Å length respectively. IPA made two conventional hydrogen bonds through ASN267 with 2.24 Å and 2.44 Å lengths. Furthermore, there are three pi-alkyl bonds between IPA and PL^{pro} through PRO247 and ALA249 with 4.69 Å, 5.33 Å, and 4.88 Å length and one pi-sulphur bond with MET208 residue with a length of 5.98 Å and one pi-anion bond through ASP164 with 3.24 Å length (Fig. 13).

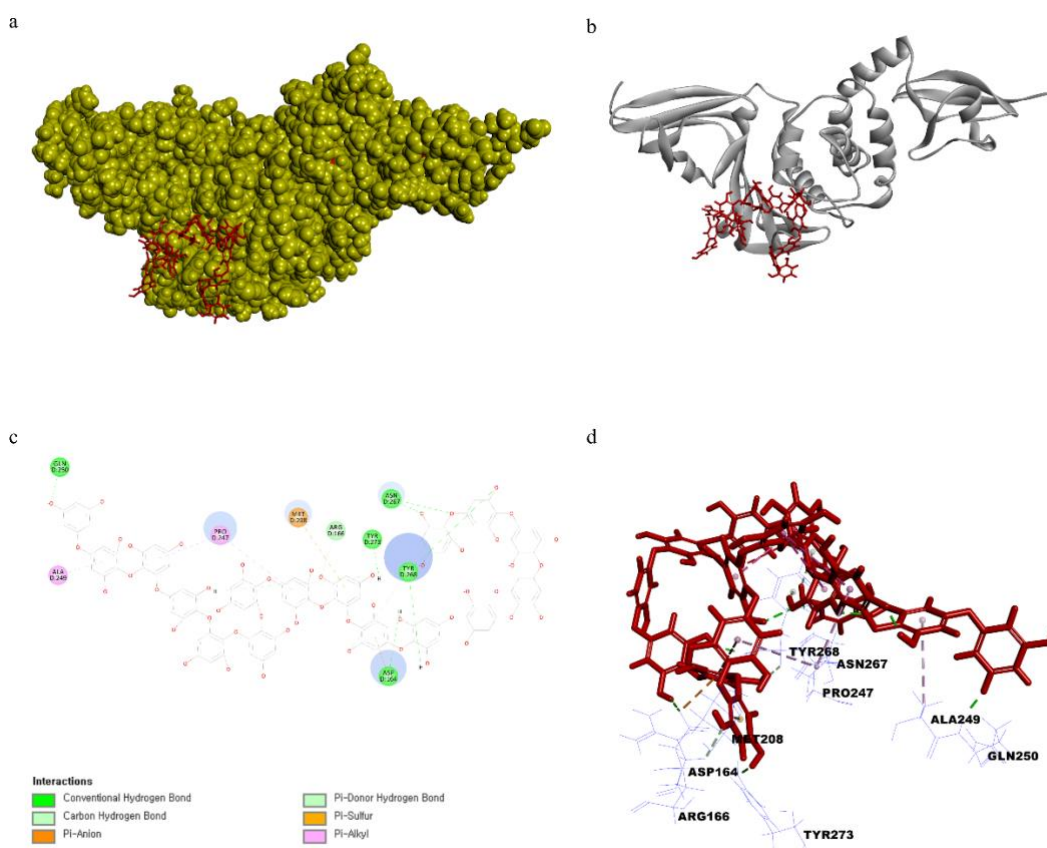


Fig. 13. In-silico analysis of PL^{pro} with Ishophloroglucinol A (IPA). a) 3D representation of docking pose of IPA with PL^{pro}. b) Cartoon representation of docking pose of IPA with PL^{pro}. c) 2D representation of Ligand interaction of IPA with PL^{pro}. d) 3D representation of Ligand interaction of IPA with PL^{pro}.

DPHC produced two conventional hydrogen bonds with PL^{pro} via two conventional hydrogen bonds with GLN270 and THR302 (1.94 Å and 1.92 Å); one carbon–hydrogen bond with PRO249 (2.22 Å); and three weak bonds, including an attractive charge with LYS158, a pi-cation with ASP165, and pi-anion with ARG167 (5.68–5.69 Å) (Fig. 14).

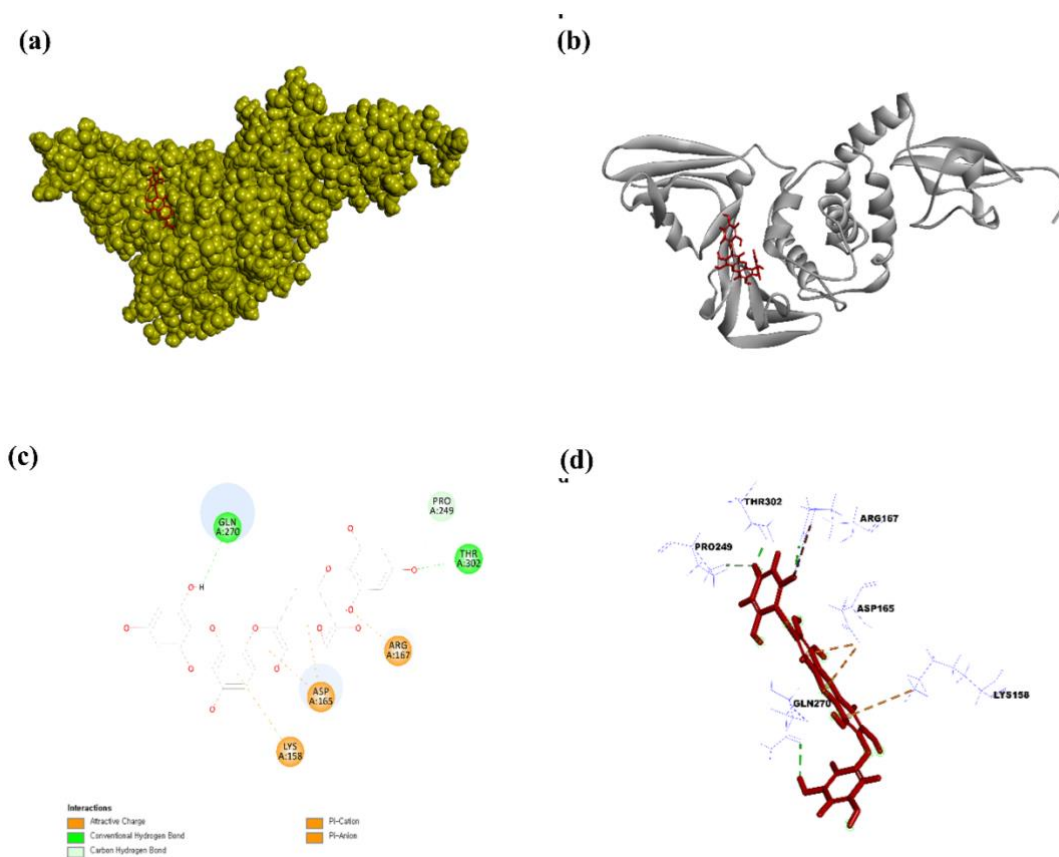


Fig. 14. In-silico analysis of PL^{pro} with Diphlorethohydroxycarmalol (DPHC), a) 3D representation of docking pose of DPHC with PL^{pro}. b) Cartoon representation of docking pose of DPHC with PL^{pro}. c) 2D representation of Ligand interaction of DPHC with PL^{pro}. d) 3D representation of Ligand interaction of DPHC with PL^{pro}.

Dieckol made three conventional hydrogen bonds with PL^{pro} through GLY163, TYR273, and THR302 residues, and bond lengths were 1.91 Å, 2.18 Å, and 2.06 Å. Further, PRO247 and SER245 made a carbon-hydrogen bond with 2.51 Å and 2.54 Å length. Moreover, PRO2478 made a pi-alkyl bond with 5.50 Å lengths. ARG166 made a salt bridge with 1.75 Å length and ASP164 bound to Dieckol via three pi-anion with 4.87 Å, 4.0 Å, and 3.90 Å. ALA246 made two amide-pi staked bonds with 5.50 Å and 5.37 Å lengths. THR301 residue made a 2.88 Å length pi-lone pair with Dieckol (Fig. 15).

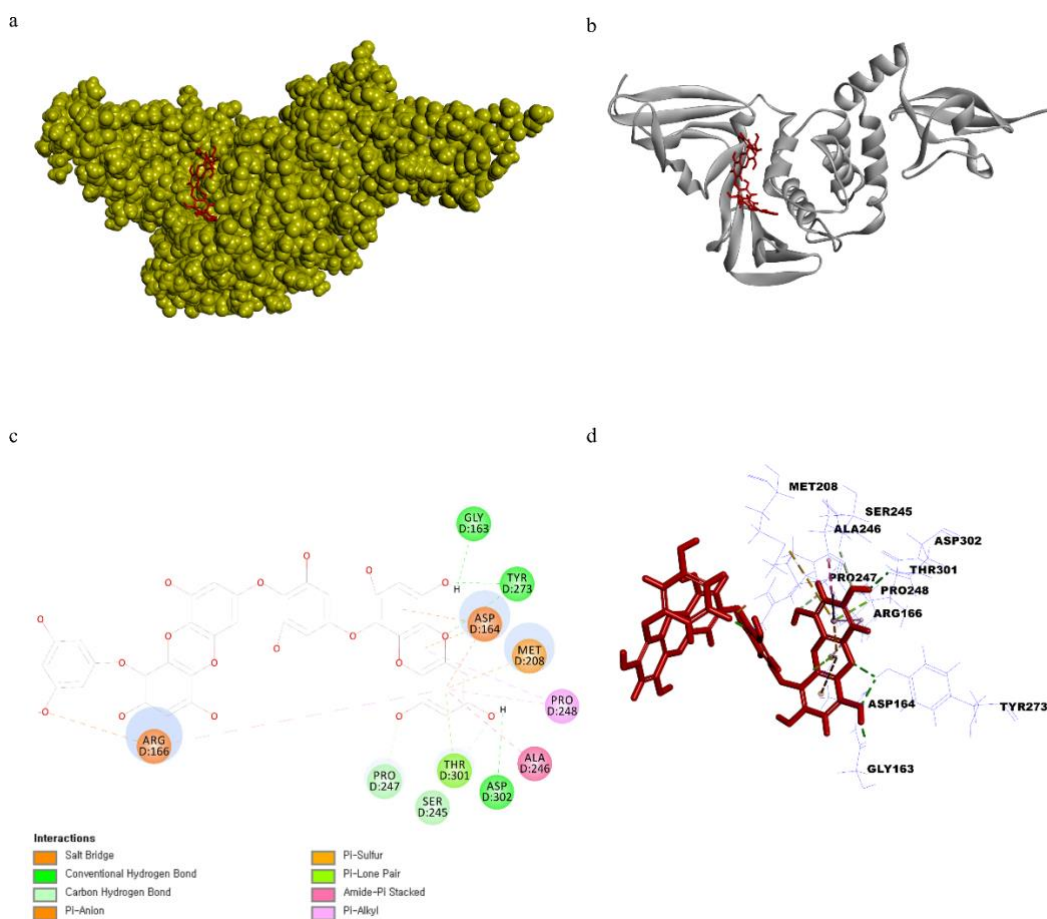


Fig. 15. In-silico analysis of PL^{pro} with Dieckol. a) 3D representation of docking pose of Dieckol with PL^{pro}. b) Cartoon representation of docking pose of Dieckol with PL^{pro}. c) 2D representation of Ligand interaction of Dieckol with PL^{pro}. d) 3D representation of Ligand interaction of Dieckol with PL^{pro}.

Eckmaxol was bound to the PL^{pro} through ARG166, TYR273, and ASP302 residues via conventional hydrogen bonds with 2.01 Å, 2.41 Å, and 2.76 Å length, respectively. Further, there are two carbon-hydrogen bonds between Eckmaxol and PRO248 and TYR248 with 2.62 Å and 2.91 Å lengths, respectively. PRO247 made two pi-alkyl bonds with Eckmaxol with 5.00 Å, and 4.98 Å length, and POR248, and ARG166 made another pi-alkyl bond with 5.36 Å and 5.43 Å length, respectively (Fig. 16).

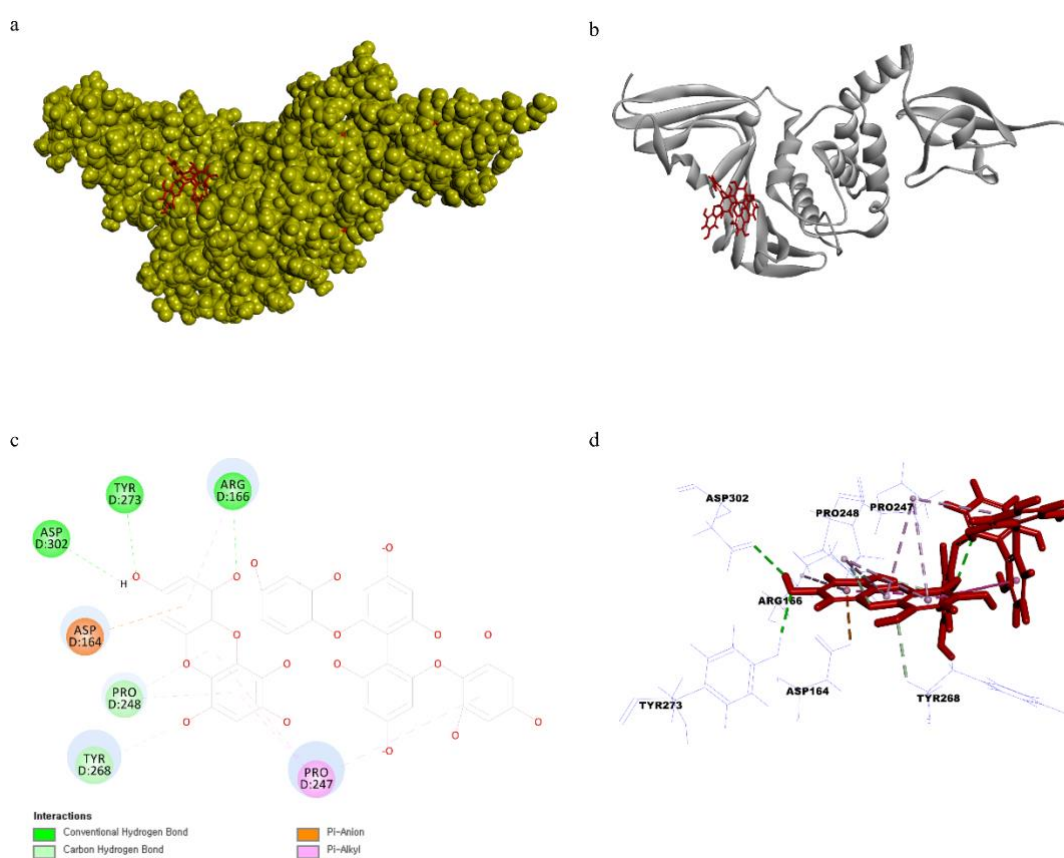


Fig. 16. In-silico analysis of PL^{pro} with Eckmaxol. a) 3D representation of docking pose of Eckmaxol with PL^{pro}. b) Cartoon representation of docking pose of Eckmaxol with PL^{pro}. c) 2D representation of Ligand interaction of Eckmaxol with PL^{pro}. d) 3D representation of Ligand interaction of Eckmaxol with PL^{pro}.

3.3 In-vitro inhibition of marine algal compounds

The inhibition ability of IPA, DPHC, Dieckol, and Eckmaxol was evaluated using an in-vitro inhibition assay kit of 3CL^{pro} and PL^{pro}. The results are summarized in Table 3. The broad-spectrum antiviral medication GC376 was used as a positive control against 3CL^{pro} [29], and GRL0617 was used as the positive control against PL^{pro} [30]. The results show that IPA expressed remarkable dose-dependent inhibition activity against 3CL^{pro}. Moreover, DPHC, Dieckol, and Eckmaxol showed elevated inhibition activity (Fig. 19). PL^{pro} cleavage mechanism was also inhibited by IPA with the lowest IC₅₀ value. Dieckol and Eckmaxol also inhibited the mechanism of PL^{pro} significantly (Fig. 17 and 18).

Table 3. Inhibitory activity of isolated compounds on the cell free cleavage of 3CL^{pro}, PL^{pro} and interactions of ACE-2: SARS-CoV-2 spike protein.

No	Drug target	Ligand	IC ₅₀ value
1	3CL ^{pro}	Ishophloroglucin A (IPA)	0.4814 ± 0.031
2		Dieckol	5.4902 ± 0.092
3		Eckmaxol	1.8886 ± 0.078
4		Diphlorethohydroxycarmalol (DPHC)	3.1193 ± 0.066
5		GC376	0.4231 ± 0.045
6	PL ^{pro}	Ishophloroglucin A (IPA)	1.4048 ± 0.007
7		Dieckol	19.7404 ± 0.090
8		Eckmaxol	19.8349 ± 0.121
9		Diphlorethohydroxycarmalol (DPHC)	6.6367 ± 0.056
10		GRL0617	1.5 ± 0.120

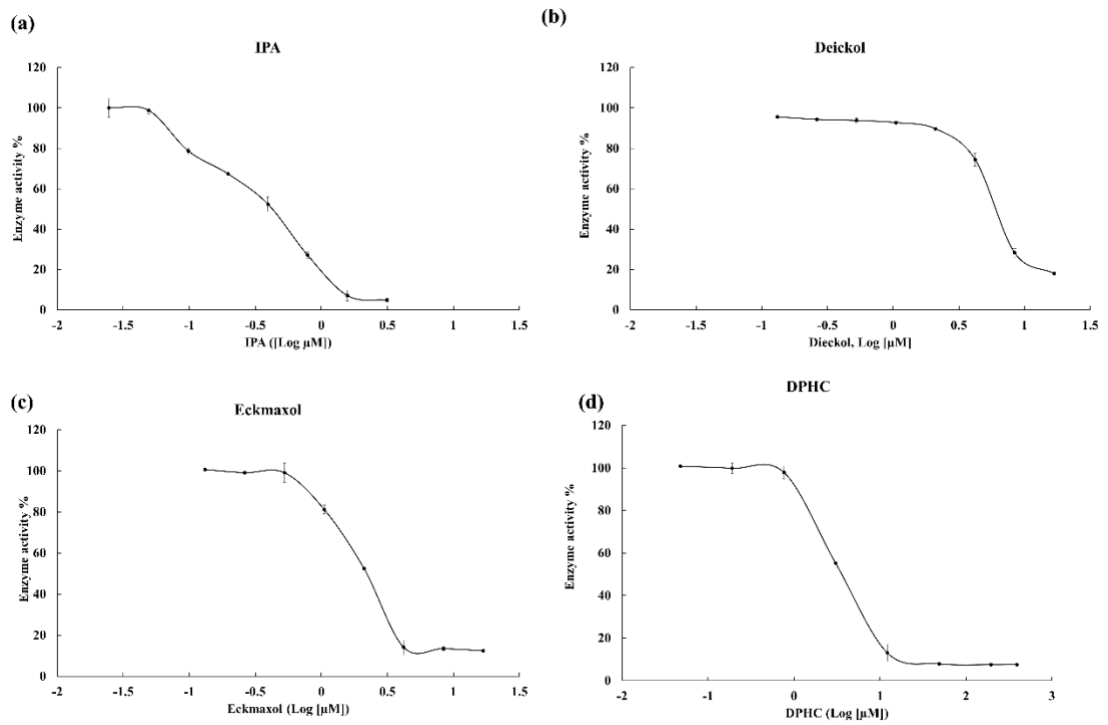


Fig. 17. In-vitro evaluation of 3CL^{pro}. Effect of (a) Ishophloroglucin A (IPA), (b) Dieckol, (c) Eckmaxol, and (d) Diphlorethohydroxycarmalol (DPHC) on the activity of SARS-CoV-2 3CL^{pro} and enzyme kinetic activity.

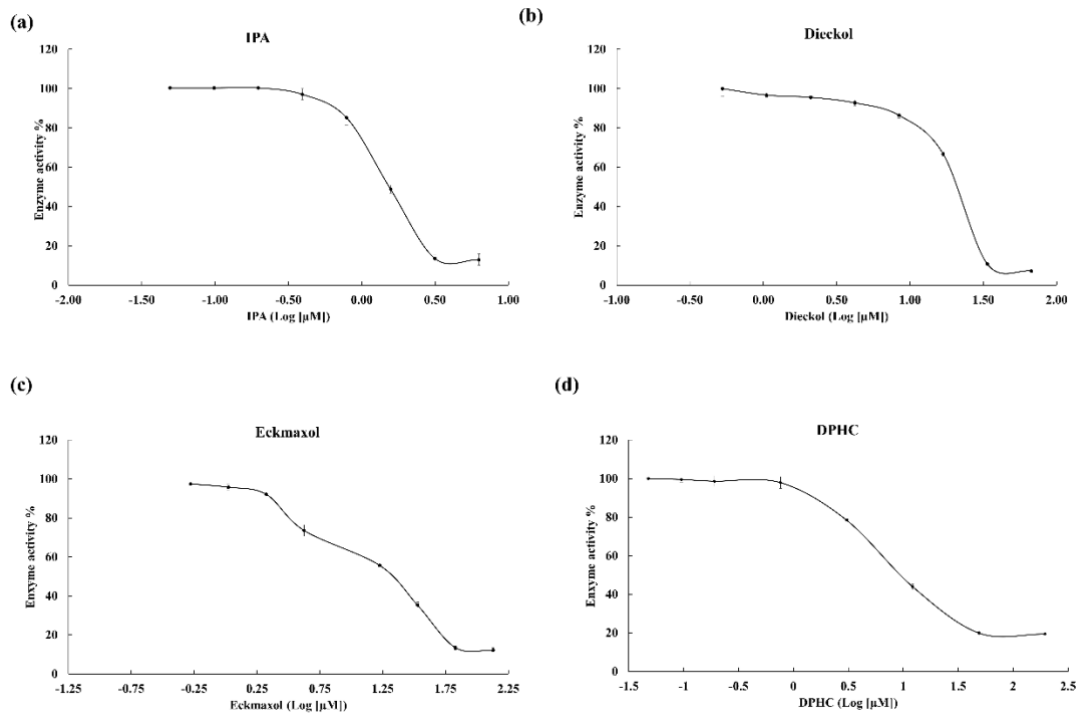


Fig. 18. In-vitro evaluation of PL^{pro}. Effect of (a) Ishophloroglucin A (IPA), (b) Dieckol, (c) Eckmaxol, and (d) Diphlorethohydroxycarmalol (DPHC) on the activity of SARS-CoV-2 PL^{pro} and enzyme kinetic activity.

3.4 Line-weaver Burk Plot

The inhibition data were plotted in the Line-weaver Burk plot, which determines the mode of inhibition. The V_{max} of all compounds was unchanged, and K_m was increased with the inhibitor concentration. This revealed that IPA, DPHC, Dieckol, and Eckmaxol inhibited 3CLpro and PLpro as competitive inhibitors (Fig. 19 and 20).

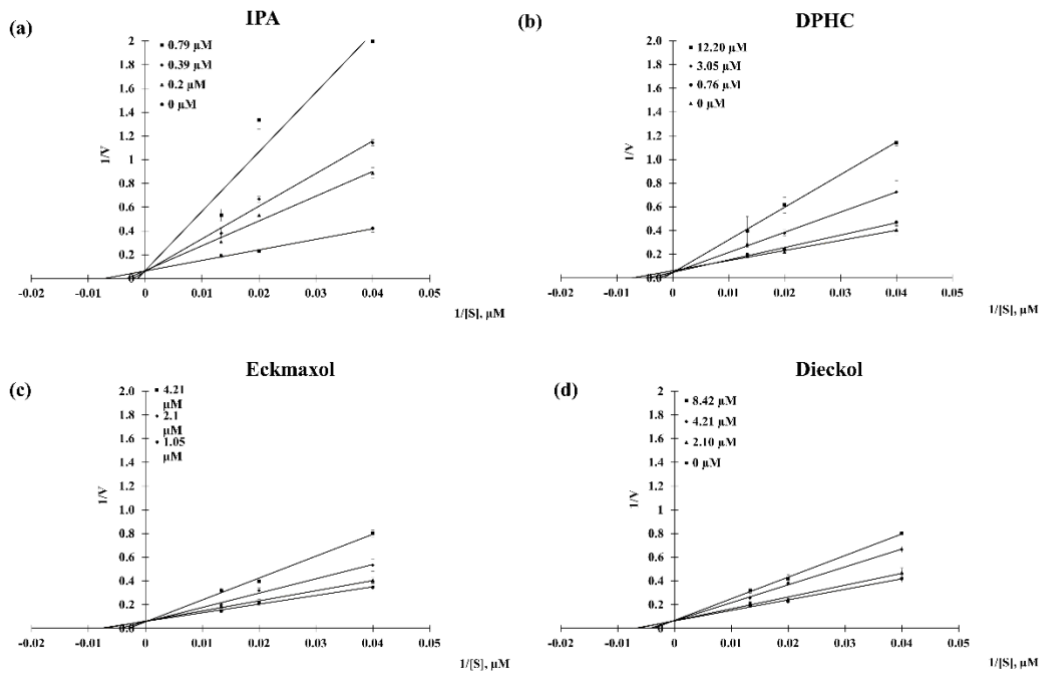


Fig. 19. Line-weaver Burk plot of (a) Ishophloroglucin A (IPA), (b) Diphlorethohydroxycarmalol (DPHC), (c) Eckmaxol, and (d) Dieckol on the activity of SARS-CoV-2 3CL^{pro}.

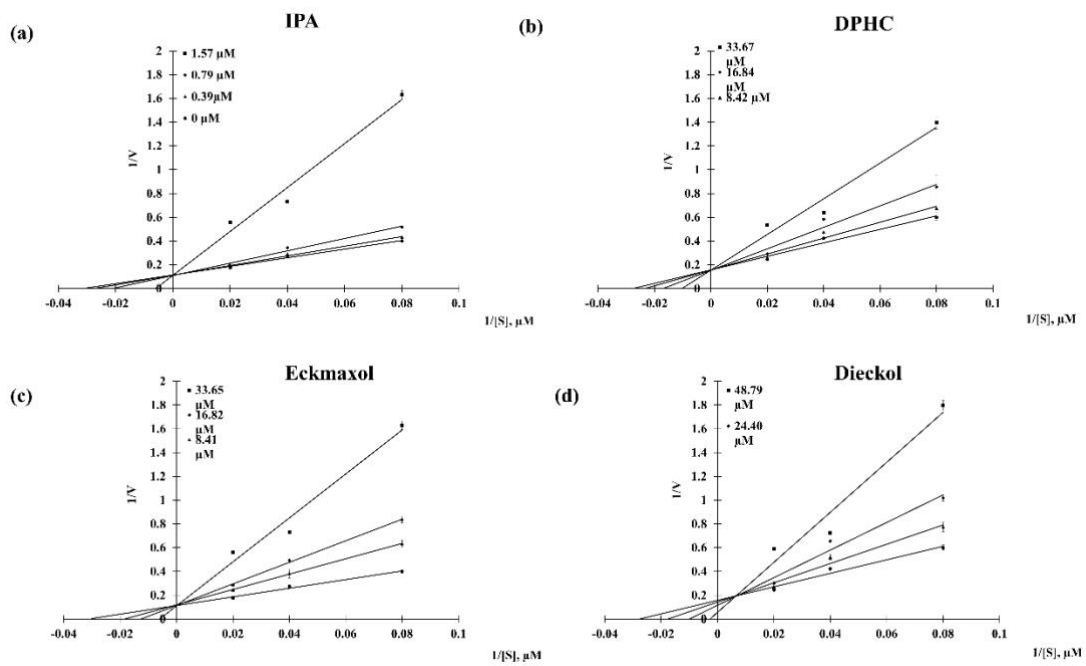


Fig. 20. Line-weaver Burk plot of (a) Ishophloroglucin A (IPA), (b) Diphlorethohydroxycarmalol (DPHC), (c) Eckmaxol, and (d) Dieckol on the activity of SARS-CoV-2 PL^{pro}.

3.5 Cell-Based Inhibition of 3CL^{pro} and PL^{pro}

A cell-based inhibition assay for 3CL^{pro} and PL^{pro} was subsequently performed to confirm the molecular docking activity and in vitro assay kit results. The selected MNP concentrations were non-toxic to the Vero E-6 cells. All MNPs were dissolved in DMSO and diluted using 1X phosphate-buffered saline. The final DMSO concentration in the highest diluted MNP concentration was less than 1%.

All MNPs successfully inhibited the proteolytic activity of 3CL^{pro} and PL^{pro} in a dose-dependent manner. IPA exhibited significant and dose-dependent inhibitory activity against 3CL^{pro} and PL^{pro} at 6.29–75.52 μ M and 12.59–75.52 μ M, respectively. Furthermore, IPA showed the most significant inhibitory activity against the proteolytic activity of 3CL^{pro} and PL^{pro} compared to other MNPs. Moreover, DPHC, Eckmaxol, and Dieckol showed significant and dose-dependent inhibitory activities (Fig. 21).

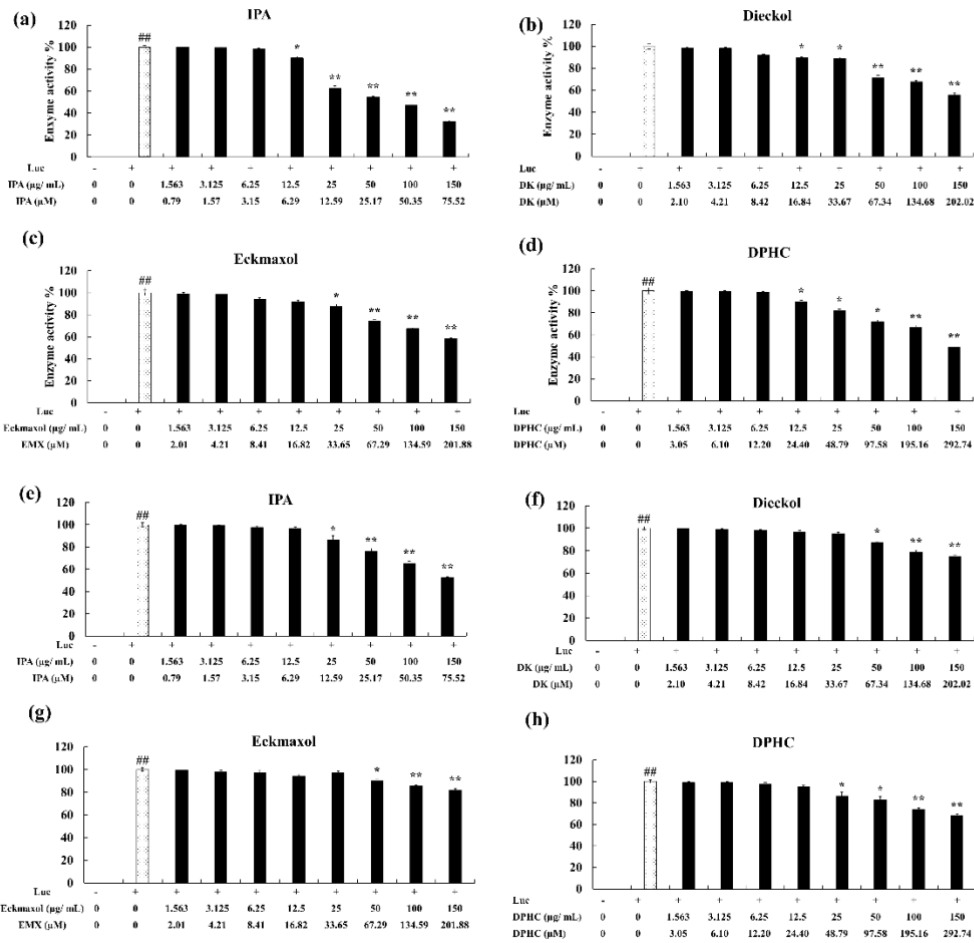


Fig 21. Cell-based 3CL^{pro} inhibitory activity of (a) Ishophloroglucin A (IPA), (b) Dieckol, (c) Eckmaxol, and (d) Diphlorethohydroxycarmalol (DPHC) and Cell-based PL^{pro} inhibitory activity of (e) Ishophloroglucin A (IPA), (f) Dieckol, (g) Eckmaxol, and (h) Diphlorethohydroxycarmalol (DPHC).

3.6 Cytopathic Effect (CPE) Reduction potential

According to the CPE reduction assay results, IPA, DPHC, and Eckmaxol expressed great CPE reduction activity at 6.25 μM against SARS-CoV-2 compared to Dieckol. DPHC exhibited the most excellent CPE reduction activity at 25 μM . Furthermore, Dieckol presented a dose-dependent inhibitory activity against SARS-COV-2 (Fig. 22).

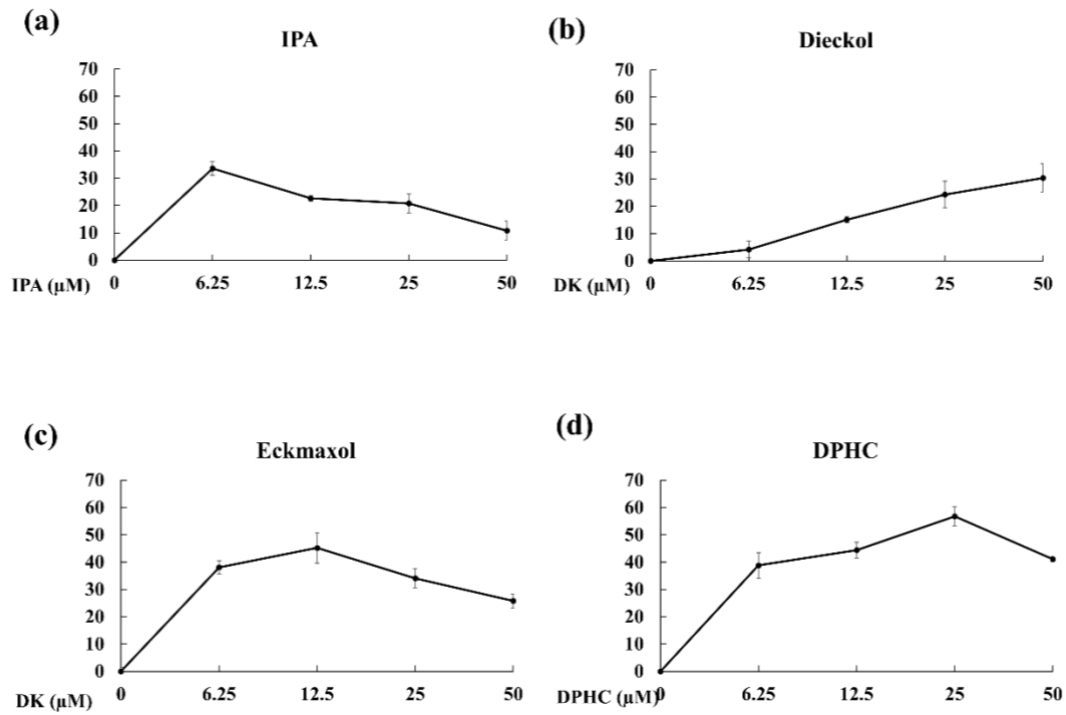


Fig 22. Inhibitory activity of Cytopathic effect induced by SARS-CoV-2 (a) Ishophloroglucin A (IPA), (b) Dieckol, (c) Eckmaxol, and (d) Diphlorethohydroxycarmalol (DPHC).

4. Discussion

The emergence of COVID-19 in December 2019 resulted in a pandemic that was responsible for millions of deaths. The health sector developed several vaccines and attempted to repurpose US Food and Drug Administration (FDA)-approved drugs. However, these attempts were insufficient to eliminate COVID-19, and most vaccines failed due to viral mutations. This emphasized the development of an antiviral agent to be used against SARS-CoV-2. In the various studies that provide insights into developing an antiviral agent for SARS-CoV-2, such as computational studies, in vitro, in vivo, and clinical trials can be observed. However, the authors of the present study attempted to develop an antiviral agent for several drug targets, and this multi-target approach was more successful than inhibiting individual drug targets.

The present study used Discovery Studio software to perform the initial screening. The “Prepare protein” tool of the software successfully prepared the structures of 3CLpro and PLpro using 6LU7 and 7CMD structures of PDB. The “Prepare protein” tool was utilized to solve the most common problems, such as removing alternate conformations, removing heteroatoms, and hydrogen additions, and correcting missing or incorrectly specified residues. The energy minimization of target receptor proteins was performed using the “Protein minimization” tool. DS provides three options to prepare the binding site of the receptor protein: “based on the PDB site records,” “from receptor cavities,” and “current form selection.” The present study used the final tool based on the available ligands of the crystal structures and previously published data. The molecular docking results reveal that compounds IPA, DPHC, Dieckol, and Eckmaxol showed the most significant binding affinity to the active sites of 3CLpro and PLpro. Therefore, these compounds were selected for further analysis.

The current study used an in vitro assay kit that was specially designed to determine 3CLpro and PLpro inhibitions. The isolated polyphenolic compounds were utilized to determine inhibitory activity against 3CLpro and PLpro. All of the tested compounds exhibited dose-dependent inhibitory activity against 3CLpro and PLpro. GC376 (IC₅₀ 0.4231 μM) and GRL0617 (IC₅₀ 1.5 μM) were used as positive controls against 3CLpro and PLpro, respectively [14, 31, 32]. Among these compounds, IPA presented remarkable inhibitory activity against proteases 3CLpro and PLpro with IC₅₀ values of 0.4814 and 1.4048 μM, respectively.

Furthermore, DPHC, Dieckol, and Eckmaxol also exhibited significant inhibitory activity. These results strengthen the in-silico outcomes. The binding affinity of these compounds was evaluated based on the active site of the protease enzymes. Thus, according to the enzyme kinetic results, a Line-weaver Burk plot was created to determine the inhibitory patterns by increasing K_m and constant V_{max} with the increasing compound concentration. This confirmed that all compounds were competitive inhibitors. These results also confirm the in-silico results that all the compounds are bound to the active site of the protease enzymes.

3CLpro and PLpro inhibitions were evaluated further using a cell-based inhibitory assay. This method did not require protein purification and was close to the natural physiological state. Thus, this method can be successfully used to strengthen the previous results. The in-frame construction of 3CLpro or PLpro with the substrate (the peptide sequence that contained a cleavage site) and firefly luciferase gene was designed as the plasmid transfected into the Vero E-9 cells. Usually, this method should be performed as a co-transfection process using the indicated vector. However, it can affect the accuracy

of the final results. Therefore, we used a vector that contained both renilla and firefly luciferases.

Furthermore, renilla luciferase was expressed independently from the protease gene or firefly luciferase. Thus, the luminescence from the firefly luciferase can be normalized using renilla luciferase expression. The luciferase protein bound to another protein with a value greater than 33 kDa remarkably decreased the luciferase activity [33]. Thus, a peptide sequence containing a cleavage site for 3CLpro or PLpro was used to bind the protease enzyme with the firefly luciferase. Thus, the inhibitory activity of MPNs downregulated the luciferase activity [34] and did not interfere with renilla luciferase activity. These results also exhibit the significant inhibitory activity of MNPs against 3CLpro and PLpro. However, the IC₅₀ values of the results present a significant difference compared to the *in vitro* assay kit. The permeability of the compounds and cell membrane could be the reason for the results we obtained [35]. Furthermore, the results confirm that IPA is the most efficient inhibitor of both proteases. SARS-CoV-2 can affect cells in numerous organs and systems in the human body and primarily infects the upper and lower respiratory tracts. Among them, the lungs are the most infected organ due to the presence of ACE-2 receptors [36]. Therefore, the CPE of the virus on these tissues and the reduction in CPE are essential factors. The CPE reduction evaluation is a commonly used assay format for screening antiviral agents. The cell death caused by viral infection was measured using this assay [37]. The CPE reduction effect of all compounds against the virus was evaluated, and among them, IPA, DPHC, and Eckmaxol exhibited remarkable CPE reduction activity. However, further studies are required to reveal and confirm the exact behavior of these compounds in an *in vivo* model.

5. Conclusion

In this study, we first reported the potential of polyphenolic compounds isolated from brown marine algae as an inhibitor against SARS-CoV-2 using two main drug targets that play a pivotal role in viral replication and survival in the host cell. The binding affinity of the selected molecules was evaluated using a molecular docking study. The in-silico results reveal interesting molecules that have the potential to bind with the active site of each protein. The inhibition activities of isolated compounds against 3CLpro and PLpro were assessed with a molecular in vitro biological assay kit and cell-based inhibition. The results show that all four compounds significantly downregulate the proteolytic activity of 3CLpro, and PLpro is significantly downregulated. Additionally, the potential of IPA as the most potent inhibitor through the multiple approaches against SARS-CoV-2 was identified. The CPE reduction assay reinforced these outcomes.

Part II: Polyphenolic Compounds Isolated from Marine Algae inhibit the SARS-CoV-2 cell entry mechanism via disturbing SARS-CoV-2 spike proteins and angiotensin converting enzyme interaction

1. Introduction

Humankind has been attacked by three epidemics involving unidentified coronaviruses in the 21st century that belongs to the family Coronaviridae, which consists of a positive-sense single-stranded RNA (+ssRNA) genome. This family has a high recombination rate and genetic variability leading to easy distribution among humans and other animals, resulting in various coronavirus types in human and animal populations. Coronaviruses primarily target the respiratory system and cause mild respiratory diseases, acute pneumonia, and respiratory failure. In recent history, three severe pandemics have involved respiratory diseases caused by coronavirus. The most recent global pandemic was COVID-19, caused by severe acute respiratory syndrome (SARS-CoV-2), and the other two were regional epidemics, SARS-CoV and Middle East respiratory syndrome (MERS-CoV), in 2003 and 2012, respectively. The entire world was suffered from this pandemic, and continuing. Thus, rapid development of an antiviral drug against SARS-CoV-2 is still required. The traditional source for treating human ailments has long been natural substances derived from plants, animals, microorganisms, and minerals. Natural product drug research has been dramatically reinvigorated by recent advancements in analytical technology, spectroscopy, and high-throughput screening, with contributions from marine-based pharmaceuticals. The maritime environment is a unique resource that has a vast array of biological diversity and, if properly investigated, has the potential to produce ground-breaking treatments. As more substances derived from marine sources enter clinical trials, the influence of this discipline on the pharmaceutical business grows [38]. Many compounds are made from marine species for antiviral activity. Over 40 substances are commercially available in the pharmaceutical

markets, including prospective antiviral treatments or alternative antiviral medications. Many more are undergoing preclinical and clinical testing as potential antiviral medications [39]. The current exploration of the marine environment for compounds with significant pharmacological applications will be significantly accelerated by the growing interest in marine-derived antiviral compounds, and it will continue to be a promising strategy and a new trend for contemporary medicine.

Determination of the cell entry mechanism of coronavirus is important for evaluating the pathogenicity and infectivity of SARS-CoV-2 [40, 41]. Moreover, this is a key target for intervention strategies and host immune surveillance [41, 42]. The cell entry mechanism can be divided into three main phases. Initially, the viral attachment is conducted by a coronavirus via binding with the cell surface receptor of the host cells, which then enters the endosome and finally fuses lysosomal and viral membranes [41, 42]. The spike protein of mature coronavirus is a trimer consisting of three receptor-binding S1 heads placed on top of the S2 stalk. According to previous studies of SARS-CoV, ACE-2 is recognized as its receptor by the RBD of SARS-CoV S1 [43-45]. The RBD follows a specific mechanism that regularly switches between standing up and lying down positions to evade the immune response of the host cell [46, 47]. The SARS-CoV spike protein requires proteolytic activation at the S1/S2 boundary to fuse the membranes. Here, the S1 disunites, and S2 undergoes structural changes. The lysosomal proteases cathepsin and cell surface protease TMPRSS2 play major roles in activating the spike protein and cell entry mechanism [48, 49]. These specific factors of the cell entry mechanism lead to severe symptoms, rapid spread, and a high fatality rate in infected patients [50-52].

Recent studies have revealed that SARS-CoV-2 also recognizes ACE-2 as a receptor for cell entry, and these studies have guided the identification of critical functional characteristics between SARS-CoV and SARS-CoV-2 in receptor recognition [53-55]. The RBD of SARS-CoV-2 expresses a significantly higher binding affinity with ACE-2 than SARS-CoV [56]. However, there are conflicting reports from different studies on the binding affinity of SARS-CoV-2 RBD to ACE-2. As mentioned above, RBD follows standing up and laying down states to evade the immune response, and these states are associated with receptor binding affinity. Meanwhile, an interesting study regarding the cryo-electron microscopy structure of SARS-CoV-2 revealed that the RBD was mostly in the lying downstate, which shows ineffective binding with ACE-2 [57, 58]. Moreover, studies have confirmed the role of TMPRSS-2 and lysosomal proteases as protease activators in the cell entry mechanism of SARS-CoV-2 [59, 60].

As mentioned, the SARS-CoV spike protein consists of S1 and S2 subunits. This S1 unit facilitates the binding with ACE-2. However, the entry mechanism requires S protein priming. Therefore, cellular serine proteases such as TMPRSS2 and TMPRSS11D cleave the spike protein at the S1/S2 and S1 sites. This cleavage allows the fusion between spike protein and cellular membranes [61]. SARS-CoV-2 spike protein showed 76% to 78% sequence similarity for whole protein, 73% to 76% for RBD, and 50% to 53% for the RBM with SARS-CoV. Moreover, the similarity of spike protein between SARS-CoV and SARS-CoV-2 provides insight into sharing the same host receptor ACE-2. Further, the RBM of SARS-CoV-2 does not contain any insertion or deletion, and when considering about 14 residues of RBD that provide contact with the ACE-2 receptor, nine fully conserved residues, and four partially conserved residues can be identified between the mentioned two strains [62]. Hence, inhibiting binding between the RBD of SARS-

CoV-2 and ACE-2 receptor can be identified as a potential way to inhibit the SARS-CoV-2 infection.

The present study aims to inhibit SARS-CoV-2 through 3CLpro, PLpro, and ACE-2: SARS-CoV-2 spike protein binding using natural products isolated from marine algae. This part of the study investigated the inhibitory potential of these marine natural compounds. Molecular docking was utilized to initially screen selected natural products based on the ACE-2 protein structures. Moreover, the resulting compounds were isolated and used for biological assays to confirm the inhibition activity further. To the best of our knowledge, this is the first report concerning the assessment of marine natural products on 3CLpro, PLpro, and ACE-2 of SARS-CoV-2.

2. Methods and Materials

2.1 Chemicals and reagents

Dimethylsulfoxide (DMSO) and All the organic solvents (HPLC grade) used in the experiments were purchased from Sigma-Aldrich (St Louis, MO, USA). The in-vitro inhibition assay kits for ACE-2: SARS-CoV-2 spike, was purchased from AMSBIO company (Madrid, Spain). NL4-3 mCherry Luciferase plasmid (Cat #44965), pcDNA3.1-SARS2-Spike plasmid (Cat #145032), and pLENTI_hACE2_PURO (Cat #155295) were purchased from addgene (Watertown, Massachusetts, USA). Dulbecco's modified Eagle's medium (DMEM) was purchased from Gibco/BRL (Burlington, ON, Canada), 10% fetal bovine serum (FBS) and 5% penicillin/streptomycin were purchased from WELGENE (Gyeongsan, Korea), and 3-(4,5-Dimethylthiazol-2-yl)-2,5-diphenyltetrazolium bromide (MTT) was purchased from Sigma Aldrich (St. Lois, MO, USA). HEK293T cells were purchased from the American Type Culture Collection (ATCC, Manassas, VA, USA. X-tremeGENE™ HP DNA Transfection Reagent was purchased from Sigma-Aldrich (St Louis, MO, USA)

2.2 Preparation of Receptors

The protein Data Bank (PDB) (<http://www.pdb.org>) was used to obtain crystal structures of ACE-2 under PDB ID: 6LZG. The molecular docking studies were conducted using Discovery Studio (DS-Client v18.1.100.18065). Briefly, the crystal structure of each protein was downloaded from the PDB and opened in the DS. The water molecules and heteroatoms were removed, and the "Clean protein" tool was used to correct minor problems, such as missing-side chain atoms, which were added in an extended confirmation.

The "Prepare protein" tool was utilized to solve most common problems, such as removing alternate conformations, heteroatoms, hydrogens addition, and correcting missing or incorrectly specified residues. The energy minimization of target receptor proteins was performed using the "Protein minimization" tool. DS provides three options to prepare the binding site of the receptor protein, "based on the PDB site records," "from receptor cavities," and "current form selection." The present study used the last tool based on the available ligands of the crystal structures and previously published data. ACE-2 was available in PDB as a complex with SARS-CoV-2 spike protein. The chain B SARS-CoV-2 spike protein was removed, and the binding site was determined based on the previous studies [63]. Briefly, the binding site was prepared as a grid in the crystal structure's ligand binding site, and the target proteins' prepared binding sites were identified by specifying a sphere of a given radius located in the active site. The geometric center of the ligand in the crystal structure was used as the center of the sphere. Python-enhanced molecular graphics tool (PyMOL, version 2.4.1) was used to calculate the root-mean-square deviation of atomic position (RMSD) value of the prepared ACE-2 structure to determine any significant difference between them.

2.3. Preparation of ligands

The ligands were 16 compounds from marine algae. The 3D structure of each compound was generated, and hydrogen atoms were added. The ligand's energy was minimized using the "Clean geometry" tool and applied CHARMM force field. The final ligand structure generated by the "Prepare ligand" tool was optimized using DS ligand optimization. The summary of the ligands used in this study is shown in Fig. 1 of part I.

2.4 Molecular docking

Docking of the selected ligands with prepared proteins was performed using DS. The crystal structure of ACE-2 bound with the receptor binding domain (RBD) of SARS-CoV-2 spike protein was reproduced, and the RMSD value between the raw crystal structure and docking results was calculated to confirm the accuracy of the process. Initially, Flexible docking experiments were performed using the 3D crystal structure of ACE-2. Flexible docking is a fully automated workflow. The flexible docking protocol allows for receptor flexibility during the docking of flexible ligands. The side chains of specified amino acids in the target receptor protein are allowed to move during docking.

Moreover, the receptor was adapted to different ligands in an induced-fit model. Therefore, flexible docking was performed to determine the ligand's suitable orientation in each receptor protein's active site. The results from the flexible docking were used to calculate the binding energy between each ligand and receptor proteins using CHARMM-based energy. The free energy of the complex, the ligand, and the receptor was used to calculate the free energy of binding. $\text{Energy binding} = \text{Energy Complex} - (\text{Energy Ligand} + \text{Energy Receptor})$

The three ligands were selected for biological assays based on the results of molecular docking.

2.5 Sample collection and extraction

The extraction and purification procedure of the samples were explained in part I.

2.6 Inhibition assay in binding of ACE-2 receptor and SARS-CoV-2 spike protein

The inhibitory potential of isolated compounds in the binding of ACE-2: SARS-CoV-2 spike protein was evaluated using an ACE-2: SARS-CoV-2 inhibitor screening assay kit

(AMSBIO, Madrid, Spain). Briefly, 50ng of his-tagged ACE-2 protein was added to the nickel-coated well and blocked using a blocking buffer. The isolated compounds IPA, Eckmaxol, and Dieckol were added to each well except for blank and positive control. Finally, 20 ng of spike protein was added to each well except for blank and incubated 1h under room temperature with slow shaking. The Fc-tagged spike protein was detected using HRP-labelled anti-Mouse-Fc. The luminescence which emits due to the chemical reaction was detected using Synergy HTX multi-mode microplate reader (Vermont, USA). Chemiluminescence detection was performed without a selected wavelength because this method used emission photometry. The enhanced chemiluminescence was measured using Synergy HTX multi-mode microplate reader (Vermont, USA). The IC50 value of each compound was calculated, and the experimental data were fit to a logistic curve with the below-mentioned equation.

$$\text{Enzyme activity \%} = [S - B] / [P - B] * 100\%$$

“B” is the fluorescence of control (substrate and assay buffer), “P” is the fluorescence of positive control (substrate and enzyme), and “S” is the fluorescence of the tested sample.

2.7 SARS-CoV-2 pseudovirus production

2.7.1 Cell culture

The human embryonic kidney epithelial cell line HEK293T (ATCC, CRL-3216) and human lung epithelial cell line A549 (ATCC, CCL-185) were cultured in Dulbecco’s modified Eagle’s medium (DMEM; high glucose, Sigma-Aldrich) supplemented with 10% (v/v) fetal bovine serum (FBS) (Sigma-Aldrich) and 1% (v/v) PenStrep (Sigma-Aldrich) and maintained in a 5% CO₂ incubator at 37°C.

2.7.2 Gene transfection for the development of pseudovirus

HEK293T cells were inoculated in cell dishes and grown overnight at 37°C with 5%

CO₂ until the confluence for adherent cells reached 70–90%. The recombinant spike protein expression plasmid pcDNA3.1-SARS2-Spike was co-transfected with HIV backbone vector NLM-3 mCherry Luciferase plasmid. The experimental procedure is summarized in Fig 1. The mentioned plasmids were co-transfected in different ratios (spike protein plasmid: HIV backbone plasmid ratios; 1:0.1, 1:1, 1:10, 1:100, and 1:500) to determine the optimum plasmid ratio to obtain maximum pseudovirus particles. The plasmids were transfected with X-tremeGENE™ HP DNA Transfection Reagent according to the instruction from the manufacturer. After 48h, SARS-CoV-2 pseudovirus was collected and passed through a 0.45 µm filter and stored at -80 °C [64].

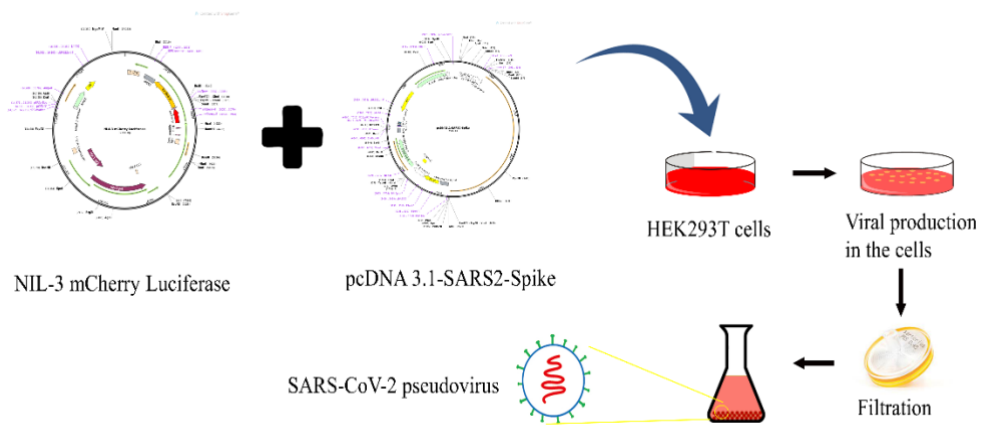


Fig. 1. Experimental procedure of SARS-CoV-2 pseudovirus production.

2.7.3 Evaluating of the titter of the pseudovirus

The qPCR was performed with the dilution series of the NLM-3 mCherry Luciferase plasmid with the primers designed for the mCherry gene. Then the standard curve was developed using the Ct(cp) value of the qPCR against the log value of the plasmid amount. The below-mentioned equation was utilized to convert the plasmid amount to the copy number. (Fig 2)

$$\text{Number of copies (molecules)} = \frac{\mathbf{X} \text{ ng} * 6.022 \times 10^{23} \text{ molecules/ mole}}{(\mathbf{N} * 660\text{g/ mole}) * 1 \times 10^9 \text{ ng/ g}}$$

X = amount of amplicon (ng)

N = length of the dsDNA amplicon

660 g/mole = average mass of 1bp ds DNA

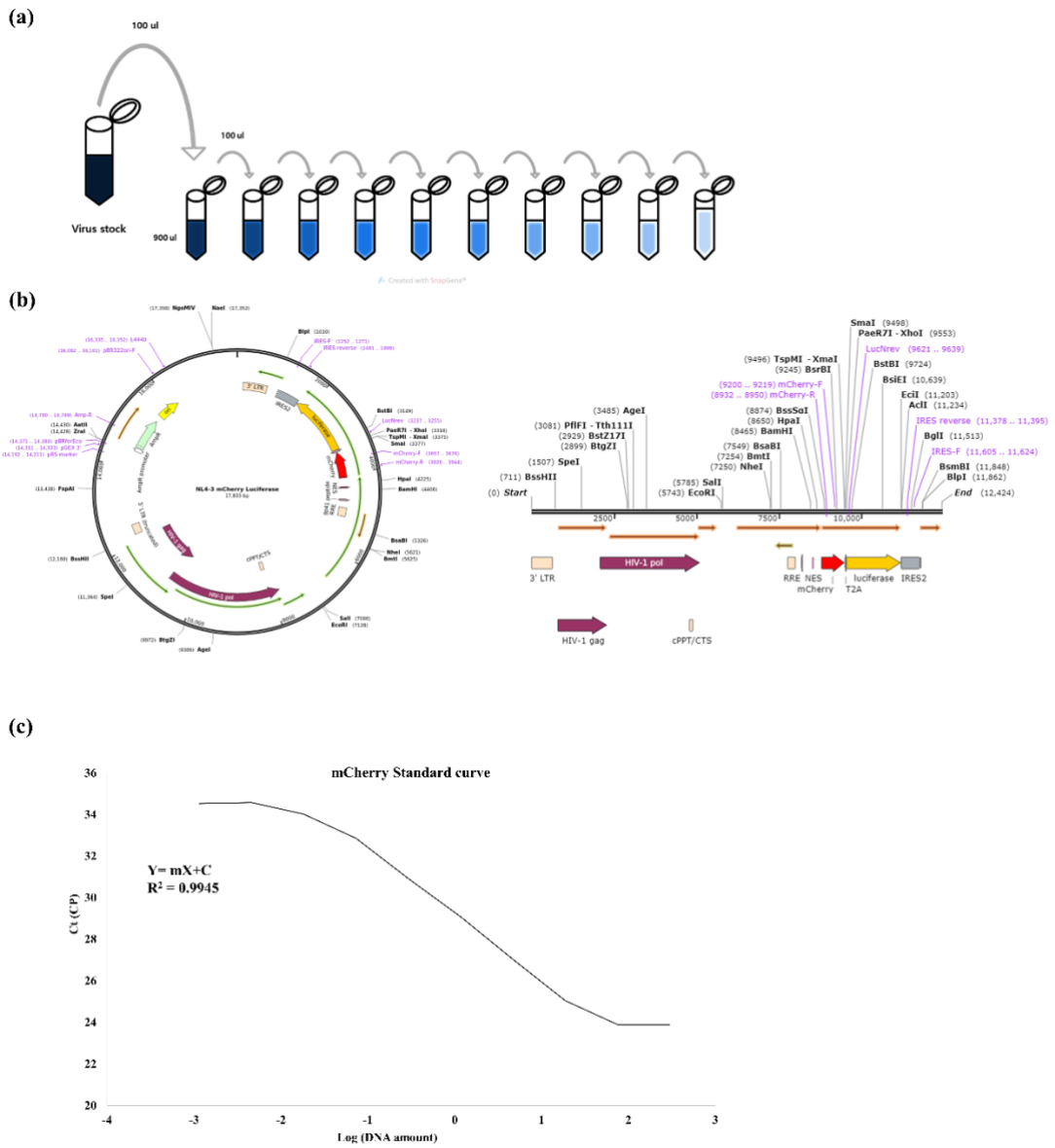


Fig. 2. Experimental procedure for evaluating virus titer. (a) dilution series of mCherry gene and (b) standard curve of mCherry gene, and (c) standard curve.

2.7.4 Infection of the pseudovirus to the HEK293T-ACE-2 cells

HEK293T-ACE-2 cells were seeded in 48 well-plates in 1×10^5 cells/ mL concentration. Then 100 μ L pseudovirus was treated after 48 hr in the presence of 4mg/ mL polybrene, and they were incubated at 37 °C and 5% CO₂ for 24 h. This medium was then replaced with fresh medium, and the cells were allowed to recover at 37 °C and CO₂. The cells were washed with PBS before observing the mCherry luminescence [65]. The fluorescence was evaluated at different time gaps from the pseudovirus treatment to obtain the maximum mCherry fluorescence.

The sample's inhibitory activity was evaluated by seeding HEK293T-ACE-2 cells in 48 well-plates at 1×10^5 cells/ mL concentration, and samples were treated after 24h incubation and provided another 1h incubation at 37 °C and CO₂. Then pseudovirus was treated, and the cell culture media was changed to fresh media after 24h incubation. Then mCherry fluorescent was obtained after 52h from the viral treatment. The fluorescence intensity was calculated using ImageJ software.

2.8 In-vivo evaluation of the inhibitory potential of polyphenolic compounds against SARS-CoV-2 cell entry

Zebrafish larvae at three days' post-fertilization (dpf) were transferred to the 96 well-plate, and each well contained one larva in 100 μ L of embryo media. Then samples were treated and incubated for another 6h. Then 10 μ L of pseudovirus was treated to each well and incubated at 28 °C for 72 h until they reached ~ 6.25 dpf. The larvae from each treatment group were pooled and washed with Milli-Q water for 6×20 min with gentle agitation prior to RNA extraction [66]. The experimental procedure was summarized in Fig 3.

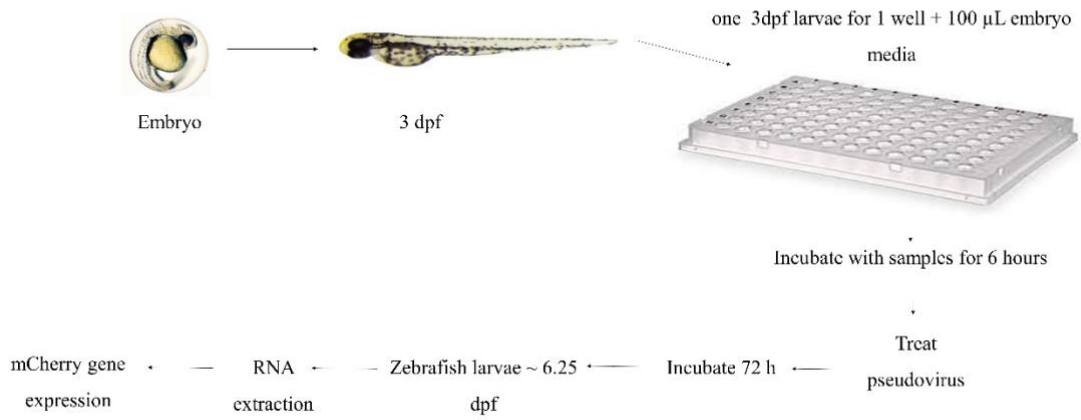


Fig. 3. Experimental procedure of in-vivo evaluation of SARS-CoV-2 pseudovirus cell entry.

2.8.1 RNA extraction, reverse transcription and RT-qPCR

The total RNA from the pseudovirus-infected zebrafish was extracted using a Tri-Reagent™ extraction kit (Sigma Aldrich, St. Louis, MO, USA). The RNA samples were transcribed using a cDNA Reverse Transcription Kit (Takara, Shiga, Japan). RT-qPCR amplification reactions of cDNA were conducted using a Thermal Cycler Dice Real-Time System (Takara, Japan) in the following manner: enzyme activation at 95 °C for 10 s, followed by 40 cycles of denaturation at 95 °C for 5 s, and annealing at 58 °C for 10 s. The reaction was carried out in a 10 µL volume containing 3 µL of cDNA, 5 µL of the 2x TaKaRa ExTaq SYBR premix (TaKaRa, BIO INC, Japan), 0.4 µL of mCherry primer, and 12 µL of RNase/DNase-free water. Using GAPDH as an internal reference standard gene in the amplification process, the mCherry expression levels were evaluated. The primers used in the experiment are; forward 5'-CCCCGTAATGCAGAAGAAGA-3' and reverse 5'-TTGGTCACCTTCAGCTTGG-3'.

2.9 Statistical analysis

All experiment results were expressed as the mean value with the standard deviation of three independent recurrences. The significant differences of all statistical data were analysed via one-way analysis of variance according to Duncan's multiple range test using the SPSS v. 20 (IBM Corp., Armonk, NY, USA).

3. Results

3.1 Receptor and ligand preparation

3.1.1. Structure of ACE-2 receptor protein preparation

The X-ray crystallography of the human ACE-2 receptor (PDB ID 6LZG) was obtained from PDB. The present structure was available as a complex with RBD of SARS-CoV-2 spike protein at a high resolution of 2.5°A. The total structure weight was 93.5kDa (Fig. 4a). The RBD of SARS-CoV-2 spike protein was bound to the human ACE-2 receptor through SER19, GLN24, PHE28, ASP30, LYS31, HIS34, ASP38, TYR41, GLN42, LEU79, MET82, TYR83, LYS353, ASP355 (Fig. 4b). The active site was prepared using these residues, and the binding site sphere was prepared with a 15Åradius. The prepared ACE-2 was superimposed with the original ACE-2 available in PBD using PyMOL, and the calculated RMSD value was 0.25 (Fig. 4c).

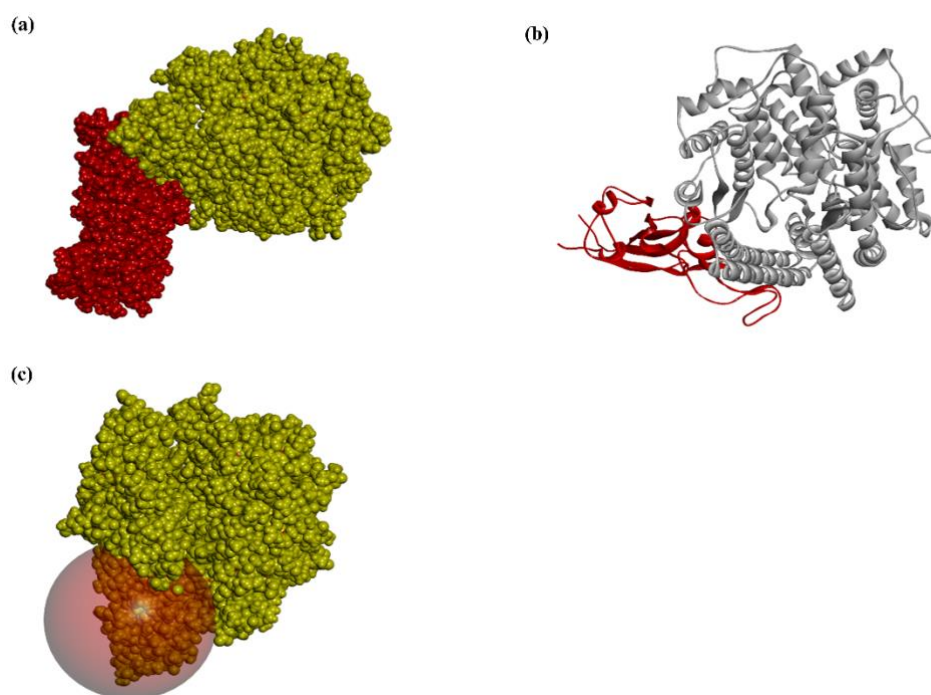


Fig. 4. Receptor preparation of ACE-2. a) Surface representation ACE-2: RBD of SARS-CoV-2 spike protein complex ACE-2. ACE-2 receptor protein is in yellow colour and RBD of SARS-CoV-2 is in red colour. b) Cartoon representation of ACE-2: RBD of SARS-CoV-2 spike protein complex. ACE-2 receptor protein is in yellow colour and RBD of SARS-CoV-2 is in red colour. c) Prepared active site of ACE-2.

3.1.2 Ligand preparation

Sixteen ligands were prepared using DS “Prepare ligand”, all the prepared ligand structures were summarized in Fig 8 of part I. The most stable ligand conformation was used for molecular docking.

3.2 Molecular docking

Molecular docking was performed between all ligands and ACE-2 receptor proteins. The corresponding dock scores are summarized in Table 1. According to the flexible docking, binding energy, and DS visualizer results, Ishophloroglucin A (IPA), Diphlorethohydroxycarmalol (DPHC), and Eckmaxol were selected for further studies.

Table 1. The cDocker interaction energies and free binding energies (Kcal/ mol) of selected ligands from marine algae with ACE-2 receptor protein.

No	Sample name	cDocker interaction energy (Kcal/mol)	Binding energy (Kcal/ mol)
1	Ishophloroglucinol A	-33.3206	-336.334
2	Diphlorethohydroxycarmalol	-114.898	-161.514
3	Dieckol	-44.5389	-178.6144
4	Phlorofucofuroeckol-A	-36.2067	-146.96
5	Nahocol A	-50.1917	-97.2917
6	Saringosterol	-35.8752	-66.8693
7	Sargacromanol E	-49.5546	-94.6006
8	Fucoxanthin	-	-

9	Eckmaxol	-68.572	-257.705
10	Fucosterol	-32.6457	-83.1795
11	Gallic acid	-16.4961	60.5235
12	Methyl gallate	-24.6816	-63.4524
13	Apo-9 fucoxanthinone	-	-
14	3-Buten-2-one,4-(4-hydroxy-2,2,6-trimethyl-7-oxabicyclo[4.1.0]hept-1-yl)-	-32.5717	-40.7664
15	Loliolide	-30.4983	-72.4829
16	Sargachromenol	-41.4074	-108.13

3.2.1. ACE-2 enzyme

IPA was stabilized with ACE-2 receptor via one conventional hydrogen bond through ARG393 with 2.28Å length and one pi-pi stacked bond through ALA386 with 5.10Å length. Furthermore, there are another two salt bridges that can be found between APA and HIS34 residue of ACE-2 with 1.78Å and 5.99Å lengths (Fig. 5).

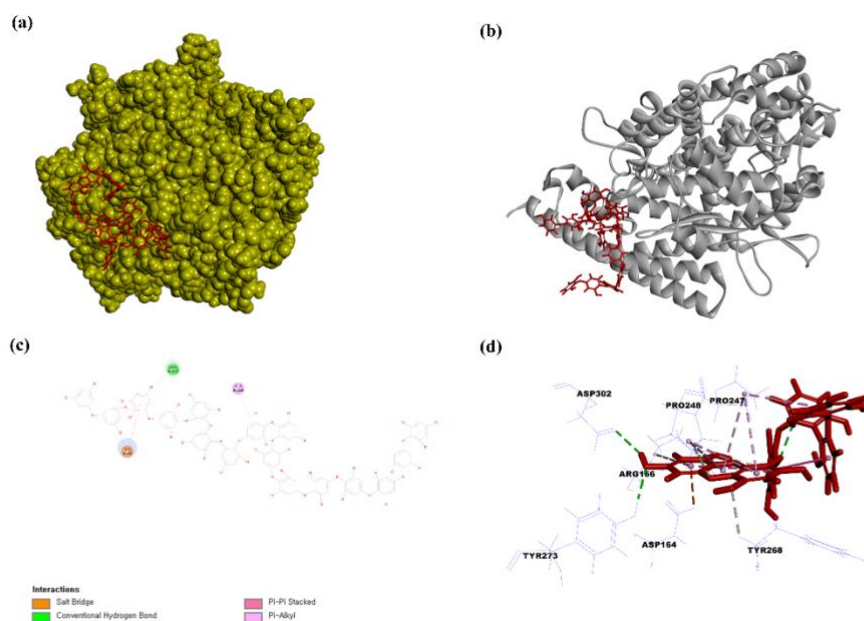


Fig. 5. In-silico evaluation of 3CL^{pro} with Ishophloroglucinol A (IPA). a) 3D representation of docking pose of IPA with ACE-2. b) Cartoon representation of docking pose of IPA with ACE-2. c) 2D representation of Ligand interaction of IPA with ACE-2. d) 3D representation of Ligand interaction of IPA with ACE-2.

DPHC was bound to the ACE-2 via one attractive charge and one pi-alkyl bond with LYS31 5.2 Å length. (Fig. 6).

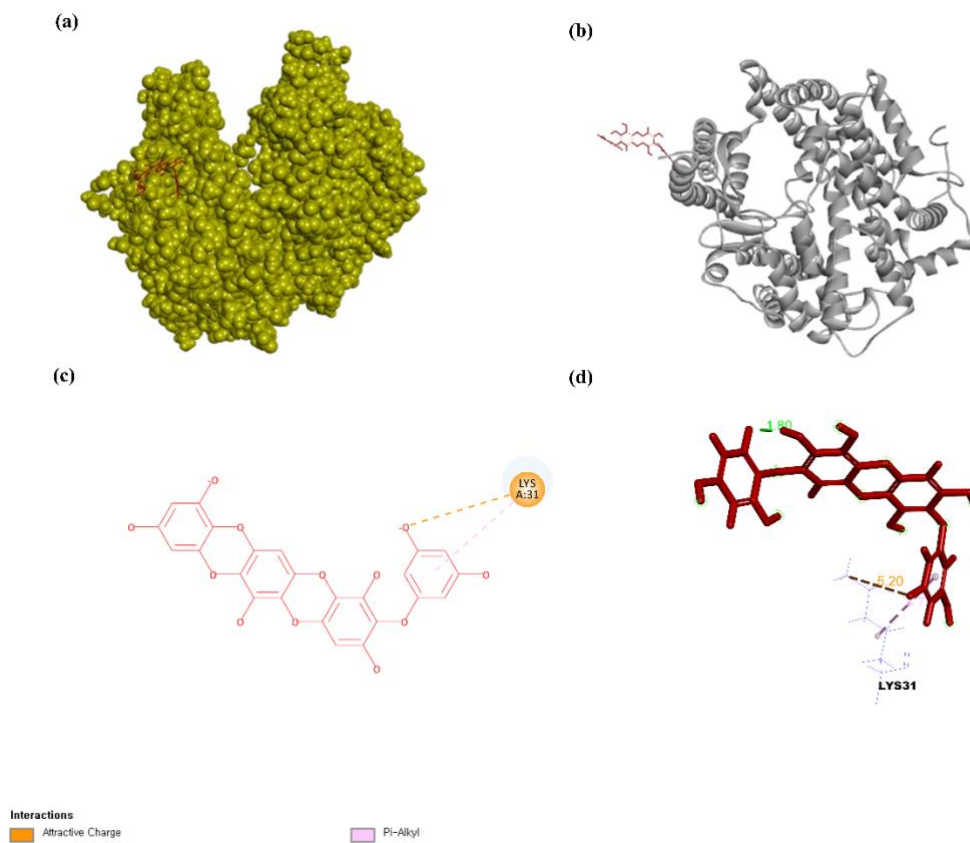


Fig. 6. In-silico evaluation of 3CL^{pro} with Diphloretohydroxycarmalol (DPHC) .a) 3D representation of docking pose of DPHC with ACE-2. **b)** Cartoon representation of docking pose of DPHC with ACE-2. **c)** 2D representation of Ligand interaction of DPHC with ACE-2. **d)** 3D representation of Ligand interaction of DPHC with ACE-2.

Eckmaxol was bound to the ACE-2 via three conventional hydrogen bonds through ASN397, ASP206, and GLY205 residues with 2.04Å, 1.97Å, and 1.97Å lengths, respectively. In addition, there is one pi-donor hydrogen bond with ASN394 residue, and the bond length was 2.60Å length. ALA99 residue of ACE-2 made a pi-alkyl bond with ALA99 4.33Å length. LYS562 residue made a salt bridge with Eckmaxol, and the bond length was 4.33Å (Fig. 7).

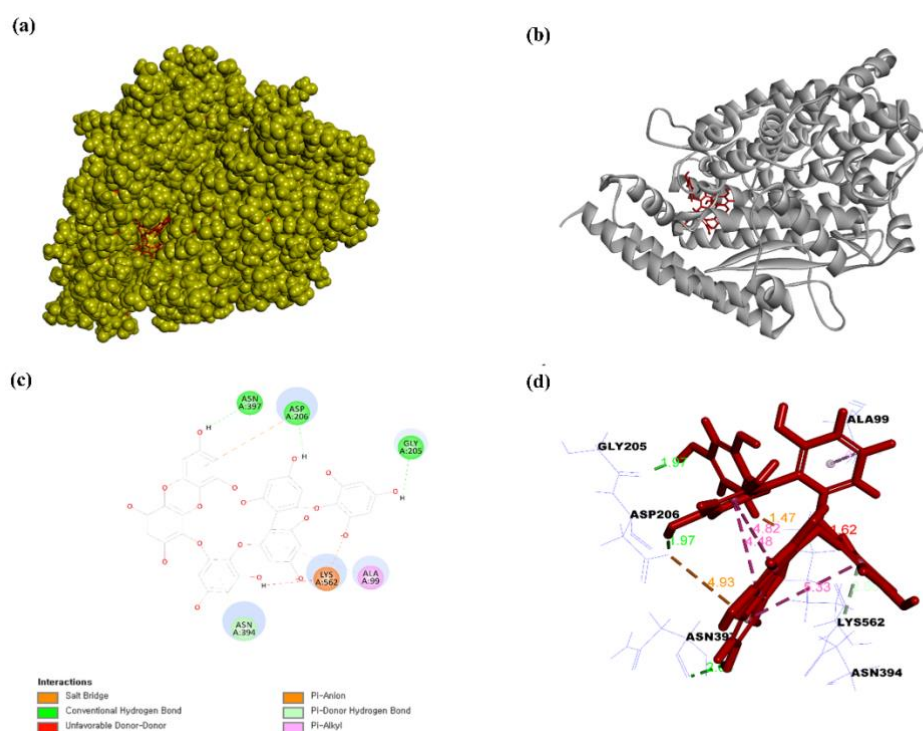


Fig. 7. In-silico evaluation of 3CL^{Pro} with Eckmaxol. a) 3D representation of docking pose of Eckmaxol with ACE-2. b) Cartoon representation of docking pose of Eckmaxol with ACE-2. c) 2D representation of Ligand interaction of Eckmaxol with ACE-2. d) 3D representation of Ligand interaction of Eckmaxol with ACE-2.

3.3 In-vitro inhibition of marine algal compounds

The inhibition of the cell entry mechanism of SARS-CoV-2 through the ACE-2 receptor was evaluated using the ACE-2: SARS-CoV-2 RBD binding inhibition assay kit. IPA, DPHC, and Eckmaxol significantly downregulated the binding between ACE-2 and SARS-CoV-2 (Fig. 8). The IC₅₀ values of each compound were summarized in Table 2.

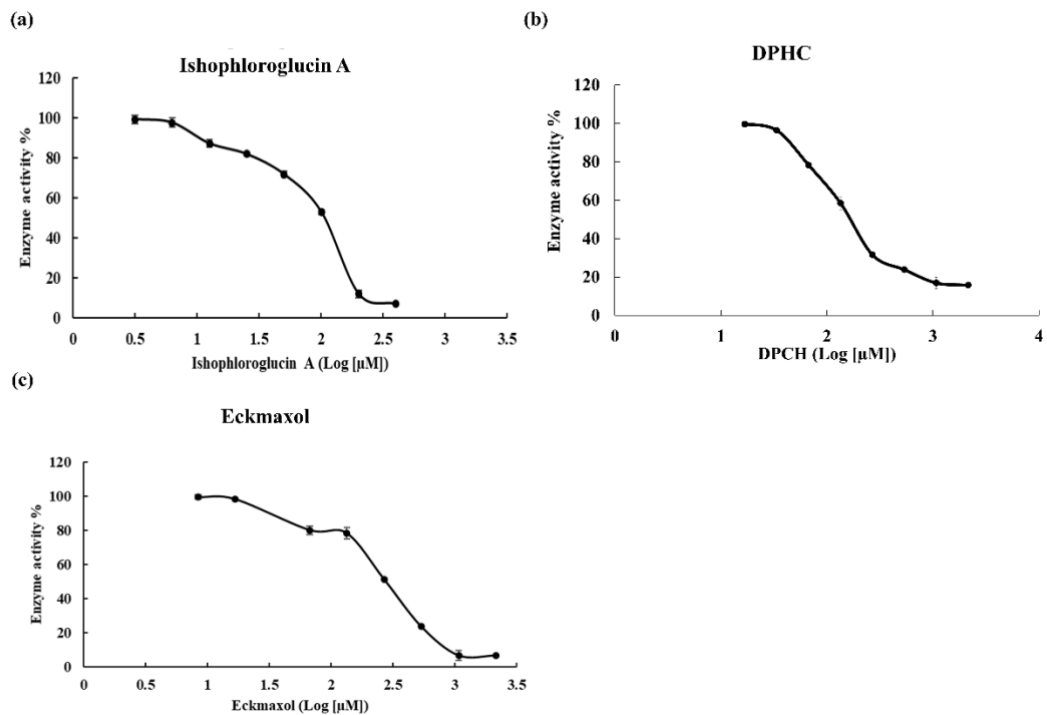


Fig. 8. In-vitro inhibition assay of the interaction between ACE-2: SARS-CoV-2 a) Ishophloroglucin A and b) Diphlorethohydroxycarmalol (DPHC), and c) Eckmaxol.

Table 2. Inhibitory activity of isolated compounds on the interactions of ACE-2: SARS-CoV-2 spike protein.

No	Drug target	Ligand	IC ₅₀ value
1		Ishophloroglucin A (IPA)	116.0303 ± 0.239
2	ACE-2	Diphlorethohydroxycarmalol (DPHC)	124.7286 ± 0.145
3		Eckmaxol	339.8811 ± 0.16

3.4 Inhibition of SARS-CoV-2 pseudovirus cell entry

3.4.1 Determination of pseudovirus production and virus titer

To generate the SARS-CoV-2 variant pseudoviruses, we used an HIV backbone vector-based pseudovirus packaging system. The HIV backbone vector, the pNL4-3 mCherry luciferase, was derived from pNL4-3 vector, in which the nef gene was replaced by the firefly luciferase gene and mCherry gene resulting in frame shifts in env and vpr. The recombinant spike protein expression plasmid pcDNA3.1-SARS2-Spike was co-transfected with different ratios and evaluated the virus titer at different time gaps to obtain the maximum virus titer. Based on the results, a 1:1 ratio of the plasmids provided the maximum pseudovirus titer at 48h after transfection, approximately 8×10^8 (Fig 9).

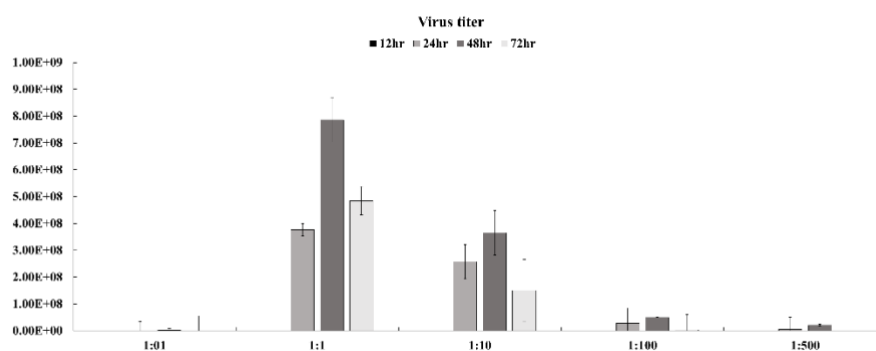


Fig. 9. Optimization of pseudovirus production.

The prepared pseudovirus was treated to the HEK293-T-ACE-2 cells and analyzed the mCherry fluorescence at different time points from the pseudoviral treatment. The results revealed that 52h after pseudovirus treatment provided significant mCherry fluorescence (Fig. 10a), The mCherry fluorescence results revealed IPA, DPHC, and Eckmaxol significantly downregulated the mCherry fluorescence that confirmed the inhibitory potential of SARS-CoV-2 viral cell entry mechanism (Fig 10b and c).

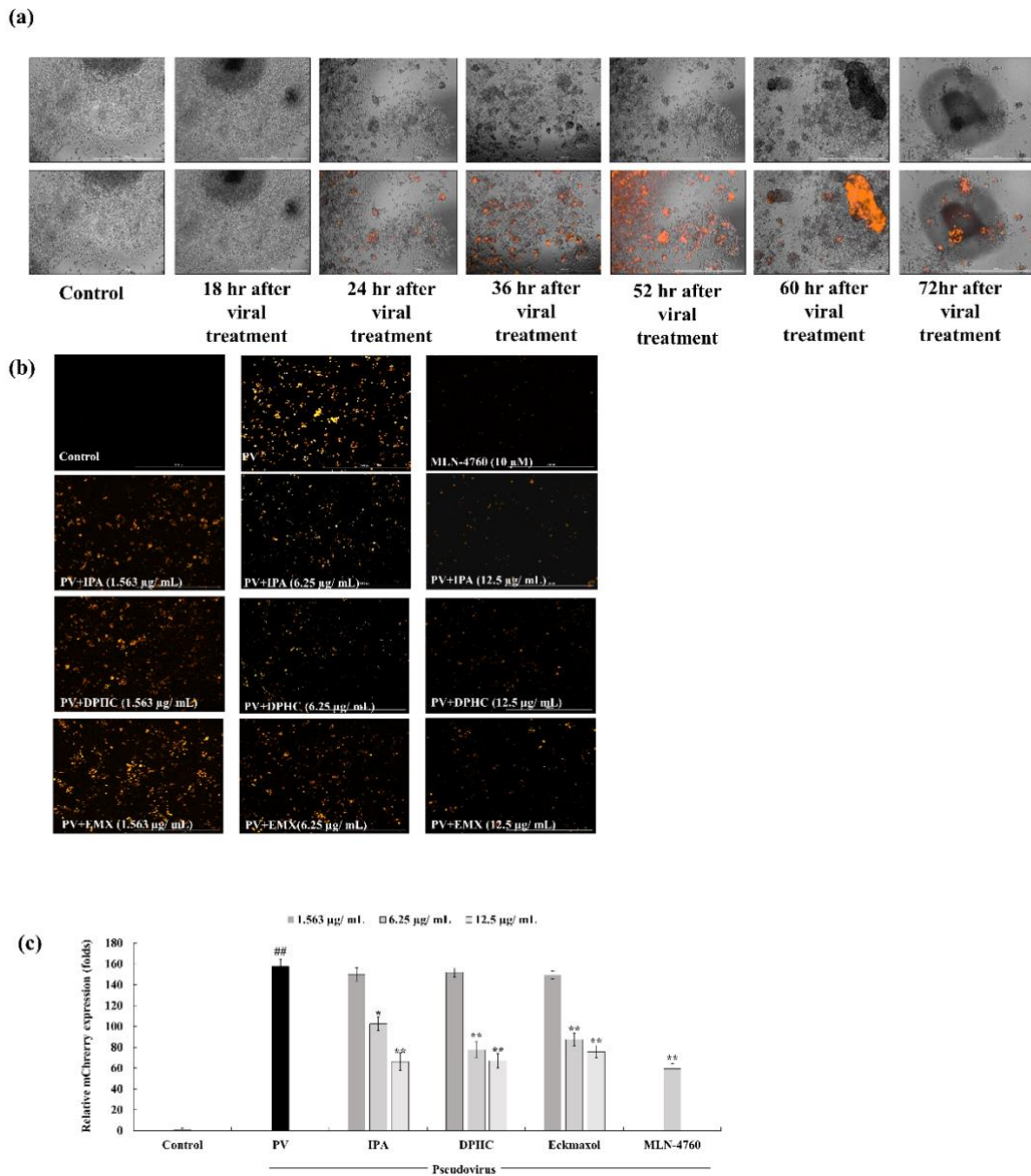


Fig. 10. Evaluation of the cell entry mechanism of SARS-CoV-2 pseudovirus (PV). (a) Optimization of the SARS-CoV-2 pseudovirus mCherry fluorescence expression time, (b) Inhibitory potential of Ishophloroglucin A (IPA), Diphlorethohydroxycarmalol (DPHC), Eckmaxol, and (c) fluorescence quantification. Triplicate experiments were used to evaluate the data and the mean value is expressed with \pm SD. * $p < 0.05$, ** $p < 0.01$, against spike-treated group or ## $p < 0.01$, against control (ANOVA, Duncan's multiple range test).

3.5 Inhibition of SARS-CoV-2 pseudovirus cell entry in in-vivo

The mCherry gene's expression was used to indicate successful pseudovirus entry in zebrafish larvae. The 3dpf larvae were pre-treated with polyphenolic compounds or PBS for 72h. The ACE-2 expression of the zebrafish was also evaluated using ACE-2 specific primers; forward 5'-CCCCGTAATGCAGAAGAAGA-3' and reverse 5'-TTGGTCACCTTCAGCTTGG-3'. The expression of the ACE-2 was significantly increased at 3dpf and 5dpf-7dpf, showing remarkable upregulation of ACE-2 expression (Fig. 11a). The mCherry expression was upregulated with the viral media amount that was treated to each well. However, when the embryo media: pseudovirus media ratio exceeds 10:1, it was mortal to the zebrafish and significantly downregulated the mCherry expression (Fig. 11b). Thus, 10 μ L media containing pseudovirus was treated each well. The mCherry expression results revealed that all compounds significantly and dose-dependently downregulated the pseudovirus cell entry (Fig. 11c).

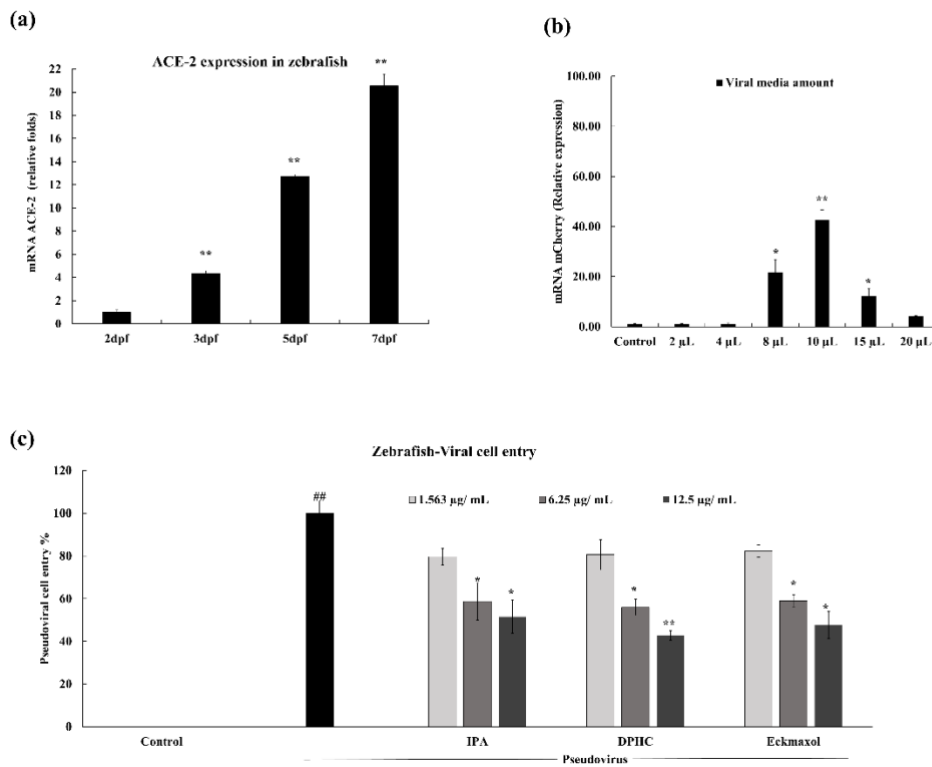


Fig. 11. In-vivo evaluation of SARS-CoV-2 pseudovirus cell entry. (a) ACE-2 expression of zebrafish with age, (b) optimization of the effect of viral media amount for mCherry expression in zebrafish, and (c) inhibitory potential of Ishophloroglucin A (IPA), Diphlorethohydroxycarmalol (DPHC), and Eckmaxol, against SARS-CoV-2 pseudovirus cell entry. Triplicate experiments were used to evaluate the data and the mean value is expressed with \pm SD. * $p < 0.05$, ** $p < 0.01$, against spike-treated group or ## $p < 0.01$, against control (ANOVA, Duncan's multiple range test).

4. Discussion

Many viruses employ numerous receptors and/or co-receptors for penetrating host cells [67]. Receptor recognition by coronavirus is the first and essential step for entering human cells. The spike protein of coronaviruses is defined as one of the biggest viral spike glycoproteins known, so it is plausible to imagine that different domains within a single spike protein could interact with various receptors rendering easier and faster virus entry. This aspect is crucial because, while it is ascertained that ACE2 is the most recognized door for the entry, on the other side to target only ACE2 could be limiting considering that recent data shows ACE2 is up-regulated in diabetes and treatment with ACE inhibitors and angiotensin II Type-I receptor blockers [68]. Therefore, an increased expression of ACE2 would be associated with a more manageable infection with SARS-CoV-2. Therefore, this aspect suggests that COVID-19 therapy by a multi-targeting approach is the right way. In this work, an in-silico approach using docking studies has been performed for the initial screening of the compounds based on the binding energy of ligands with ACE-2, 3CLpro, and PLpro.

ACE-2 is a single-pass type 1 membrane monocarboxypeptidase discovered two decades ago [69]. ACE-2 consists of an N-terminal peptidase domain and a C-terminal collecting-like domain. The peptidase domain is responsible for the main functions of the renin-angiotensin system (RAS). The ACE-2 shares 40% homology with the N-terminal catalytic domain of ACE, and a hydrophobic region near the C-terminus is likely to serve as a membrane anchor [70]. The ACE-2 protein is encoded by the ACE-2 gene located on chromosome Xp22. These ACE-2 proteins are more abundantly expressed on the apical surface of the well-differentiated and mostly ciliated airway epithelium of the lungs (alveolar Type-2 cells) and enterocytes of the small intestine [71]. Furthermore,

ACE-2 protein is expressed in arterial and venous endothelial cells and arterial smooth muscle cells in the heart, kidneys, adrenal glands, pancreas, skeletal muscle, and adipose tissues [69]. The coronavirus, SARS-CoV-2, has been seen to infect humans through their spike protein responsible for CoV cell entry and host-to-host transmission. During viral infection, this spike protein cleaves into S1 and S2 sites [70]. The FURIN cleavage site in the SARS-CoV-2S protein may provide a priming mechanism [72]. The ectodomain S1 of spike protein binds to the peptidase domain of the ACE-2 enzyme, while the S2 is cleaved further by the host cell serine protease TMPRSS2 resulting in membrane fusion. These steps are essential for viral entry into the cells [73]. An in vivo study shows that the infection of human airway epithelia by SARS coronavirus correlated with the state of cell differentiation and ACE-2 expression and localization. The infection tends to occur more readily through well-differentiated ciliated cells with higher ACE-2 expression [74]. Therefore, the present study evaluated the inhibitory activity of IPA, DPHC, and Eckmaxol on ACE-2: SARS-CoV-2 spike protein binding. IPA bound to the ACE-2 receptor protein via a conventional hydrogen bond with ARG393 residue. The bond length was 2.28°A.

Moreover, it was stabilized on ACE-2 by another pi-pi stacked bond with ALA386 (5.10°A) and two salt bridges HIS34 residue (1.78Å and 5.99°A). The molecular docking results revealed that IPA shielded ACE-2 from the RBD of the spike protein. An in-vitro assay further confirmed this result. IPA successfully inhibited the ACE-2: spike protein binding. These results suggested IPA as a potential drug candidate against SARS-CoV-2. DPHC and Eckmaxol also significantly downregulated the ACE-2: spike protein binding, expressing the potential as a SARS-CoV-2 cell entry mechanism inhibitor.

Further experiments, including pseudovirus and zebrafish in-vivo model, further solidified the in-vitro assay kit results. Studies of live SARS-CoV-2 are restricted to biosafety level 3 laboratories, which has made SARS-CoV-2 research inaccessible to the majority of research laboratories around the world, which would seriously delay the development of vaccines and therapeutics against SARS-CoV-2 if there were no alternative solution. Pseudoviruses are a kind of recombinant virus with their core or backbone and surface proteins derived from different viruses [75]. Genes inside pseudoviruses are usually altered or modified to abolish native surface protein expression. An additional plasmid is then used to express alternative surface proteins, producing a pseudovirus that can infect susceptible host cells but can only replicate intracellularly for a single round [76, 77]. As viral surface proteins play pivotal roles in gaining entry into host cells, the conformational structures of pseudoviral surface proteins have high similarity to that of the native viral proteins; however, pseudoviruses have attenuated virulence compared with wild-type (WT) viruses, allowing them to be safely handled in biosafety level 2 laboratories [78]. As a result, pseudoviruses are widely used for the study of cellular tropism [79], receptor recognition [80], drug discovery [81], and for developing and evaluating antibodies and vaccines [82, 83].

The present study utilized the human immunodeficiency virus (HIV-1)-based lentiviral packaging system for developing SARS-CoV-2 pseudovirus. The HIV-1 lentiviral packaging system is currently the most widely used SARS-CoV-2 pseudoviral packaging system. Generally, two or three plasmids are co-transfected into the cells to produce the pseudoviruses. The two-plasmid packaging system is the most widely used SARS-CoV-2 pseudoviral packaging system, which includes a plasmid to express the SARS-CoV-2 S protein and another HIV-1 backbone plasmid to express the packaging proteins and signals but with the envelope gene deleted. Several HIV-1 lentiviral backbone plasmids

are used in the two-plasmid packaging system, such as pNL4-3-kfs [84] and pNL4-3.Luc.R-E- [85-87]. The HIV-1 three-plasmid packaging system is usually comprised of a packaging plasmid, a transfer plasmid containing the reporter gene, and a SARS-CoV-2 S protein-expressing plasmid. Specifically, this system involves splitting the HIV-1 backbone into separate packaging and transfer plasmids. The packaging plasmid expresses the Gag and Pol proteins.

In contrast, the transfer plasmid contains the cis-regulatory elements needed for HIV-1 reverse transcription, integration, and packaging, as well as multiple cloning sites and a reporter gene under the control of a heterogeneous promoter [88, 89]. The SARS-CoV-2 S protein-expressing plasmid is made of a vector carrying the S gene driven by a cytomegalovirus (CMV) promoter. Several independent groups have reported co-transfection of pNL4-3.Luc.R-E- and a SARS-CoV-2 S protein-expressing plasmid can produce SARS-CoV-2 pseudoviruses [85-87].

The prepared SARS-CoV-2 pseudovirus was treated to the ACE-2 receptor overexpressed HEK293T cells and observed the significant upregulation of the mCherry expression in the cell. Further, we treated this pseudovirus to the normal HEK293T cells and did not recognize significant up-regulation of the mCherry fluorescence in the cell. After optimization of the plasmid ratio and expression time, the author confirmed the downregulation of mCherry expression in the cells via fluorescence microscopic images. ACE-2 chemical inhibitor (MLS-4760) was used to inhibit ACE-2 activity in the cells. This reversible ACE2 inhibitor binds to the active site zinc with high affinity and emulates the transition state during peptide hydrolysis. It reduces serum and kidney ACE 2 activity and abolishes angiotensin II-induced hypertension in mice [90]. DPHC showed remarkable inhibitory activity against pseudoviral cell entry among the evaluated

compounds. Meanwhile, IPA and Eckmaxol also significantly downregulated the cell entry mechanism via inhibiting spike: ACE-2 interaction.

These results were further confirmed by an in-vivo experiment. Here, we established a zebrafish model to evaluate the cell entry mechanism. Animal models have been essential tools for uncovering many human diseases' pathogenesis and therapeutic targets. They are used to demonstrate the efficacy and safety of therapeutic agents, provide essential information on routes of administration, pharmacokinetics, and pharmacodynamics, and identify critical mechanisms driving pathology in vivo. Although COVID-19 has appeared suddenly and recently, research studies have already developed and implemented many animal models for deciphering the secrets of the disease and provided insights into SARS-CoV-2 biology.

Zebrafish (*Danio rerio*) has been demonstrated as a reliable model system for studying human viral pathologies, including RNA viruses such as Chikungunya virus [91], and is considered suitable for rapid mass testing for COVID-19. However, no evidence supports that coronaviruses infect zebrafish or other fish species. This vertebrate model has unique advantages, including transparent bodies, a short lifespan, low maintenance costs, the easy production of large numbers of embryos, and numerous reporter lines available to monitor immune and inflammatory responses. Moreover, humans and zebrafish share 70% of the genome, while 84% of human genes associated with human diseases have a counterpart in zebrafish. Comparative analysis of ACE2 molecules in vertebrates indicates they are well conserved (Fig. 2). A single ortholog of mammalian ACE2 is present in zebrafish. The results of the present study revealed that all compounds significantly and dose-dependently downregulated the pseudoviral cell entry mechanism. Further, DPHC showed comparatively higher inhibitory activity than other compounds.

5. Conclusion

The results from the present study revealed the inhibitory potential of IPA, DPHC, and Eckmaxol in three ways, including in-silico, in-vitro, and in-vivo. Moreover, these results solidified the concept of a multi-target approach against SARS-CoV-2. Until part II, we confirmed that these compounds have the potential to inhibit SARS-CoV-2 cell entry by inhibiting the interaction between SARS-CoV-2 spike protein and ACE-2 receptor and SARS-CoV-2 replication and survival in the host cell by inhibiting the proteolytic activity of 3CLpro and PLpro. Based on the in-silico and in-vitro assay kit results, IPA showed higher inhibitory activity than DPHC and Eckmaxol. However, cell-based inhibitory activity evaluation and in-vivo experiment results showed that DPHC has high inhibitory activity. The reason for this can be the instability of the IPA due to its high molecular weight.

Part III: Polyphenolic Compounds Isolated from Marine Algae inhibit the SARS-CoV-2 spike protein-induced cytokine storm in the host

1. Introduction

As exposure to SARS-CoV-2 has become almost inevitable, it is essential to understand the effects of viral infection and minimize its impact. The author investigated the inhibition of SARS-CoV-2 cell entry mechanism and replication in the host cell and revealed the inhibitory potential of IPA, DPHC, Eckmaxol, and Dieckol. Most of these compounds are well-known as anti-inflammatory agents, specifically as TLR inhibitors. Therefore, the present part is expected to investigate the anti-inflammatory potential of these compounds against SARS-CoV-2 spike protein-induced inflammation. This further solidifies the multi-target approach of these polyphenolic compounds against SARS-CoV-2. Like other coronaviruses, such as SARS-CoV-1 and Middle Eastern respiratory syndrome (MERS)-CoV, SARS-CoV-2 primarily causes infection in the respiratory tract, leading to either asymptomatic infection or a range of symptoms including cough, fever, pneumonia, respiratory failure, along with other complications like diarrhea and multi-organ failures [92-94]. In the absence of effective therapies, COVID-19 has caused over 4 million deaths worldwide by the end of 2021. Although our knowledge is still evolving, immunopathology caused by the cytokine storm plays a decisive role in COVID-19 pathogenesis. SARS-CoV-2 infects human cells through its Spike (S) protein, which binds to the receptor angiotensin-converting enzyme 2 (ACE2), expressed on alveolar epithelial cells, allowing endocytosis of the viral particle[95, 96]. Following endocytosis, the viral genome is replicated using both viral and host machineries, leading to the death of virally infected cells [97]. The pathology of SARS-CoV-2 infected lung is further worsened with inflammatory responses of innate immune cells such as macrophages, monocytes, and neutrophils, which are activated by viral components and products of apoptotic and necrotic cells [98]. While the innate immune response is essential for

antiviral host defense, excessive inflammatory cytokines and chemokines are cytotoxic for respiratory epithelial cells and vascular endothelial cells [62]. Indeed, the clinical manifestation of COVID-19 is marked by higher concentrations of IL-2, IL-6, IL-8, TNF α , IFN γ , MCP1, MIP1 α , IP-10, and GM-CSF in patients' blood [98]. Disease severity and death of COVID-19 patients have been correlated to the elevated expression of IL-6 and TNF α . However, our understanding of the precise mechanism of the induction of proinflammatory cytokines and chemokines during SARS-CoV-2 infection is very limited. The innate immune inflammatory response is initiated with the recognition of pathogen-associated molecular patterns (PAMPs) by pattern recognition receptors (PRRs), such as Toll-like receptors (TLRs), NOD-like receptors (NLRs), and RIG-I like receptors (RLRs). Activated PRRs involve multiple signaling adapters to activate transcription factors, such as NF- κ B, AP1, and IRF3, which regulate the expression of genes involved in immunity and inflammation. RNA sensing receptors such as TLR7, RIG-I, and MDA5 play a central role in antiviral immunity by inducing type I interferons (IFN α and IFN β) via IRF3 and NF- κ B [99-102]. Although the relative contribution of RNA sensing pathways in SARS-CoV-2-mediated immunopathology is yet to be explored, previous studies reported that macrophages and dendritic cells infected with SARS-CoV-1 produce proinflammatory cytokines and chemokines, but not type I interferons [103, 104]. Consistently, inflammatory responses in severe COVID-19 patients are characterized by high levels of proinflammatory cytokines but poor type I interferon response [94]. Beyond these phenotypic observations, the precise mechanism of the hyper-inflammatory response during SARS-CoV-2 infection is poorly understood. Therefore, the present study investigated the anti-inflammatory potential of IPA, DPHC, Eckmaxol, and Dieckol against SARS-CoV-2 spike protein-induced inflammation in the host cell through in-vitro and in-vivo evaluations.

2. Methods and Materials

2.1 Chemicals and reagents

Dimethylsulfoxide (DMSO) and All the organic solvents (HPLC grade) used in the experiments were purchased from Sigma-Aldrich (St Louis, MO, USA). The murine MH-S lung macrophage cell line was purchased from American Type Culture Collection (Rockville, MD, USA). Roswell Park Memorial Institute medium (RPMI) supplemented with fetal bovine serum (FBS) and antibiotics (penicillin and streptomycin) were purchased from Gibco (Life Technologies, Grand Island, NY, USA). The antibodies used for Western blotting were purchased from Santa Cruz Biotechnology (Santa Cruz, CA, USA). The cytokine assay kits used for the experiment were purchased from eBioscience (San Diego, CA, USA), R&D Systems (Minneapolis, MN, USA), BD Optics (San Diego, CA, USA), and Invitrogen (Carlsbad, CA, USA). HEK293T cells were purchased from American Type Culture Collection (Rockville, MD, USA). Dulbecco's modified Eagle's medium (DMEM) was purchased from Gibco/BRL (Burlington, ON, Canada), A549 and MHS cells were purchased from Sigma-Aldrich (St Louis, MO, USA). X-tremeGENE™ HP DNA Transfection Reagent was purchased from Sigma-Aldrich (St Louis, MO, USA). SARS-CoV-2 spike protein was purchased from RayBiotech (Cat. #230-30161, Norcross, Georgia, USA). Enzyme-linked immunosorbent assay (ELISA) kits for mouse TNF- α , IL-1 β , IL-6, and prostaglandin E2 (PGE2) were obtained from R & D system (Minneapolis, MN, USA). C29 TRL-2 inhibitor was purchased from Sellekchem (Cat. #S6597, SD, Houston, USA).

2.2 Cell culture and maintenance

Murine MH-S lung macrophages were maintained in RPMI growth medium supplemented with 10% FBS and 1% antibiotics. Cells were maintained under controlled

conditions of 5% CO₂ at 37 °C. Cells were periodically sub-cultured and used for the experiments in the exponential growth phase. DMEM (high glucose) with 10% FBS (heat inactivated) and 1% penicillin/streptomycin antibiotics were used as a growth media for RAW 264.7 macrophages. Cultured cells were kept in a controlled environment at 37 °C with 5% CO₂. A549 and HEK293T cells were maintained in DMEM media supplemented with 10% FBS and 1% penicillin/streptomycin antibiotics.

2.3 Maintenance of zebrafish and larvae

Zebrafish were handled as previously described [105]. The zebrafish study was approved by The Animal Care and Use Committee of Jeju National University (Jeju Special Self-governing Province, Republic of Korea). All methods were carried out in accordance with relevant guidelines and regulations. Additionally, all the methods were carried out in accordance with the ARRIVE guidelines⁵⁰. Zebrafish were raised at 28.5°C with a 14:10 h light: dark cycle in a water-recirculating tank system (pH 7.4 and 0.03% salinity). Fertilized embryos were collected after natural spawning and cultured at 28.5 °C in E3 embryo media containing 2 mg/L methylene blue. To inhibit melanin formation, 0.003% PTU was added to the egg water throughout the experimental period.

2.4 Gene transfection to the A549 and HEK293T cells

A549 and HEK293T cells were co-transfected with GFP-Flag SARS-CoV-2 spike protein plasmid using X-tremeGENE™ HP DNA Transfection Reagent according to the instruction from the manufacturer. The transfection and expression were confirmed by observing GFP under a fluorescence microscope and western blot analysis. 48h post-transfection, cell culture media was collected for Enzyme-Linked Immunosorbent Assay

(ELISA), cells were lysed with RIPA lysis buffer and protein was extracted for western blot evaluation.

2.5 Determination of Cell Viability

MTT assay was utilized to evaluate the toxicity of polyphenolic compounds (IPA, DPHC, Eckmaxol, and Dieckol) in different concentrations (1.563-150 $\mu\text{g}/\text{mL}$). The toxicity of spike protein was also evaluated (10-2000 ng/mL).

2.6 Evaluation of the Production of Cytokines

The ELISA kits were used with the manufacturer's instructions to evaluate the cytokine production (IL-1 β , IL-6, and TNF- α). In the evaluation of the inhibitory effect of the polyphenolic compounds, cells were seeded in the 12-well culture plate. Samples were treated after 24h incubation at 37 °C and 5% CO₂, and spike protein was treated after 1h from the sample treatment. Then cell culture supernatant was harvested after 8h from macrophages, and 24h from epithelial cells, and an ELISA assay was performed.

2.7 Gene expression analysis

Cells were seeded in the 12-well culture plate, and samples were treated after 24h incubation at 37 °C and 5% CO₂, and spike protein was treated after 1h incubation from the sample treatment. Then the total RNA extraction was performed using TRIzol reagent (Life Technologies, Carlsbad, CA, USA) after 8h with macrophages and 24h with epithelial cells. The total amount of RNA (1 μg) was reverse-transcribed using a first-strand cDNA synthesis kit (TaKaRa, Shiga, Japan) to obtain cDNA according to the manufacturer's instructions. For the total RNA extraction of zebrafish, the larvae from each treatment group were pooled and washed with Milli-Q water for 6 \times 20 min with

gentle agitation prior to RNA extraction. The cDNA was amplified using the primers listed in Table 1.

Table 1. Primer sequences used in the study.

Gene	Primer	Sequence
m_GAPDH	Sense	5'-AAGGGTCATCATCTCTGCCC-3'
	Antisense	5'-GTGATGGCATGGACTGTGGT-3'
m_TNF- α	Sense	5'-TTGACCTCAGCGCTGAGTTG-3'
	Antisense	5'-CCTGTAGCCCACGTCGTAGC-3'
m_IL-6	Sense	5'-GTACTCCAGAAGACCAGAGG-3'
	Antisense	5'-TGCTGGTGACAACCACGGCC-3'
m_IL-1 β	Sense	5'-CAGGATGAGGACATGAGCACC-3'
	Antisense	5'-CTCTGCAGACTCAAACCTCCAC-3'
m_CXCL-1	Sense	5'-TGAGCTGCGCTGTCAGTGCCT-3'
	Antisense	5'-AGAAGCCAGCGTTCACCAGA-3'
m_CXCL-2	Sense	5'-CAAGAACATCCAGAGCTTGAGTGT-3'

	Antisense	5'-GCCCTTGAGAGTGGCTATGACTT-3'
	Sense	5'-CCCAGGGA CCTCTCT CTAATCA-3'
h_TNF- α	Antisense	5'-GCTTGAGGGTTTGCTACAACATG-3'
	Sense	5'-GTAGCCGCCCCACACAGA-3'
h_IL-6	Antisense	5'-CATGTCTCCTTTCTCAGGGCTG-3'
	Sense	5'-AAATACCTGTGGCCTTGGGC-3'
h_IL-1 β	Antisense	5'-TTTGGGATCTACACTCTCCAGCT-3'
	Sense	5'-AACCGAAGTCATAGCCACAC-3'
h_CXCL-1	Antisense	5'-CCTCCCTTCTGGTCAGTT-3'
	Sense	5'-CGCCCAAACCGAAGTCAT-3'
h_CXCL-2	Antisense	5'-GATTTGCCATTTTTTCAGCATCTTT-3'
	Sense	5'-TGGTATTGTGATGGACTCTGG-3'
z_ β -actin	Antisense	5'-AGCACTGTGTTGGCATAACAGG-3'

	Sense	5'-CTGGCTCCTGCTTTTGGC-3'
z_ace2	Antisense	5'-TCTTTATCTGCATTTTCCTGGGAG-3'
	Sense	5'-CTGCTTCACGCTCCATAAGA-3'
z_TNF- α	Antisense	5'-CTGGTCCTGGTCATCTCTCC-3'
	Sense	5'-ATGCCATCCGCTCAGAGT-3'
z_IL-6	Antisense	5'-GCGTCAGGTTTACTCACTT-3'
	Sense	5'-CGTCTCCACATCTCGTACTCA-3'
z_IL-1 β	Antisense	5'-GTGTCTTTTCCTGTCCATCTCC-3'
	Sense	5'-TGATGGTGCTGACAATCGTG-3'
z_CCL20	Antisense	5'-CTTTGGACGGGTCTGTGCA-3'

h-Human, m- Mouse, z-Zebrafish

2.8 Western blot evaluation

A549 and MHS cells were seeded in 1×10^5 cells/ mL and incubated for 24h. Then samples were treated and provided one h incubation before treating spike protein. MHS and A549 cells were harvested after 8 h and 24h, respectively. The harvested cells were washed with ice-cold PBS, and cytosolic proteins were extracted. According to the

previously established method, NF- κ B and MAPK, cell signaling pathways, were analyzed to evaluate the anti-inflammatory potential [106].

2.9 Spike protein microinjection to zebrafish

Three dpf zebrafish larvae were anesthetized using 0.04% tricaine, and SARS-CoV-2 spike protein (1 mg/ mL, 2 nL in each larva) was microinjected into the yolk sac using Drummond NANOJECT III Injector (Drummond Scientific, Broomall, PA, USA). The negative control group was microinjected with PBS. After the microinjection of spike protein, the larvae were immediately placed in E3 media containing the indicated concentrations of IPA, DPHC, Eckmaxol, and Dieckol. Dead larvae were removed within 0.5 hpi. Each group of larvae (n = 50) was cultured at 28.5 °C and observed for signs of phenotypic abnormality and mortality. The heart rate of the larvae was manually counted for one minute and used as an indicator for the cardiac toxicity evaluations. All mentioned parameters were observed using Olympus SZ2-ILST Stereomicroscopy (Tokyo, Japan).

2.10 Neutral red staining

Neutral red is a vital dye that accumulates in the lysosomes through endocytosis. As macrophage cells undergo efficient endocytosis, neutral red more robustly labels macrophages than any other cell type. Optimal staining of macrophages in live embryos was achieved by incubating embryos in 2.5 μ g/mL neutral red solution containing 0.003% PTU at 28.5°C in the dark for 6–8 h. After staining, macrophage migration was observed using Olympus SZ2-ILST Stereomicroscopy [107].

2.11 Sudan black staining

Sudan black is an azo stain that detects the presence of lipids, with dark stains representing neutrophils. A stock solution of Sudan black was prepared from Sudan black

powder (0.6 g) dissolved in pure ethanol (200 mL). A buffer solution was made from phenol (16 g) dissolved in pure ethanol (30 mL) plus $\text{Na}_2\text{HPO}_4 \cdot 12\text{H}_2\text{O}$ (0.3 g) dissolved in distilled water (100 mL). Mixing stock solution (30 mL) with buffer (20 mL) was a working staining solution. Whole larvae were fixed with 4% methanol-free PFA in PBS for 2 h at room temperature and rinsed in PBS. The larvae were incubated in Sudan black solution for 40 min, washed extensively in 70% ethanol, and then progressively rehydrated with PBS plus 0.1% Tween-20. The stained neutrophils were observed using Olympus SZ2-ILST stereomicroscope [107].

2.12 Statistical analysis

All experiment results were expressed as the mean value with the standard deviation of three independent recurrences. The significant differences of all statistical data were analysed via one-way analysis of variance according to Duncan's multiple range test using the SPSS v. 20 (IBM Corp., Armonk, NY, USA).

3. Results

3.1 Pro-inflammatory cytokine production in SARS-CoV-2 spike protein transfected A549 and HEK293T cells

The author transfected the spike protein to understand the inflammatory induction mechanism of SARS-CoV-2 spike protein to A549 and HEK293T cells and evaluated the pro-inflammatory cytokine production. The transfection was confirmed by observing GFP under the fluorescence microscope (Fig. 1a). Then, spike protein expression was confirmed by western blot (Fig. 1b).

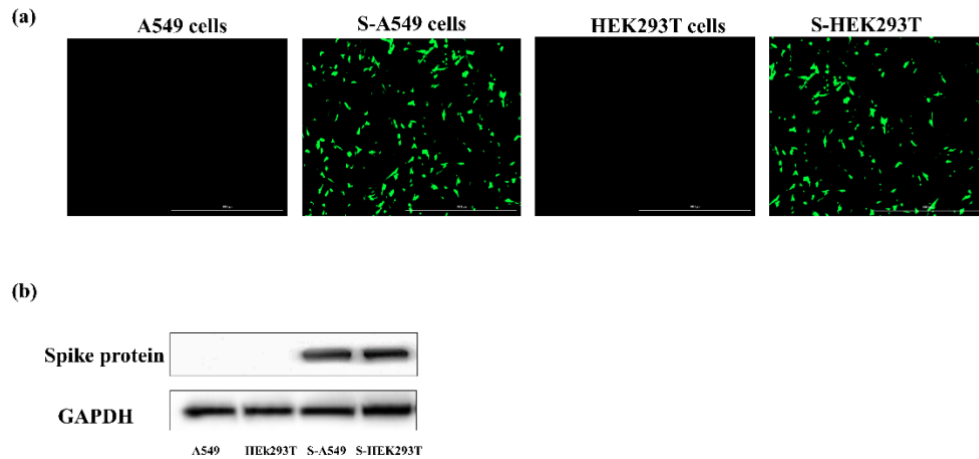


Fig. 1. Confirmation of the SARS-CoV-2 spike protein transfection. (a) GFP expression in SARS-CoV-2 spike protein transfected A549 (S-A549) and HEK293T (S-HEK293T) cells, (b) Western blot evaluation of SARS-CoV-2 spike protein in A549 and HEK293T cells.

According to the ELISA results, the cytosolic spike protein expression did not induce pro-inflammatory cytokine production (TNF- α , IL-6, and IL-1 β) in the epithelial cells (Fig.2a and b). Then to understand whether SARS-CoV-2 spike protein-infected epithelial cells can induce macrophages, we treated the MHS and RAW264.7 macrophages with SARS-CoV-2 spike protein-transfected A549 (S-A549) cell media and SARS-CoV-2 spike protein transfected HEK-293T (S-HEK-293T) cell media respectively. Based on the ELISA results of the cytokine production in macrophages, cell culture media of S-A549 and S-HEK293T did not induce the TNF- α , IL-6, and IL-1 β cytokines in the macrophages (Fig. 2c and d). These results confirmed that epithelial cells containing cytosolic spike protein did not secrete any molecules to the cell culture media that could induce macrophages.

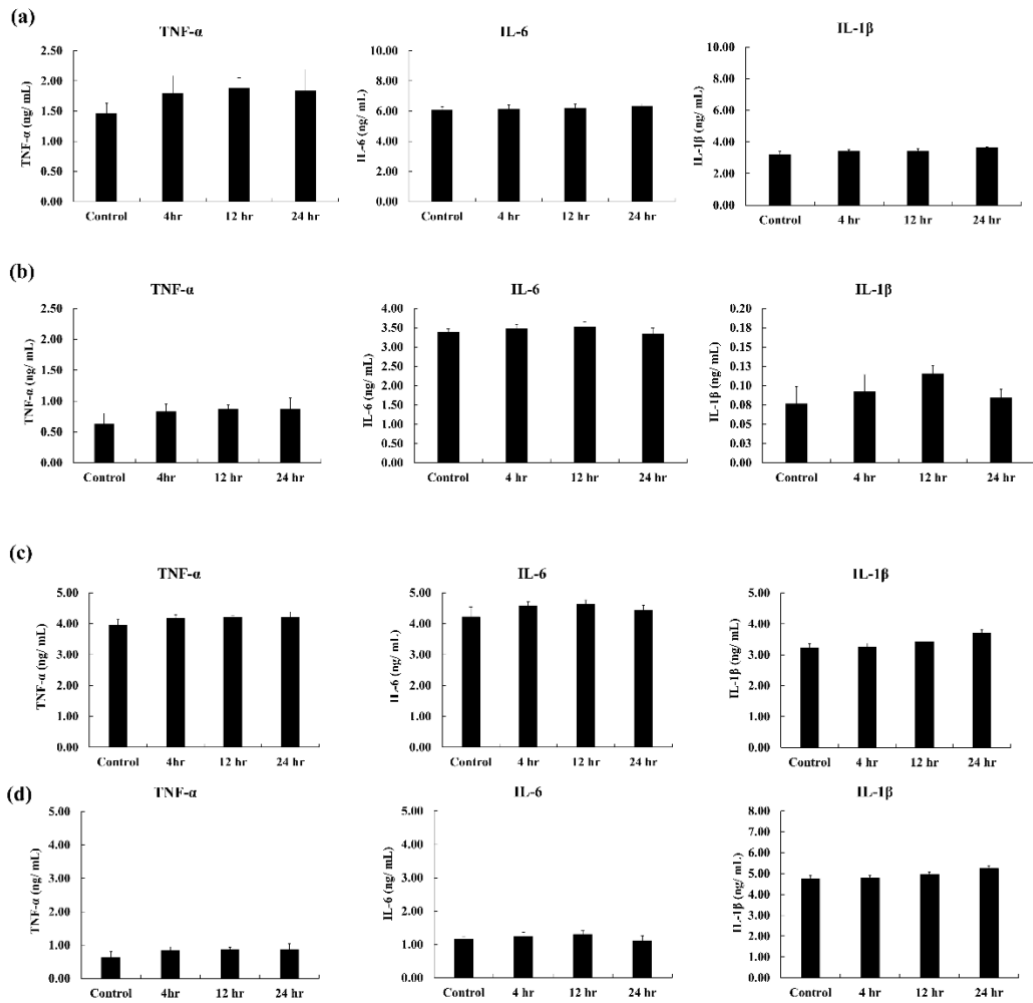


Fig. 2. Evaluation of inflammatory cytokine production in SARS-CoV-2 spike protein transfected A549 (S-A549) and HEK293T (S-HEK293T) cell. (a) inflammatory cytokine production in S-A549 cells, (c) inflammatory cytokine production in S-HEK-293T cells, (c) inflammatory cytokine production in S-A549 cell media-induced MHS cells, and (d) inflammatory cytokine production in S-HEK293T cell media-induced RAW 264.7 cells.

3.2 Pro-inflammatory cytokine production in SARS-CoV-2 spike protein transfected A549 and HEK293T cells

The cytotoxic effect of SARS-CoV-2 spike protein on A549, MHS, HEK293T, and HEK293 cells were evaluated by MTT assay (Fig 3), and based on these results, 10-1000 ng/mL and 10-500 ng/mL spike protein concentration were selected for epithelial cells and macrophages respectively. SARS-CoV-2 spike protein-treated A549 epithelial cells significantly induced the pro-inflammatory cytokine gene expression (TNF- α , IL-6, and IL-1 β) with 500 and 1000 ng/mL spike protein concentrations. Further, the author evaluated the cytokine gene expression at two time points (4h and 24h) after treating and A549 cells significant up-regulation of cytokine gene expression after 24h (Fig. 4a). Therefore, to understand the time dependant stimulation of A549 cells, the author evaluated the cytokine gene expression at four-time points (3h, 8h, 12h, and 24h) and revealed that 12h and 24h showed significant up-regulation of cytokine gene expression in A549 cells (Fig.4b). Moreover, the author evaluated the chemokine gene expression in the SARS-CoV-2 spike protein-induced A549 cells and results showed significant up-regulation of CXCL-1 and CXCL-2 (Fig. 4c).

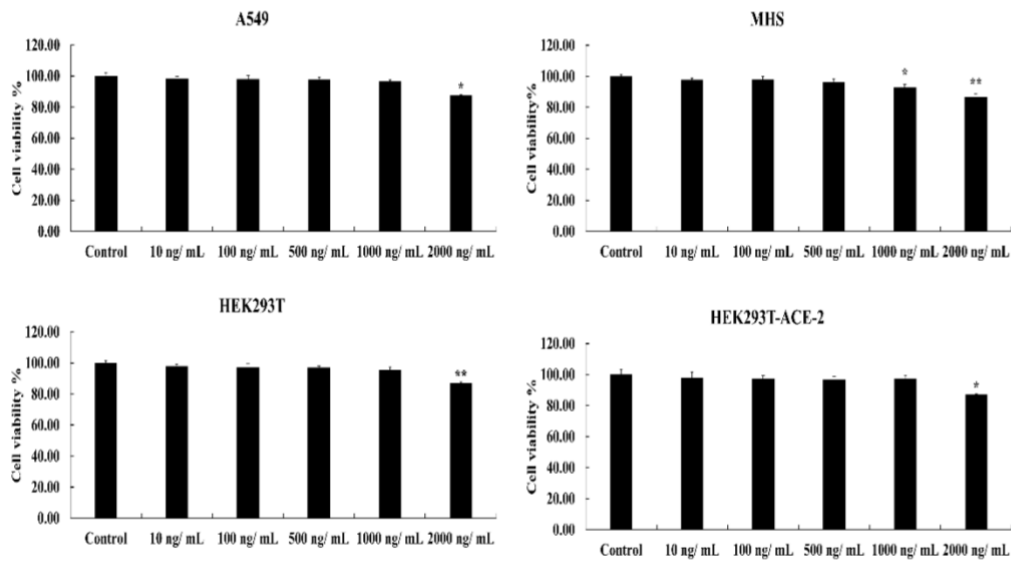


Fig. 3. Evaluation of SARS-CoV-2 spike protein-induced cytotoxicity in A549, MHS, HEK293T, and ACE-2 over-expressed HEK293T (HEK293T-ACE-2). Triplicate experiments were used to evaluate the data, and the mean value is expressed with \pm SD. * $p < 0.05$, ** $p < 0.01$, against spike-treated group or ## $p < 0.01$, against control (ANOVA, Duncan's multiple-range test)

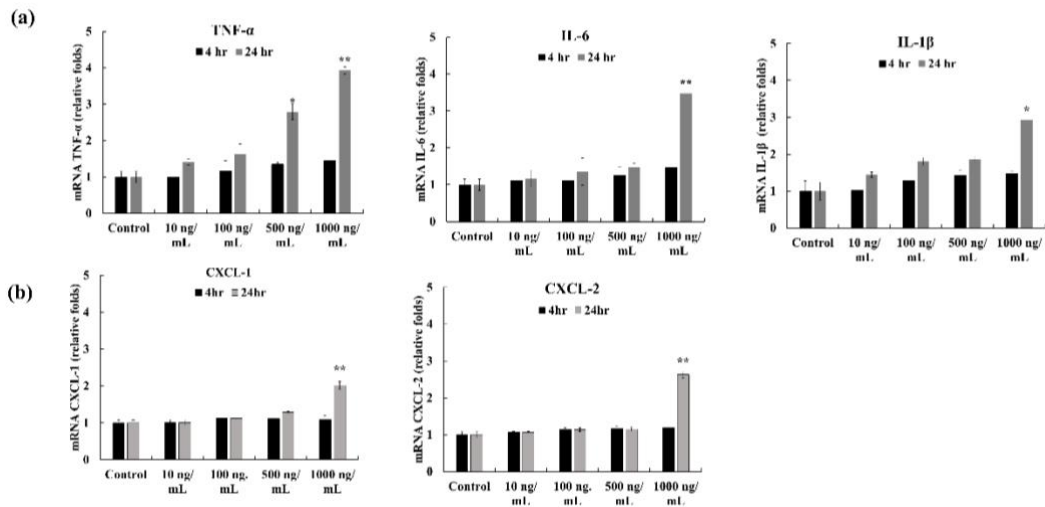


Fig. 4. Evaluation of SARS-CoV-2 spike protein-induced pro-inflammatory cytokine and chemokine gene expression in A549 cells. (a) SARS-CoV-2 spike protein-induced inflammatory cytokine gene expression from different spike protein concentrations at 4hr and 24hr in A549 cells, (b) SARS-CoV-2 spike protein-induced inflammatory chemokine gene expression from different spike protein concentrations at 4hr and 24hr in A549 cells. Triplicate experiments were used to evaluate the data, and the mean value is expressed with \pm SD. * $p < 0.05$, ** $p < 0.01$, against spike-treated group or ## $p < 0.01$, against control (ANOVA, Duncan's multiple-range test).

MHS macrophage cells were induced using 10-500 ng/ mL spike protein concentrations. ELISA results revealed that 50 ng/ mL spike protein concentration significantly up-regulated the cell's TNF- α , IL-6, and IL-1 β gene expression. Further, the author evaluated the cytokine production at two-time points (1h and 8h) after treating A549 cells with significant up-regulation of cytokine gene expression after 8h (Fig. 5a). Therefore, to understand the time dependant stimulation of MHS cells, the author evaluated the cytokine gene expression at four-time points (1h, 2h, 4h, and 8h) and revealed that 4h and 8h showed significant up-regulation of cytokine gene expression in MHS cells (Fig.5b). Moreover, the author evaluated the chemokine gene expression in the SARS-CoV-2 spike protein-induced MHS cells and results showed significant up-regulation of CXCL-1 and CXCL-2 expression levels (Fig. 5c).

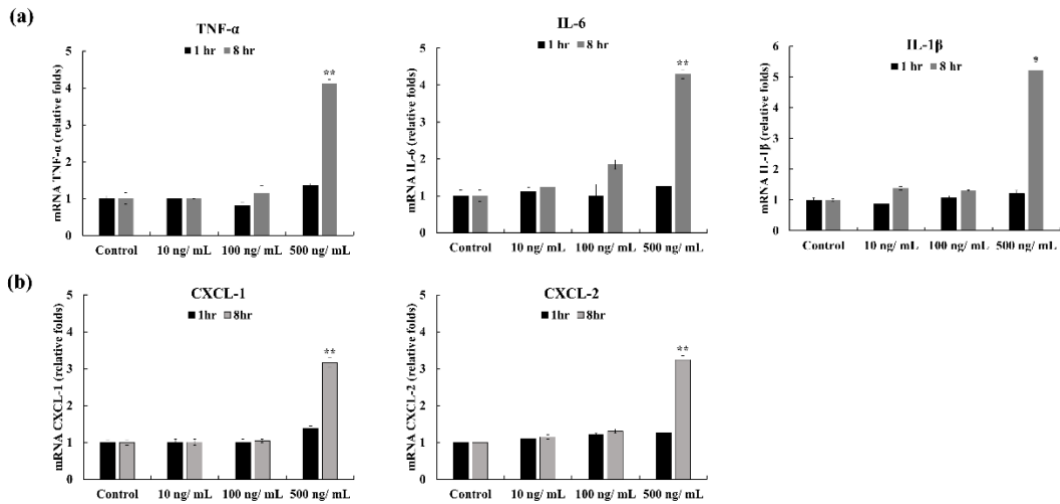


Fig. 5. Evaluation of SARS-CoV-2 spike protein-induced pro-inflammatory cytokine and chemokine gene expression in MHS cells. (a) SARS-CoV-2 spike protein-induced inflammatory cytokine gene expression from different spike protein concentrations at 4hr and 24hr in MHS cells, (b) SARS-CoV-2 spike protein-induced inflammatory chemokine gene expression from different spike protein concentrations at 4hr and 24hr in MHS cells. Triplicate experiments were used to evaluate the data, and the mean value is expressed with \pm SD. * $p < 0.05$, ** $p < 0.01$, against spike-treated group or ## $p < 0.01$, against control (ANOVA, Duncan's multiple-range test).

3.3 Evaluation of SARS-CoV-2 spike protein-induced protein expression of NF- κ B and MAPK signalling pathways

SARS-CoV-2 spike protein (1000 ng/ mL) was treated and evaluated for the protein expression of NF- κ B and MAPK signaling pathways in A549. Cell lysates collected at various time points following stimulation were analyzed for the activation of these inflammatory pathways by Western blotting. As shown in Fig. 6, I κ B α , P50, and P65 were phosphorylated in cells treated with spike protein. MAPK pathways, including ERK, P38, and JNK, are often activated concomitantly to the NF- κ B pathway in A549 cells. Surprisingly, ERK and JNK were not activated, and p38 in spike protein stimulated A549 stimulated cells. To further confirm this, the author stimulated the MHS cells from spike protein (500 ng/ mL) and evaluated the NF- κ B and MAPK pathways. The protein expression of these signaling pathways in MHS cells followed a similar pattern in A549 and activated the NF- κ B signaling pathway only. Further, the author evaluated the time-dependent expression of these proteins, and the results revealed that phosphorylation of p50, p65, and I κ B α significantly upregulated at 12h, 8h, and 8h, respectively, in A549 cells. Further, phosphorylation of all these proteins significantly upregulated at 24h in A549 cells. The phosphorylation of these proteins was comparatively earlier than in A549 cells. According to the western blot results, I κ B α , p50, and p65 significantly upregulated at 4h, 6h, and 6h, respectively, in spike protein-induced MHS cells (Fig 7). Further, phosphorylation of all proteins was significantly upregulated in 8h after the spike protein treatment.

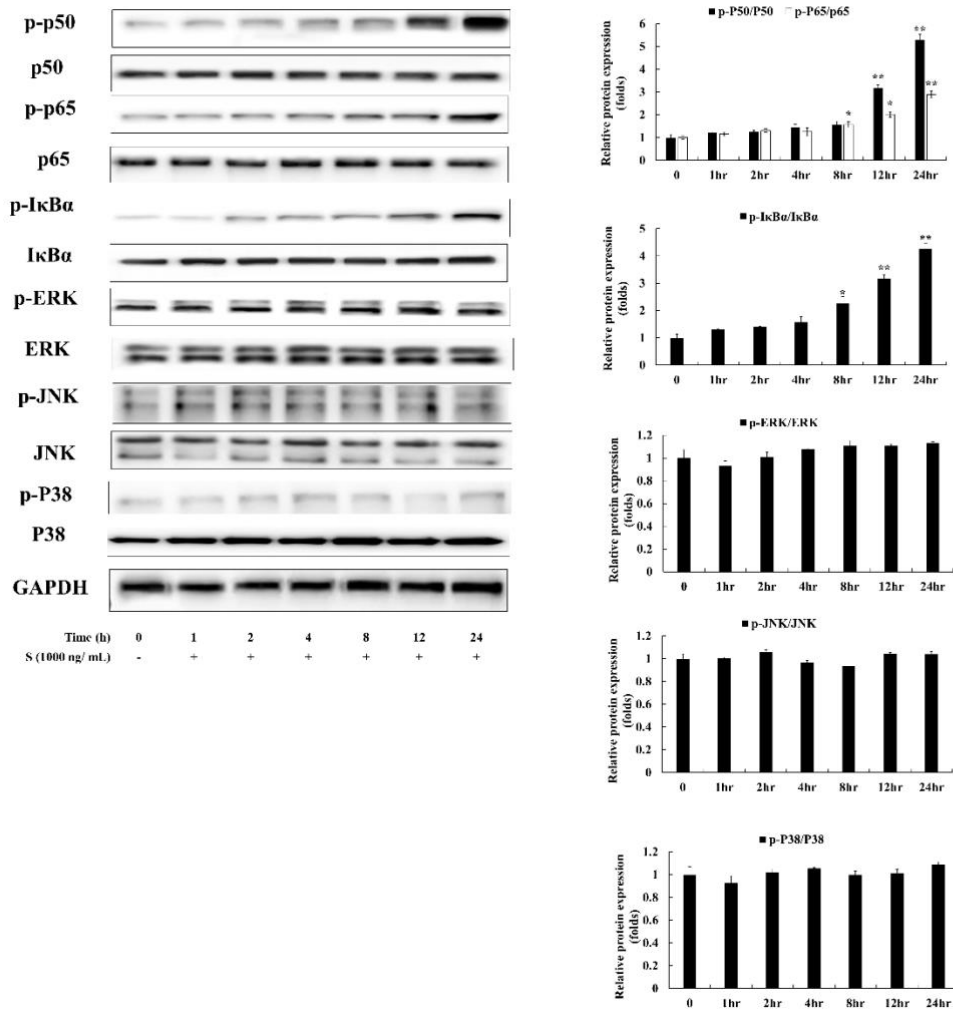


Fig. 6. Evaluation of SARS-CoV-2 spike protein-induced protein expression in NF- κ B and MAPK signalling pathways at different time points in A549 cells. Triplicate experiments were used to evaluate the data, and the mean value is expressed with \pm SD. * $p < 0.05$, ** $p < 0.01$, against spike-treated group or ## $p < 0.01$, against control (ANOVA, Duncan's multiple-range test).

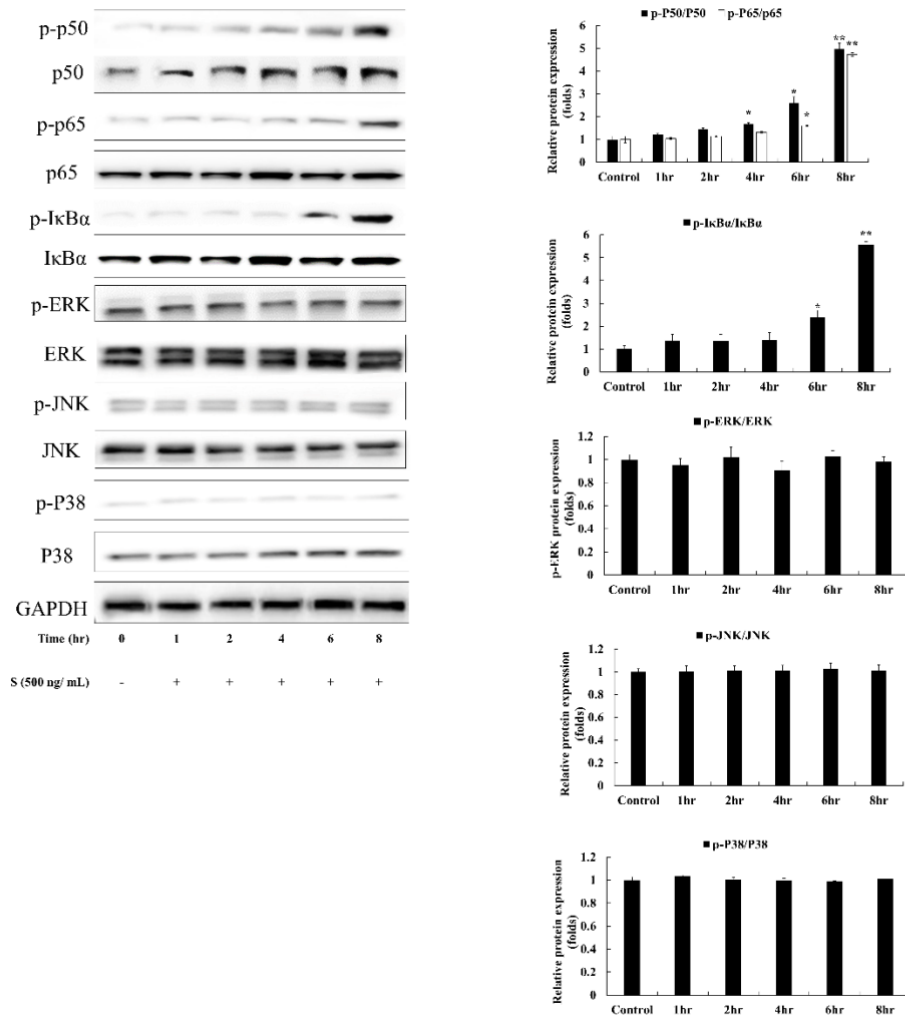


Fig. 7. Evaluation of SARS-CoV-2 spike protein-induced protein expression in NF-κB and MAPK signalling pathways at different time points in MHS cells. Triplicate experiments were used to evaluate the data, and the mean value is expressed with \pm SD. * $p < 0.05$, ** $p < 0.01$, against spike-treated group or ## $p < 0.01$, against control (ANOVA, Duncan's multiple-range test).

3.4 Evaluation of the effect of SARS-CoV-2 spike protein structure and ACE-2 expression in host cell to stimulatory potential of spike protein to develop inflammatory cytokines

ACE-2 receptor act as a cellular doorway to SARS-CoV-2 by identifying spike protein. Therefore, SARS-CoV-2 can enter the cell and initiate replication. To understand whether ACE-2 expression level on the cell surface regulates the inflammatory potential of spike protein or not, the author treated 1000 ng/ mL of spike protein to HEK293T and HEK293T-ACE-2 cells and evaluated the gene expression of TNF- α , IL-6, and IL-1 β . Results of qPCR revealed that ACE-2 expression on the cell surface did not affect the gene expression of each cytokine and confirmed that spike protein induced the inflammatory gene expression of the host cell independently from the ACE-2 receptor (Fig.8a). Further, the author heat inactivated the spike protein by heating at 95 °C for 30 min and treated the same concentration to the A549 cells. The gene expression of TNF- α , IL-6, and IL-1 β was not significantly up-regulated in heat-inactivated spike (HI-spike) protein. In contrast, normal spike protein significantly increased the gene expression of each cytokine (Fig. 8b).

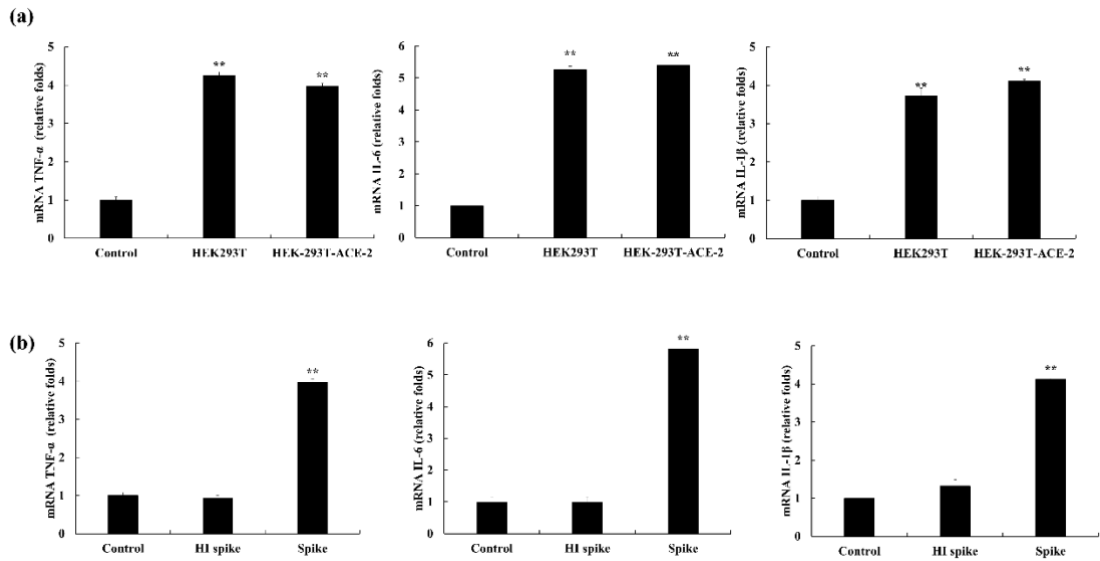


Fig. 8. Evaluation of the effect of SARS-CoV-2 spike protein structure and ACE-2 expression in host cell to stimulatory potential of spike protein to develop inflammatory cytokines. (a) SARS-CoV-2 spike protein-induced inflammatory cytokine production HEK-293T and ACE-2 over-expressed HEK293T (HEK293T-ACE-2) and (b) inflammatory cytokine production in A549 cells induced by heat-inactivated spike protein (HI spike) and spike protein. Triplicate experiments were used to evaluate the data, and the mean value is expressed with \pm SD. * $p < 0.05$, ** $p < 0.01$, against spike-treated group or ### $p < 0.01$, against control (ANOVA, Duncan's multiple-range test).

3.5 Polyphenolic compounds inhibited the inflammatory cytokine production in the SARS-CoV-2 spike protein-induced A549 and MHS cells

The cytotoxicity of IPA, DPHC, Eckmaxol, and Dieckol was evaluated to determine the safe dose range to evaluate the anti-inflammatory potential. Based on the results, 1.563, 6.25, and 125. µg/ mL was selected to evaluate the anti-inflammatory activity of each compound against SARS-CoV-2-induced inflammation (Fig. 9).

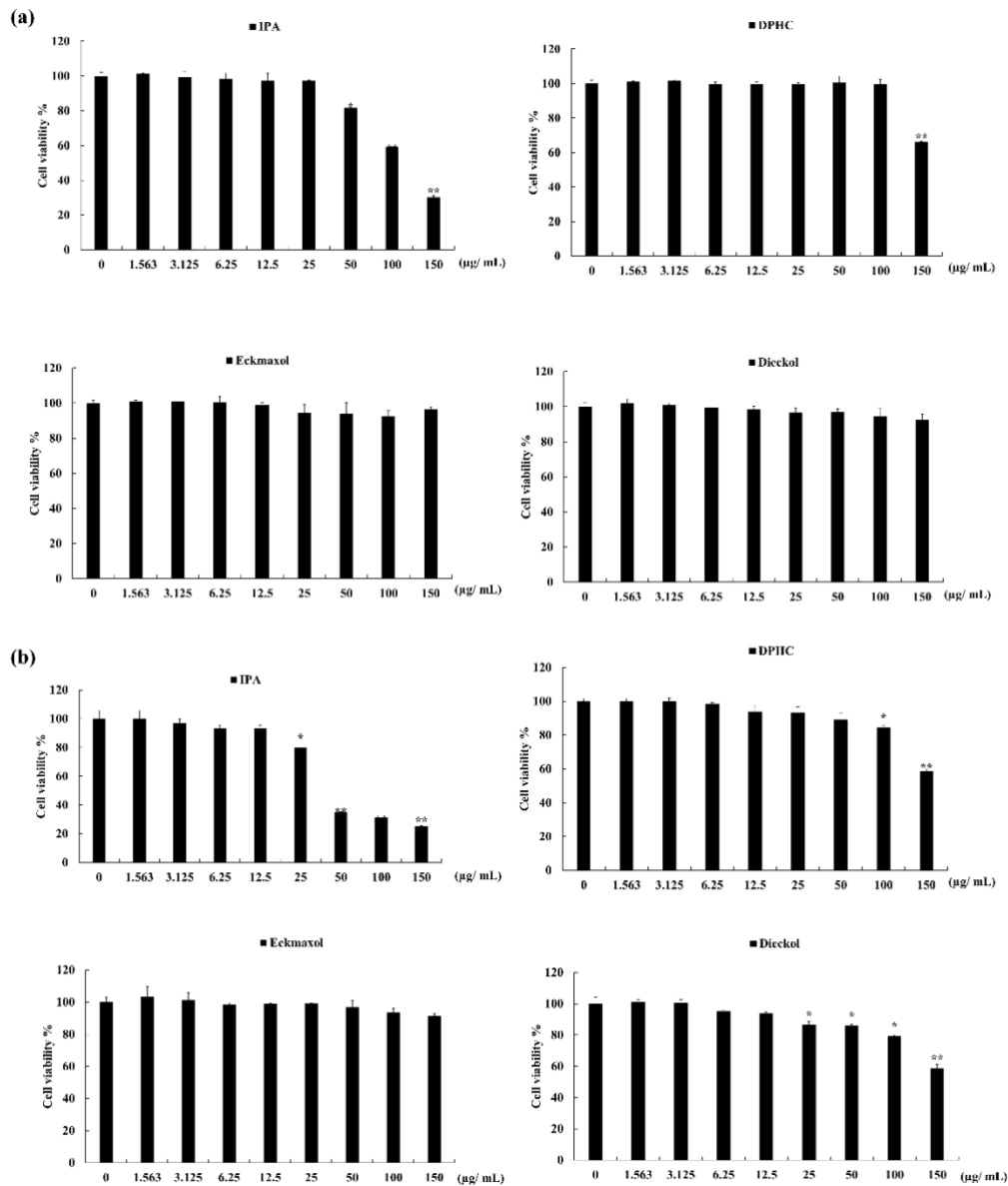


Fig 9. Cytotoxicity evaluation of (a) Ishophloroglucin A (IPA), Diphlorethohydroxycarmalol (DPHC), Eckmaxol and Dieckol in A549 cells and (b) MHS cells. Triplicate experiments were used to evaluate the data, and the mean value is expressed with \pm SD. * $p < 0.05$, ** $p < 0.01$, against spike-treated group or ## $p < 0.01$, against control (ANOVA, Duncan's multiple-range test).

3.6 Polyphenolic compounds inhibited the inflammatory cytokine and chemokine gene expression in the SARS-CoV-2 spike protein-induced A549 and MHS cells

The qPCR results of TNF- α , IL-6, and IL-1 β in A549 cells revealed the significant up-regulation of gene expression, and it was significantly reduced by TLR-2 inhibitor (150 μ M). Further, the treatments of IPA, DPHC, Eckmaxol, and Dieckol significantly and dose-dependently declined these up-regulated gene expressions (Fig.10a). Moreover, the author evaluated the spike protein-induced chemokine gene expression. It was also significantly down-regulated by the TLR-2 inhibitor and significantly and dose-dependently reduced by IPA, DPHC, Eckmaxol, and Dieckol treatments (Fig 10b). MHS cells significantly up-regulated its inflammatory cytokine and chemokine gene expression with SARS-CoV-2 spike protein treatment and TLR-2 inhibitor (150 μ M). and IPA, DPHC, Eckmaxol, and Dieckol significantly decreased the gene expression of TNF- α , IL-6, and IL-1 β (Fig. 10c), CXCL-1 and CXCL-2 (Fig. 10d).

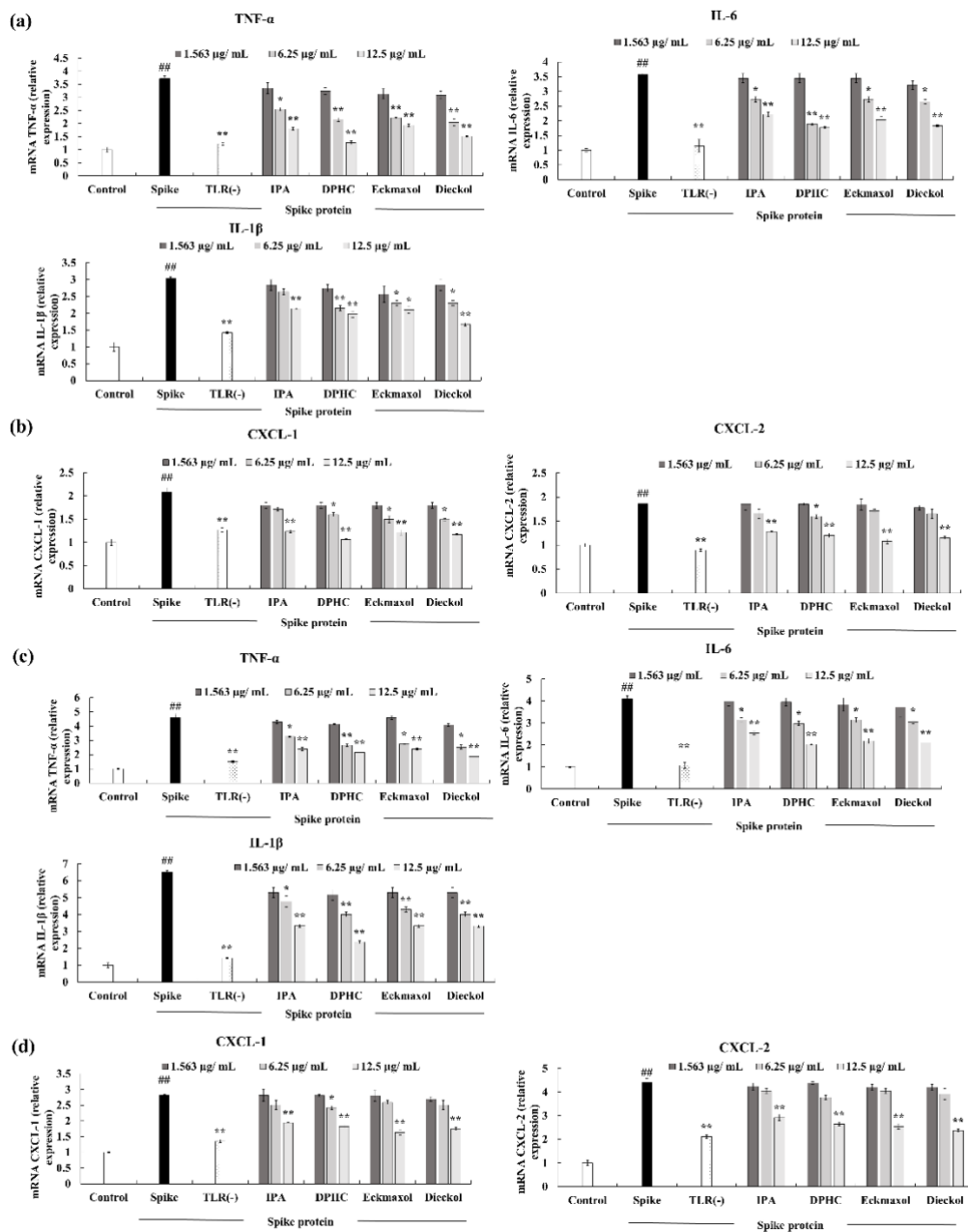


Fig 10. Inhibitory effect of Ishophloroglucin A (IPA), Diphlorethohydroxycarmalol (DPHC), Eckmaxol and Dieckol on (a) SARS-CoV-2 spike protein-induced inflammatory cytokine and (b) chemokine gene expression in A549 cells, (c) SARS-CoV-2 spike protein-induced inflammatory cytokine and (d) chemokine gene expression in MHS cells. Triplicate experiments were used to evaluate the data, and the mean value is expressed with \pm SD. * $p < 0.05$, ** $p < 0.01$, against spike-treated group or ## $p < 0.01$, against control (ANOVA, Duncan's multiple-range test).

3.7 Polyphenolic compounds inhibited the inflammatory cytokine and chemokine protein expression in the SARS-CoV-2 spike protein-induced A549 and MHS cells

The SARS-CoV-2 spike protein treatment in A549 cells significantly upregulated the phosphorylation of proteins in the NF- κ B signaling pathway. We evaluated the phosphorylation of MyD88, I κ B α , p50, and p65 in A549 cells. The upregulation of the phosphorylation of these proteins was significantly down-regulated by the TLR-2 inhibitor (150 μ M) treatment. Moreover, IPA, DPHC, Eckmaxol, and Dieckol also significantly and dose-dependently down-regulated the phosphorylation of these proteins (Fig. 11). To further solidification of these results, the author performed the same experiment with MHS cells, and results revealed that SARS-COV-2 spike protein induced-MHS cells also showed upregulated phosphorylation of NF- κ B signaling pathway. In contrast, TLR-2 inhibitor and polyphenolic compounds significantly and dose-dependently down-regulated the phosphorylation of the NF- κ B signaling pathway (Fig. 12).

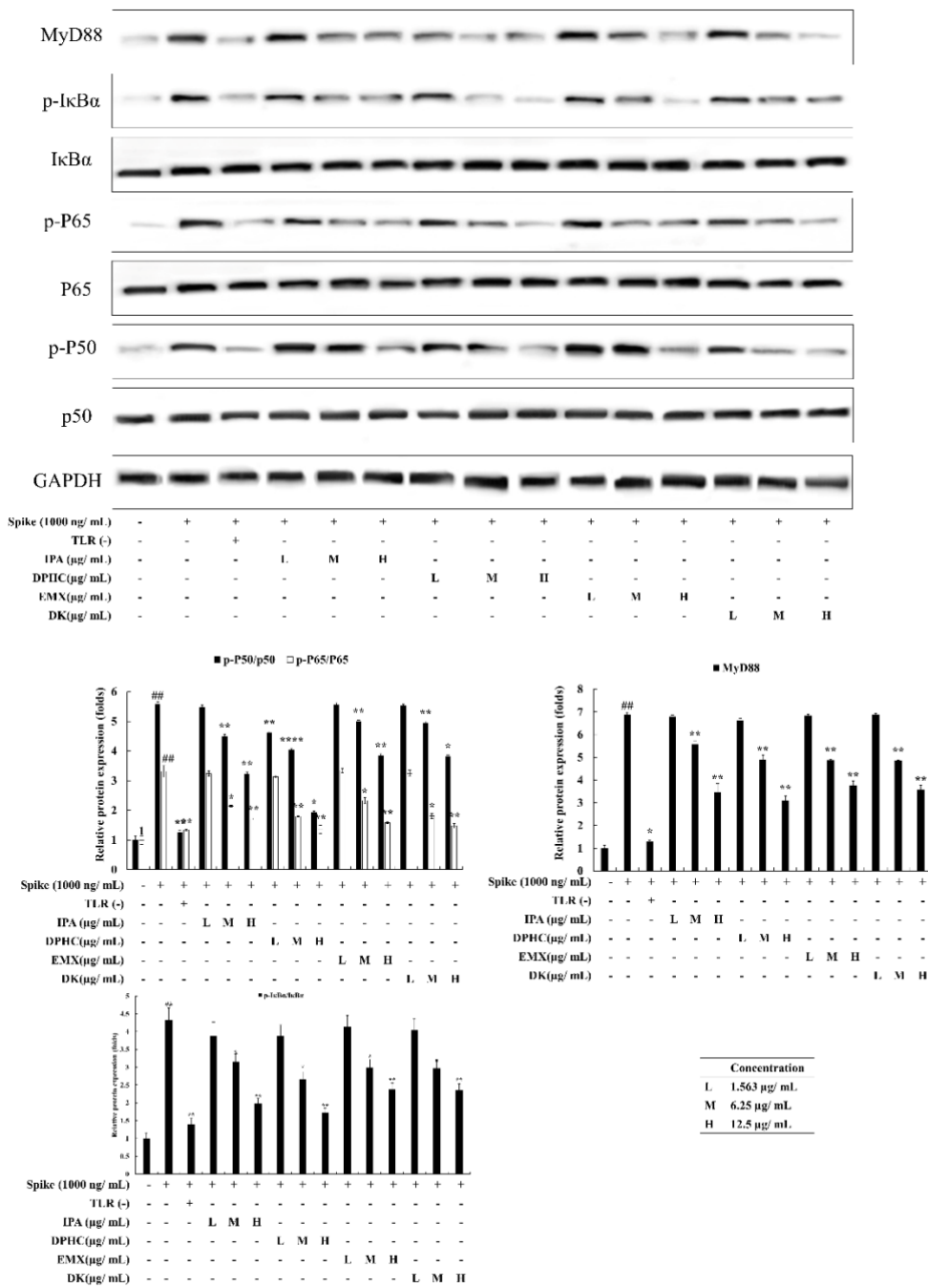


Fig 11. Evaluation of the inhibitory potential of Ishophloroglucin A (IPA), Diploretrohydroxycarmalol (DPHC), Eckmaxol, and Dieckol against protein expression SARS-CoV-2 spike protein-induced NF-κB signalling pathway in A549 cells. Triplicate experiments were used to evaluate the data and the mean value is expressed with \pm SD. * $p < 0.05$, ** $p < 0.01$, against spike-treated group or ## $p < 0.01$, against control (ANOVA, Duncan's multiple range test).

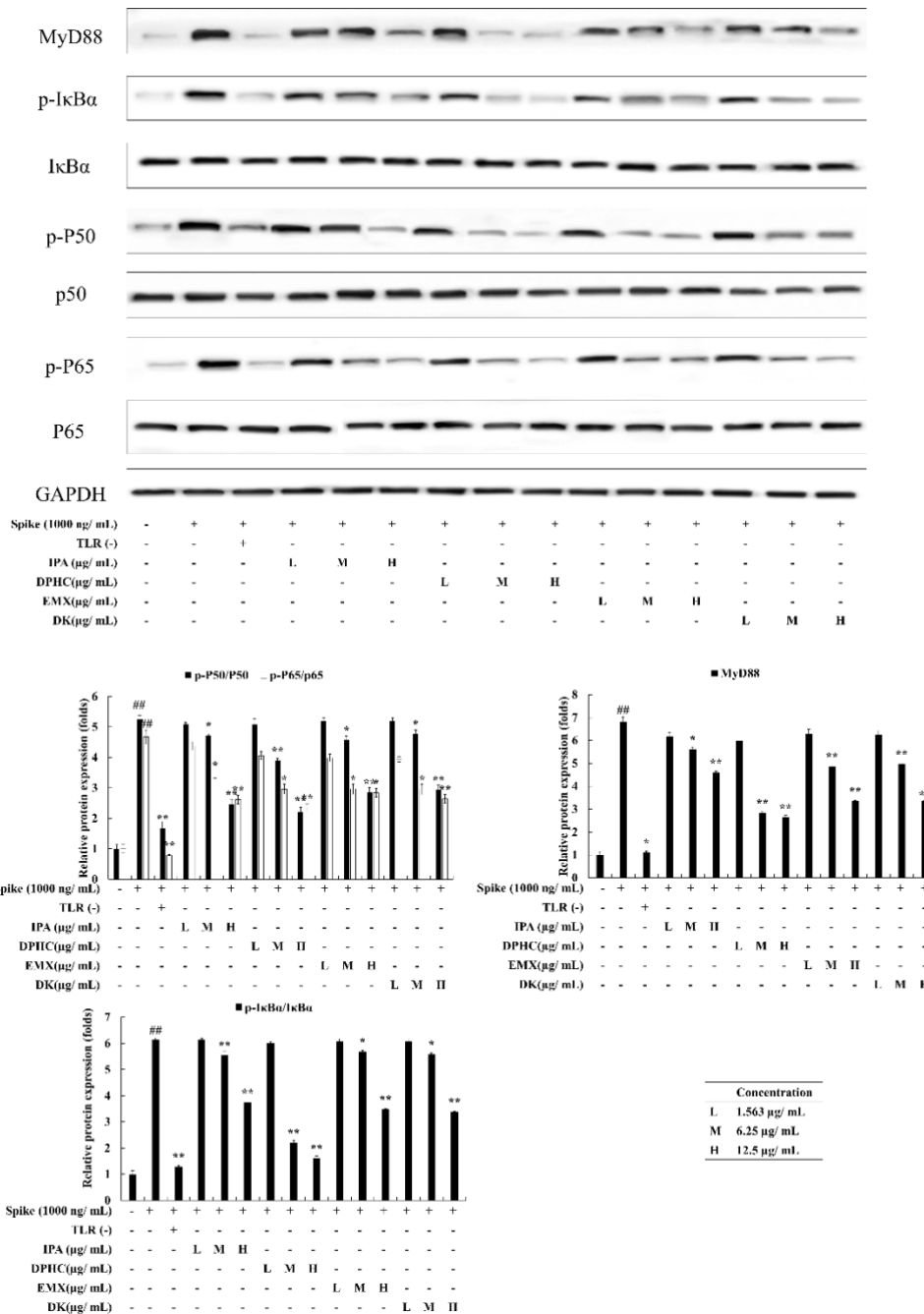


Fig 12. Evaluation of the inhibitory potential of Ishophloroglucin A (IPA), Diphlorethohydroxycarmalol (DPHC), Eckmaxol, and Dieckol against protein expression SARS-CoV-2 spike protein-induced NF-κB signalling pathway in MHS cells. Triplicate experiments were used to evaluate the data and the mean value is expressed with \pm SD. * $p < 0.05$, ** $p < 0.01$, against spike-treated group or ## $p < 0.01$, against control (ANOVA, Duncan's multiple range test).

3.8 In-vivo evaluation of the anti-inflammatory potential of polyphenolic compounds against SARS-CoV-2 spike protein-induced inflammation

To further solidify that IPA, DPHC, Eckmaxol, and Dieckol exhibit anti-inflammatory activity in a SARS-CoV-2 spike protein-induced endotoxic shock model, 3 days post fertilized (dpf) zebrafish larvae were microinjected with SARS-CoV-2 spike protein in the presence or absence of IPA, DPHC, Eckmaxol, and Dieckol or PBS or Dexamethasone (50 μ M). Initially, the toxicity of 12. μ g/ mL IPA, DPHC, Eckmaxol, and Dieckol were evaluated and confirmed the non-toxicity during the experiment (Fig 13 a). Then the different amount of spike protein was microinjected into the yolk sac of the 3dpf zebrafish larvae to confirm the toxicity. The group that injected 5 ng into the yolk sac showed a significant mortality rate than the other group (Fig. 13b). Therefore, 0.1-2 ng of spike protein was injected into the yolk sac of 3dpf larvae, and measure the gene expression level of TNF- α , IL-6, and IL-1 β at 6h time gaps until 24h. According to the results, 18h and 24h showed significant up-regulation of the inflammatory cytokine gene expression, and there was a significant reduction in 24h than 18h (Fig. 13c).

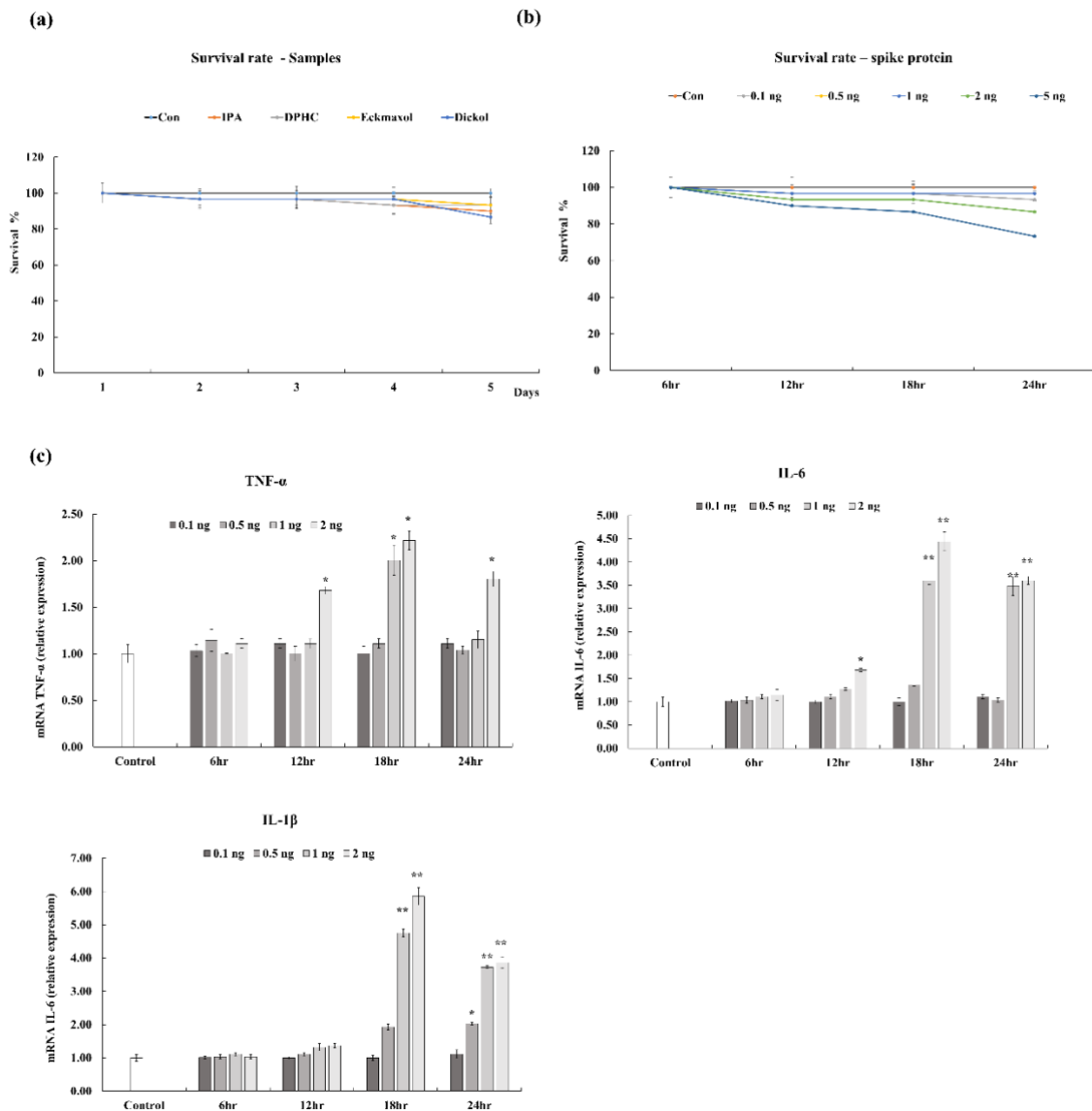


Fig 13. In-vivo evaluation of SARS-CoV-2 spike protein-induced inflammation. (a) toxicity of the Ishophloroglucin A (IPA), Diphlorethohydroxycarmalol (DPHC), Eckmaxol, and Dieckol and (b) spike protein in zebrafish, (c) SARS-CoV-2 spike protein induced inflammatory cytokine production in zebrafish at different time points after microinjection. Triplicate experiments were used to evaluate the data and the mean value is expressed with \pm SD. * $p < 0.05$, ** $p < 0.01$, against spike-treated group or ## $p < 0.01$, against control (ANOVA, Duncan's multiple range test).

The heart beating rate of the 2 ng of SARS-CoV-2 spike protein injected zebrafish larvae was measured after 18 h of the microinjection. The results showed a significant up-regulation of heartbeat rate in the SARS-CoV-2 spike protein-induced group, and IPA, DPHC, Eckmaxol, Dieckol, and dexamethasone significantly down-regulated the increased heartbeat rate (Fig. 14a).

The inhibitory potential of IPA, DPHC, Eckmaxol, and Dieckol against SARS-CoV-2 spike protein-induced inflammation was confirmed by injecting 2 ng of spike protein into 3 dpf zebrafish larvae for 18 h.

After that, the time-dependent expression of proinflammatory cytokines gene expression such as TNF- α , IL-6, and IL-1 β was evaluated. In the spike protein-microinjected condition, all genes tested in this study were expressed and reached maximal levels at 18 h, with a slightly different expression pattern. The zebrafish larvae that grew in the IPA, DPHC, Eckmaxol, and Dieckol-contained E3 media showed significant downregulation of expression levels of these genes (Fig. 14b). Further, CCL20, chemokine expression in the SARS-CoV-2 spike protein-induced zebrafish larvae was significantly up-regulated. It was significantly down-regulated by IPA, DPHC, Eckmaxol, and Dieckol (Fig. 14c).

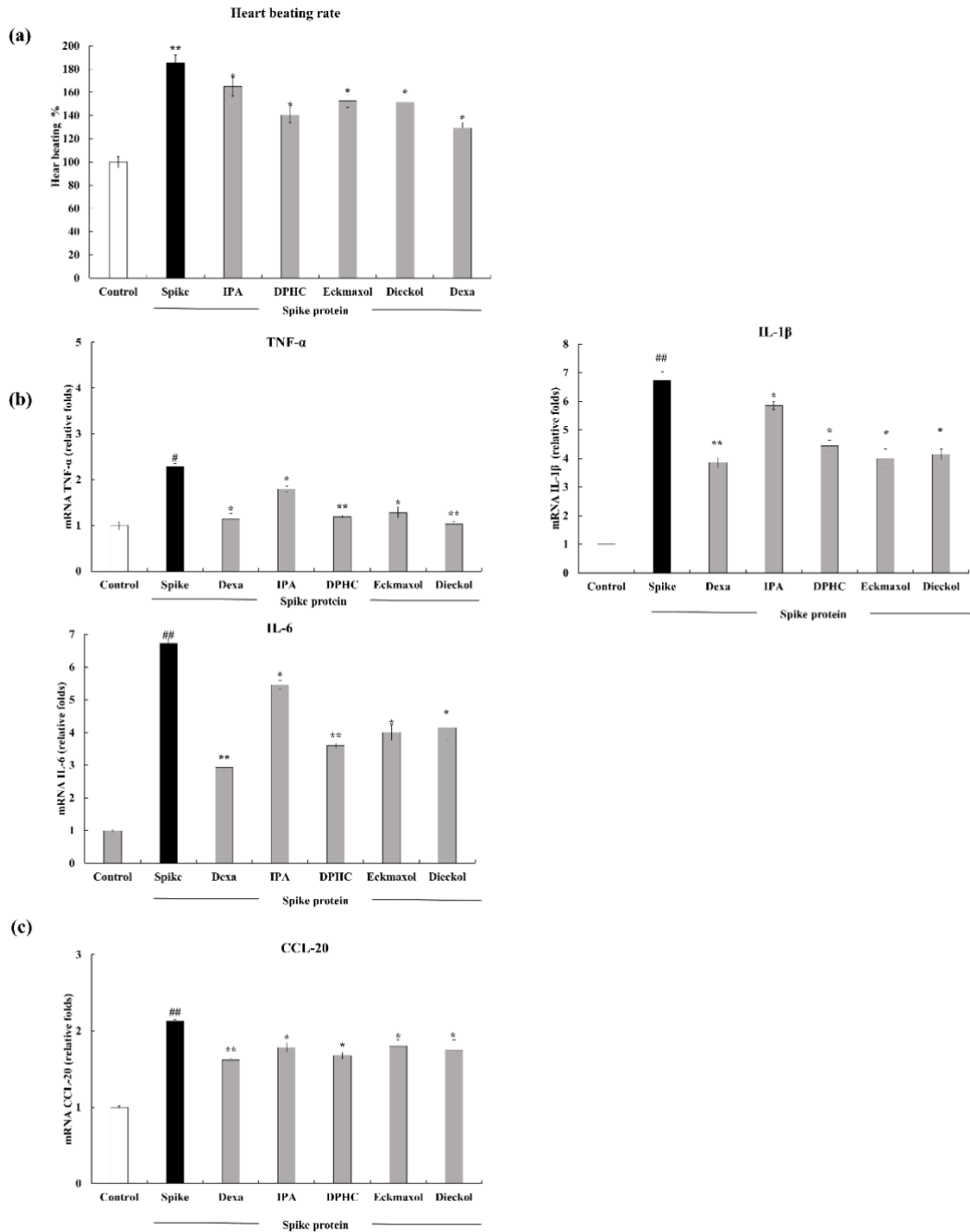


Fig 14. Anti-inflammatory effect of Ishophloroglucin A (IPA), Diphlorethohydroxycarmalol (DPHC), Eckmaxol, and Dieckol in SARS-CoV-2 spike protein-induced zebrafish. (a) heart beating rate evaluation, (b) SARS-CoV-2 spike protein induced inflammatory cytokine and (c) chemokine gene expression in zebrafish and evaluation of the inhibitory potential of Ishophloroglucin A (IPA), Diphlorethohydroxycarmalol (DPHC), Eckmaxol, and Dieckol. Triplicate experiments were used to evaluate the data and the mean value is expressed with \pm SD. * $p < 0.05$, ** $p < 0.01$, against spike-treated group or ## $p < 0.01$, against control (ANOVA, Duncan's multiple range test).

Furthermore, the author sought to determine whether IPA, DPHC, Eckmaxol, and Dieckol prevent the recruitment of macrophages and neutrophils to the inflammatory site in SARS-CoV-2 spike protein-microinjected zebrafish larvae. Neutral red staining revealed that spike protein injection significantly increased the macrophage counts at the site where spike protein was injected (inflammatory site) in the yolk sac (red color in the red box) at 18 h; however, immersion in IPA, DPHC, Eckmaxol, and Dieckol or dexamethasone resulted in a gradual decrease in the accumulation of macrophages in the yolk sac (Fig. 15a), indicating that IPA, DPHC, Eckmaxol, and Dieckol inhibits the recruitment of macrophages from the circulating blood to the yolk sac, leading to the generation of anti-inflammatory responses. In alignment with the inhibition of macrophage recruitment, spike protein -microinjection significantly decreased the large and clear cytolymph lipid droplets (accumulation of neutrophils: black dots) in the posterior blood island (PBI) as neutrophils infiltrated the inflammatory site, which indicates that polyphenolic compounds attenuate the recruitment of neutrophils to the spike-microinjected site. These results indicate that IPA, DPHC, Eckmaxol, and Dieckol inhibit the spike protein-induced inflammatory response by suppressing the expression of pro-inflammatory cytokine and chemokine genes and reducing macrophage and neutrophil recruitment to the inflammatory sites (Fig 15b and c).

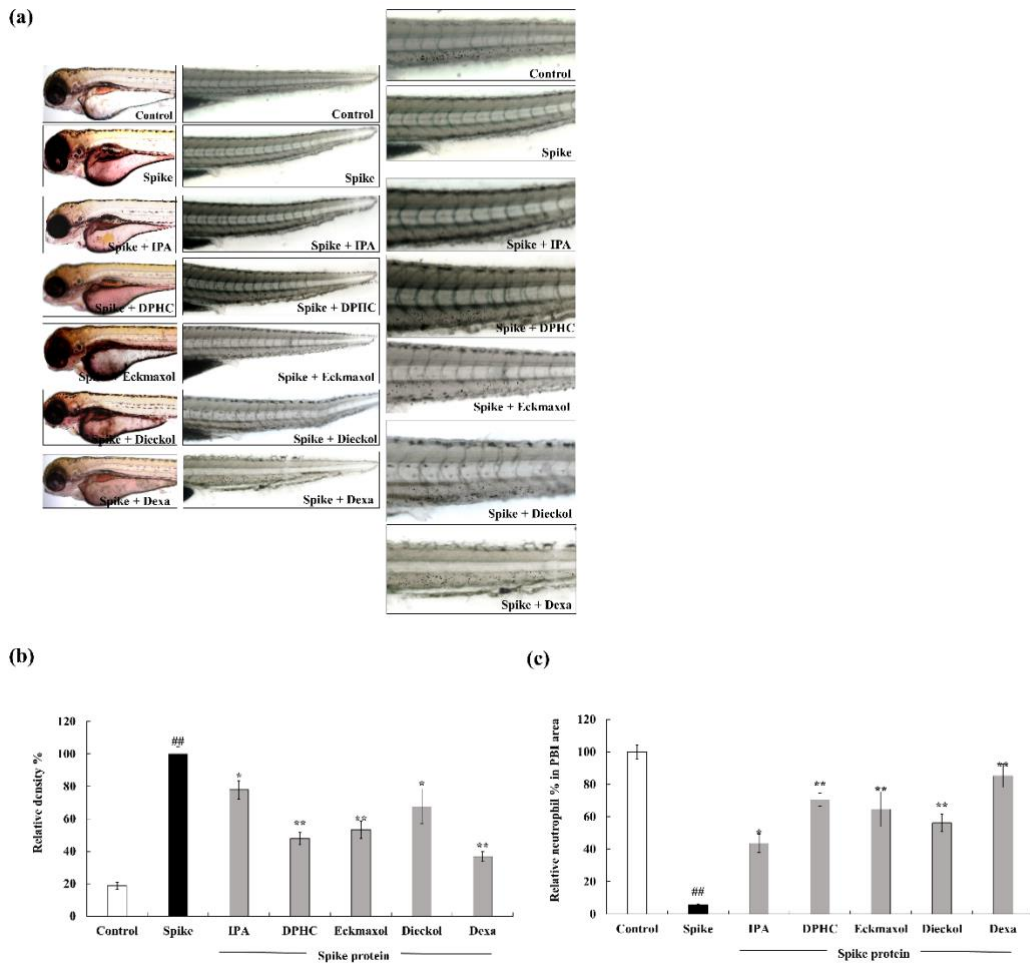


Fig 15. Macrophage and neutrophil migration in SARS-CoV-2 spike protein-induced zebrafish. (a) macrophage and neutrophil staining in zebrafish, (b) quantification of macrophage accumulation in yolks sac and (c) quantification of neutrophils in posterior blood island (PBI) area of zebrafish. Triplicate experiments were used to evaluate the data and the mean value is expressed with \pm SD. * $p < 0.05$, ** $p < 0.01$, against spike-treated group or ## $p < 0.01$, against control (ANOVA, Duncan's multiple range test).

4. Discussion

SARS-CoV-2 infection, replication, and aberrant host immune response are responsible for Covid-19 pathogenesis [92]. The initial host immune response against SARS-CoV-2 infection involves innate immune cells, such as macrophages, monocytes, neutrophils, and dendritic cells [108]. Cytokines, chemokines, and other inflammatory mediators produced by these cells inhibit virus replication, heal the damage, and activate the adaptive immune system. However, the uncontrolled release of cytokines, chemokines, and reactive oxygen species often exerts pathological consequences such as tissue injury, systemic inflammation, and organ failure [92]. Non-surviving COVID-19 patients exhibited a massive influx of macrophages and neutrophils. However, they reduced T cells in their blood [108], pointing to the association of hyper-activation of innate immune cells with COVID-19 pathogenesis. Indeed, the innate immune response is heightened in the lung of COVID-19 patients [109].

Epithelial cells of the lungs, kidneys, intestines, and vascular endothelial cells are the primary target of SARS-CoV-2 [96]. To understand whether cytosolic expression of SARS-CoV-2 affects inflammatory modulation, the author transfected spike protein to A549 and HEK-293 cells. The pro-inflammatory cytokine production of each cell was evaluated until 24 h, and results showed no significant upregulation of TNF- α , IL-6, and IL-1 β production due to the cytosolic expression of the SARS-CoV-2 spike protein. These data suggest that cytosolic spike protein does not trigger inflammation in epithelial cells. To further evaluation of the contribution of cytokine production of spike protein transfected epithelial cells, the author collected culture supernatant of spike protein transfected A549-S and HEK293T cells and added (50% v/v) into MHS and RAW264.7 cells, respectively. However, there was not any significant upregulation of these pro-

inflammatory cytokine productions. Therefore, these results provide an insight that the receptor on the cell surface should identify spike protein to induce inflammation in the cells. Therefore, the author treated the spike protein to A549 and MHS cells and evaluated the cell's gene expression and protein expression. Initially, cytotoxicity was calculated to determine the optimum spike protein concentration to evaluate the inflammatory induction of the SARS-CoV-2 spike protein mechanism. According to the results, 10-1000 ng/ mL and 10-500 ng/ mL spike protein concentrations were selected for further studies of A549 and MHS cells, respectively. The pro-inflammatory cytokine and chemokine gene expression in MHS cells at 4h and 8h were evaluated after treating 10-500 ng/ mL SARS-CoV-2 spike protein. The qPCR results revealed that cytokine and chemokine gene expression were significantly up-regulated at 500 ng/ mL group after 8h. The same experiment was performed for A549 cells using 10-1000 ng/ mL, and results revealed that epithelial cell was not induced at 8h after treating any concentration of spike protein. Therefore, the incubation time was increased to 24h, revealing that 1000 ng/ mL significantly up-regulated cytokine and chemokine expression. Further, these results suggested that macrophages are more sensitive to the presence of the spike protein than epithelial cells, and these results encouraged further evaluation of SARS-CoV-2 spike protein expression in a time-dependent manner.

Inflammatory genes are transcriptionally regulated by transcription factors that are activated by signaling pathways such as NF- κ B and MAPK. To obtain further insight into how SARS-CoV-2 spike protein induces the expression of inflammatory mediators, we stimulated A549 cells with spike protein. Cell lysates collected at various times following stimulation were analyzed for the activation of these inflammatory pathways by Western blotting. According to the results, P50, P65, and I κ B α were phosphorylated in cells treated with spike protein. MAPK pathways, including ERK, P38, and JNK, are often

activated concomitant to the NF- κ B pathway. Surprisingly, there was no activation of ERK and JNK in S2-stimulated cells. To further confirm the results, the author performed the same experiment on MHS cells and confirmed that the SARS-CoV-2 spike protein activated only the NF- κ B pathway. To understand the effect of ACE-2 expression of the host cell on the inducing inflammation by spike protein, the author treated HEK293T and HEK293T-ACE-2 cells with SARS-CoV-2 spike protein and evaluated the gene expression of cytokines. Results showed no significant difference in the gene expression of TNF- α , IL-6, and IL-1 β between the two cells, and this confirmed that spike protein induced the inflammation in the cell through another protein. Further, the heat-inactivated spike protein results confirmed that the three-dimensional structure was essential to this identification.

Based on all these results, we confirmed that the SARS-CoV-2 spike protein induced the epithelial and macrophage cells independently from the ACE-2 receptor, and the structure of the spike protein plays a key role. Further, spike protein identified by the cell surface receptor of the cells and macrophages was more rapidly induced by spike protein than epithelial cells. Then we evaluated the anti-inflammatory potential of IPA, DPHC, Eckmaxol, and Dieckol against SARS-CoV-2. Here epithelial cells were induced by 1000 ng/ mL and evaluated the results at 24h after a spike protein treatment. Macrophages were induced by 500 ng/ mL spike protein and evaluated the results at 8h after a spike protein treatment. Initially, the cytotoxicity of each compound was evaluated, and 1.563, 6.25, and 12.5 μ g/ mL were selected as safe doses based on the cytotoxicity of all compounds in both cell lines. The qPCR results of TNF- α , IL-6, and IL-1 β showed significant up-regulation of gene expression with SARS-CoV-2 spike protein in both A549 and MHS cell lines, and TLR2 inhibitor significantly down-regulated it. These results aligned with the previous studies. However, some studies have proved that SARS-CoV-2 spike

protein-induced inflammation through the TLR4 receptor. This is still not fully revealed [110-112]. This up-regulation of each gene expression was significant and dose-dependently downregulated by IPA, DPHC, Eckmaxol, and Dieckol.

Further, we evaluated the inhibitory potential of each compound against SARS-CoV-2-induced chemokine expression, and the gene expression of CXCL-1 and CXCL-2 was significantly down-regulated by TLR2 inhibitor, IPA, DPHC, Eckmaxol, and Dieckol in both cell lines. These gene expression evaluation results were further solidified by western blot analysis. The NF- κ B signaling pathway's protein expression showed significant up-regulation of the phosphorylation with a spike protein treatment. It was down-regulated by TLR-2 inhibitor, IPA, DPHC, Eckmaxol, and Dieckol in both cell lines. Further, these results followed a similar pattern with gene expression evaluation.

Inflammatory responses of COVID-19 patients are mostly contributed by innate immune cells, but they weakly express ACE-2 [113]. There is no strong evidence that SARS-CoV-2 infects and propagates infection in immune cells. Thus, it is intriguing how innate immune cells become activated to produce inflammatory mediators during SARS-CoV-2 infection. We propose a mechanism involved in hyper-inflammatory responses during SARS-CoV-2 infection. First, innate immune cells like macrophages recognize the spike protein of SARS-CoV-2 at the cell surface through TLR2, activating the NF- κ B pathway. Immune sensing of spike protein is independent of ACE-2, which was proved by treating SARS-CoV-2 spike protein to HEK-293T and HEK293T-ACE-2 expressing similar inflammatory cytokine responses. Further, epithelial cells can be activated by spike protein extracellularly, leading to the induction of pro-inflammatory cytokines and chemokines.

The Zebrafish in-vivo model further analyzed these results. Initially, we confirmed the non-toxicity of each compound on zebrafish. We selected the 0.1-2 ng of SARS-CoV-2 spike protein to proceed with the experiment by micro-injecting it into the yolk sac of the 3dpf zebrafish. Based on the qPCR results, until 24h after micro-inject 0.1-2 ng of spike protein into the yolk sac of zebrafish confirmed that 2 ng of spike protein and 18h incubation was the optimum conditions to evaluate the anti-inflammatory potential of IPA, DPHC, Eckmaxol, and Dieckol. Therefore, we initially evaluated the zebrafish's heart beating rate after treating SARS-CoV-2 spike protein pretreated with IPA, DPHC, Eckmaxol, and Dieckol. Spike protein significantly increases the heart beating rate, and IPA, DPHC, Eckmaxol, and Dieckol significantly downregulated it.

Further, the qPCR results of TNF- α , IL-6, IL-1 β , and CCL-20 also significantly downregulate the spike protein-induced gene expression. These results were further solidified by analyzing macrophage and neutrophil migration of SARS-CoV-2 spike protein-induced zebrafish. Neutral red staining revealed the accumulation of macrophage in spike protein micro-injected yolk sac, and IPA, DPHC, Eckmaxol, and Dieckol significantly downregulated it. Further, neutrophils in the PBI area were also migrated to the yolk sac in the spike protein-treated group, and it was significantly down-regulated in the polyphenolic compounds pretreated groups. Furthermore, gene expression analysis of cytokines and chemokines was further solidified by these in-vivo results.

5. Conclusion

In summary, this study documents a potential mechanism for the inflammatory response induced by SARS-CoV-2. We demonstrate that SARS-CoV-2 spike protein is a potent viral pathogen-associated molecular pattern (PAMP) that, upon sensing by TLR2, activates the NF- κ B pathway, leading to the expression of inflammatory mediators in innate immune and epithelial cells. IPA, DPHC, Eckmaxol, and Dieckol significantly down-regulated the SARS-CoV-2 spike protein-induced inflammation via regulating pro-inflammatory cytokine and chemokine expressions.

References

1. Zhou, P., et al., *A pneumonia outbreak associated with a new coronavirus of probable bat origin*. *nature*, 2020. **579**(7798): p. 270-273.
2. Huang, C., et al., *Clinical features of patients infected with 2019 novel coronavirus in Wuhan, China*. *The lancet*, 2020. **395**(10223): p. 497-506.
3. Lau, S.K., et al., *Severe acute respiratory syndrome coronavirus-like virus in Chinese horseshoe bats*. *Proceedings of the National Academy of Sciences*, 2005. **102**(39): p. 14040-14045.
4. Rothan, H.A. and S.N. Byrareddy, *The epidemiology and pathogenesis of coronavirus disease (COVID-19) outbreak*. *Journal of autoimmunity*, 2020. **109**: p. 102433.
5. Li, F., *Structure, function, and evolution of coronavirus spike proteins*. *Annual review of virology*, 2016. **3**: p. 237-261.
6. Du, L., et al., *The spike protein of SARS-CoV—a target for vaccine and therapeutic development*. *Nature Reviews Microbiology*, 2009. **7**(3): p. 226-236.
7. Li, F., *Receptor recognition mechanisms of coronaviruses: a decade of structural studies*. *Journal of virology*, 2015. **89**(4): p. 1954-1964.
8. Lu, R., et al., *Genomic characterisation and epidemiology of 2019 novel coronavirus: implications for virus origins and receptor binding*. *The lancet*, 2020. **395**(10224): p. 565-574.
9. Naqvi, A.A.T., et al., *Insights into SARS-CoV-2 genome, structure, evolution, pathogenesis and therapies: Structural genomics approach*. *Biochimica et Biophysica Acta (BBA)-Molecular Basis of Disease*, 2020. **1866**(10): p. 165878.
10. Anand, K., et al., *Coronavirus main proteinase (3CLpro) structure: basis for design of anti-SARS drugs*. *Science*, 2003. **300**(5626): p. 1763-1767.
11. Ghosh, A.K., et al., *Design and synthesis of peptidomimetic severe acute respiratory syndrome chymotrypsin-like protease inhibitors*. *Journal of medicinal chemistry*, 2005. **48**(22): p. 6767-6771.
12. Kumar, V., et al., *Identification, synthesis and evaluation of SARS-CoV and MERS-CoV 3C-like protease inhibitors*. *Bioorganic & medicinal chemistry*, 2016. **24**(13): p. 3035-3042.
13. Pillaiyar, T., et al., *An overview of severe acute respiratory syndrome—coronavirus (SARS-CoV) 3CL protease inhibitors: peptidomimetics and small molecule chemotherapy*. *Journal of medicinal chemistry*, 2016. **59**(14): p. 6595-6628.
14. Shin, D., et al., *Papain-like protease regulates SARS-CoV-2 viral spread and innate immunity*. *Nature*, 2020. **587**(7835): p. 657-662.
15. Solan, M. and N. Whiteley, *Stressors in the marine environment: physiological and ecological responses; societal implications*. 2016: Oxford University Press.
16. Mostafa, S.S., *Microalgal biotechnology: prospects and applications*. *Plant science*, 2012. **12**: p. 276-314.
17. Rengasamy, K.R., et al., *Potential antiradical and alpha-glucosidase inhibitors from *Ecklonia maxima* (Osbeck) Papenfuss*. *Food chemistry*, 2013. **141**(2): p. 1412-1415.
18. Li, A.-N., et al., *Resources and biological activities of natural polyphenols*. *Nutrients*, 2014. **6**(12): p. 6020-6047.
19. Kim, A.-R., et al., *Isolation and identification of phlorotannins from *Ecklonia stolonifera* with antioxidant and anti-inflammatory properties*. *Journal of agricultural and food chemistry*, 2009. **57**(9): p. 3483-3489.

20. Cho, H.M., et al., *Dereplication by high-performance liquid chromatography (HPLC) with quadrupole-time-of-flight mass spectroscopy (qTOF-MS) and antiviral activities of phlorotannins from Ecklonia cava*. Marine Drugs, 2019. **17**(3): p. 149.
21. Venkatesan, J., et al., *Phlorotannins*. Encyclopedia of food chemistry, 2019: p. 515.
22. Yang, H.-K., et al., *Efficacy of algal Ecklonia cava extract against viral hemorrhagic septicemia virus (VHSV)*. Fish & Shellfish Immunology, 2018. **72**: p. 273-281.
23. Jin, Z., et al., *Structure of Mpro from SARS-CoV-2 and discovery of its inhibitors*. Nature, 2020. **582**(7811): p. 289-293.
24. Gao, X., et al., *Crystal structure of SARS-CoV-2 papain-like protease*. Acta Pharmaceutica Sinica B, 2020.
25. Zhou, X., et al., *Isolation and purification of a neuroprotective phlorotannin from the marine algae Ecklonia maxima by size exclusion and high-speed counter-current chromatography*. Marine Drugs, 2019. **17**(4): p. 212.
26. Ryu, B., et al., *Ishophloroglucin A, a novel phlorotannin for standardizing the anti- α -glucosidase activity of Ishige okamurae*. Marine drugs, 2018. **16**(11): p. 436.
27. Kim, H.-S., et al., *High-performance centrifugal partition chromatography (HPCPC) for efficient isolation of diphloretohydroxycarmalol (DPHC) and screening of its antioxidant activity in a zebrafish model*. Process Biochemistry, 2020. **88**: p. 189-196.
28. Li, X.-Q., et al., *COMPARISON OF INHIBITORY EFFECTS OF THE PROTON PUMP-INHIBITING DRUGS OMEPRAZOLE, ESOMEPRAZOLE, LANSOPRAZOLE, PANTOPRAZOLE, AND RABEPRAZOLE ON HUMAN CYTOCHROME P450 ACTIVITIES*. Drug Metabolism and Disposition, 2004. **32**(8): p. 821.
29. Fu, L., et al., *Both Boceprevir and GC376 efficaciously inhibit SARS-CoV-2 by targeting its main protease*. Nature communications, 2020. **11**(1): p. 4417.
30. Gao, X., et al., *Crystal structure of SARS-CoV-2 papain-like protease*. Acta Pharmaceutica Sinica B, 2021. **11**(1): p. 237-245.
31. Hajbabaie, R., M.T. Harper, and T. Rahman, *Establishing an analogue based in silico pipeline in the pursuit of novel inhibitory scaffolds against the SARS coronavirus 2 papain-like protease*. Molecules, 2021. **26**(4): p. 1134.
32. Pillaiyar, T., S. Meenakshisundaram, and M. Manickam, *Recent discovery and development of inhibitors targeting coronaviruses*. Drug discovery today, 2020. **25**(4): p. 668-688.
33. Joubert, P., et al., *Identification of a new cleavage site of the 3C-like protease of rabbit haemorrhagic disease virus*. Journal of General Virology, 2000. **81**(2): p. 481-488.
34. Lin, C.-W., et al., *Anti-SARS coronavirus 3C-like protease effects of Isatis indigotica root and plant-derived phenolic compounds*. Antiviral research, 2005. **68**(1): p. 36-42.
35. Park, J.-Y., et al., *Dieckol, a SARS-CoV 3CLpro inhibitor, isolated from the edible brown algae Ecklonia cava*. Bioorganic & medicinal chemistry, 2013. **21**(13): p. 3730.
36. Harrison, A.G., T. Lin, and P. Wang, *Mechanisms of SARS-CoV-2 transmission and pathogenesis*. Trends in immunology, 2020. **41**(12): p. 1100-1115.
37. Gorshkov, K., et al., *The SARS-CoV-2 cytopathic effect is blocked with autophagy modulators*. Biorxiv, 2020.
38. Shinde, P., P. Banerjee, and A. Mandhare, *Marine natural products as source of new drugs: a patent review (2015–2018)*. Expert Opinion on Therapeutic Patents, 2019. **29**(4): p. 283-309.
39. Yasuhara-Bell, J. and Y. Lu, *Marine compounds and their antiviral activities*. Antiviral Res, 2010. **86**(3): p. 231-40.
40. Li, F., *Structure, Function, and Evolution of Coronavirus Spike Proteins*. Annu Rev Virol, 2016. **3**(1): p. 237-261.
41. Perlman, S. and J. Netland, *Coronaviruses post-SARS: update on replication and pathogenesis*. Nat Rev Microbiol, 2009. **7**(6): p. 439-50.

42. Du, L., et al., *The spike protein of SARS-CoV--a target for vaccine and therapeutic development*. Nat Rev Microbiol, 2009. **7**(3): p. 226-36.
43. Li, F., *Receptor recognition mechanisms of coronaviruses: a decade of structural studies*. J Virol, 2015. **89**(4): p. 1954-64.
44. Li, W., et al., *Angiotensin-converting enzyme 2 is a functional receptor for the SARS coronavirus*. Nature, 2003. **426**(6965): p. 450-4.
45. Li, F., et al., *Structure of SARS coronavirus spike receptor-binding domain complexed with receptor*. Science, 2005. **309**(5742): p. 1864-8.
46. Yuan, Y., et al., *Cryo-EM structures of MERS-CoV and SARS-CoV spike glycoproteins reveal the dynamic receptor binding domains*. Nat Commun, 2017. **8**(1): p. 15092.
47. Gui, M., et al., *Cryo-electron microscopy structures of the SARS-CoV spike glycoprotein reveal a prerequisite conformational state for receptor binding*. Cell Res, 2017. **27**(1): p. 119-129.
48. Belouzard, S., et al., *Mechanisms of coronavirus cell entry mediated by the viral spike protein*. Viruses, 2012. **4**(6): p. 1011-33.
49. Heald-Sargent, T. and T. Gallagher, *Ready, set, fuse! The coronavirus spike protein and acquisition of fusion competence*. Viruses, 2012. **4**(4): p. 557-80.
50. Bolles, M., E. Donaldson, and R. Baric, *SARS-CoV and emergent coronaviruses: viral determinants of interspecies transmission*. Curr Opin Virol, 2011. **1**(6): p. 624-34.
51. Frieman, M. and R. Baric, *Mechanisms of severe acute respiratory syndrome pathogenesis and innate immunomodulation*. Microbiol Mol Biol Rev, 2008. **72**(4): p. 672-85, Table of Contents.
52. Li, F., *Receptor recognition and cross-species infections of SARS coronavirus*. Antiviral Res, 2013. **100**(1): p. 246-54.
53. Xu, Z., et al., *Nelfinavir was predicted to be a potential inhibitor of 2019-nCov main protease by an integrative approach combining homology modelling, molecular docking and binding free energy calculation*. 2020: p. 2020.01.27.921627.
54. Zhou, P., et al., *A pneumonia outbreak associated with a new coronavirus of probable bat origin*. Nature, 2020. **579**(7798): p. 270-273.
55. Letko, M., A. Marzi, and V. Munster, *Functional assessment of cell entry and receptor usage for SARS-CoV-2 and other lineage B betacoronaviruses*. Nat Microbiol, 2020. **5**(4): p. 562-569.
56. Shang, J., et al., *Structural basis of receptor recognition by SARS-CoV-2*. Nature, 2020. **581**(7807): p. 221-224.
57. Walls, A.C., et al., *Structure, Function, and Antigenicity of the SARS-CoV-2 Spike Glycoprotein*. Cell, 2020. **181**(2): p. 281-292 e6.
58. Wrapp, D., et al., *Cryo-EM structure of the 2019-nCoV spike in the prefusion conformation*. Science, 2020. **367**(6483): p. 1260-1263.
59. Hoffmann, M., et al., *SARS-CoV-2 Cell Entry Depends on ACE2 and TMPRSS2 and Is Blocked by a Clinically Proven Protease Inhibitor*. Cell, 2020. **181**(2): p. 271-280 e8.
60. Ou, X., et al., *Characterization of spike glycoprotein of SARS-CoV-2 on virus entry and its immune cross-reactivity with SARS-CoV*. Nat Commun, 2020. **11**(1): p. 1620.
61. Hoffmann, M., et al., *SARS-CoV-2 Cell Entry Depends on ACE2 and TMPRSS2 and Is Blocked by a Clinically Proven Protease Inhibitor*. Cell, 2020. **181**(2): p. 271-280.e8.
62. Xu, Z., et al., *Pathological findings of COVID-19 associated with acute respiratory distress syndrome*. Lancet Respir Med. 2020; **8** (4): 420–422. Published online, 2020.
63. Wang, Q., et al., *Structural and Functional Basis of SARS-CoV-2 Entry by Using Human ACE2*. Cell, 2020. **181**(4): p. 894-904.e9.
64. Lassen, K.G., et al., *A Flexible Model of HIV-1 Latency Permitting Evaluation of Many Primary CD4 T-Cell Reservoirs*. PLOS ONE, 2012. **7**(1): p. e30176.

65. Lo, H.-L. and J.-K. Yee, *Production of Vesicular Stomatitis Virus G Glycoprotein (VSV-G) Pseudotyped Retroviral Vectors*. Current Protocols in Human Genetics, 2007. **52**(1): p. 12.7.1-12.7.11.
66. Wang, X., et al., *Polygoni multiflori radix extracts inhibit SARS-CoV-2 pseudovirus entry in HEK293T cells and zebrafish larvae*. Phytomedicine, 2022. **102**: p. 154154.
67. Jeffers, S.A., et al., *CD209L (L-SIGN) is a receptor for severe acute respiratory syndrome coronavirus*. Proceedings of the National Academy of Sciences of the United States of America, 2004. **101**(44): p. 15748.
68. Fang, L., G. Karakiulakis, and M. Roth, *Antihypertensive drugs and risk of COVID-19? - Authors' reply*. The Lancet. Respiratory medicine, 2020. **8**(5): p. e32-e33.
69. Donoghue, M., et al., *A Novel Angiotensin-Converting Enzyme-Related Carboxypeptidase (ACE2) Converts Angiotensin I to Angiotensin 1-9*. Circulation Research, 2000. **87**(5): p. e1-e9.
70. Yan, R., et al., *Structural basis for the recognition of SARS-CoV-2 by full-length human ACE2*. Science, 2020. **367**(6485): p. 1444-1448.
71. Hamming, I., et al., *Tissue distribution of ACE2 protein, the functional receptor for SARS coronavirus. A first step in understanding SARS pathogenesis*. The Journal of Pathology: A Journal of the Pathological Society of Great Britain and Ireland, 2004. **203**(2): p. 631-637.
72. Lukassen, S., et al., *SARS-CoV-2 receptor ACE2 and TMPRSS2 are predominantly expressed in a transient secretory cell type in subsegmental bronchial branches*. bioRxiv, 2020: p. 2020.03.13.991455.
73. Hoffmann, M., et al., *SARS-CoV-2 Cell Entry Depends on ACE2 and TMPRSS2 and Is Blocked by a Clinically Proven Protease Inhibitor*. Cell, 2020. **181**(2): p. 271-280 e8.
74. Jia, H.P., et al., *ACE2 Receptor Expression and Severe Acute Respiratory Syndrome Coronavirus Infection Depend on Differentiation of Human Airway Epithelia*. Journal of Virology, 2005. **79**(23): p. 14614.
75. Sanders, D.A., *No false start for novel pseudotyped vectors*. Current opinion in biotechnology, 2002. **13**(5): p. 437-442.
76. Ory, D.S., B.A. Neugeboren, and R.C. Mulligan, *A stable human-derived packaging cell line for production of high titer retrovirus/vesicular stomatitis virus G pseudotypes*. Proceedings of the National Academy of Sciences, 1996. **93**(21): p. 11400-11406.
77. Zhang, L., et al., *A bioluminescent imaging mouse model for Marburg virus based on a pseudovirus system*. Human Vaccines & Immunotherapeutics, 2017. **13**(8): p. 1811-1817.
78. Welch, S.R., et al., *Lassa and Ebola virus inhibitors identified using minigenome and recombinant virus reporter systems*. Antiviral Research, 2016. **136**: p. 9-18.
79. Bartosch, B., J. Dubuisson, and F.-L. Cosset, *Infectious hepatitis C virus pseudo-particles containing functional E1-E2 envelope protein complexes*. The Journal of experimental medicine, 2003. **197**(5): p. 633-642.
80. Radoshitzky, S.R., et al., *Transferrin receptor 1 is a cellular receptor for New World haemorrhagic fever arenaviruses*. Nature, 2007. **446**(7131): p. 92-96.
81. Yang, L., et al., *Identification of SARS-CoV-2 entry inhibitors among already approved drugs*. Acta Pharmacologica Sinica, 2021. **42**(8): p. 1347-1353.
82. Nie, J., et al., *Development of in vitro and in vivo rabies virus neutralization assays based on a high-titer pseudovirus system*. Scientific reports, 2017. **7**(1): p. 42769.
83. Zettl, F., et al., *Rapid quantification of SARS-CoV-2-neutralizing antibodies using propagation-defective vesicular stomatitis virus pseudotypes*. Vaccines, 2020. **8**(3): p. 386.

84. He, S., et al., *PSGL-1 inhibits the incorporation of SARS-CoV and SARS-CoV-2 Spike glycoproteins into pseudovirions and impairs pseudovirus attachment and infectivity*. *Viruses*, 2020. **13**(1): p. 46.
85. Yang, R., et al., *Development and effectiveness of pseudotyped SARS-CoV-2 system as determined by neutralizing efficiency and entry inhibition test in vitro*. *Biosafety and health*, 2020. **2**(4): p. 226-231.
86. Zhu, Y., et al., *Design of potent membrane fusion inhibitors against SARS-CoV-2, an emerging coronavirus with high fusogenic activity*. *Journal of virology*, 2020. **94**(14): p. e00635-20.
87. Wan, J., et al., *Human-IgG-neutralizing monoclonal antibodies block the SARS-CoV-2 infection*. *Cell Reports*, 2020. **32**(3): p. 107918.
88. Huang, S.-W., et al., *Assessing the application of a pseudovirus system for emerging SARS-CoV-2 and re-emerging avian influenza virus H5 subtypes in vaccine development*. *biomedical journal*, 2020. **43**(4): p. 375-387.
89. Ou, X., et al., *Characterization of spike glycoprotein of SARS-CoV-2 on virus entry and its immune cross-reactivity with SARS-CoV*. *Nature communications*, 2020. **11**(1): p. 1620.
90. Walther, T. and W.M. Kuebler, *Don't judge too RASHly: the multifaceted role of the renin-angiotensin system and its therapeutic potential in COVID-19*. *American Journal of Physiology-Lung Cellular and Molecular Physiology*, 2020. **318**(5): p. L1023-L1024.
91. Palha, N., et al., *Real-time whole-body visualization of Chikungunya Virus infection and host interferon response in zebrafish*. *PLoS pathogens*, 2013. **9**(9): p. e1003619.
92. Britton, G., et al., *The Sinai Immunology Review Project. Immunology of COVID-19: current state of the science*. *Immunity*, 2020.
93. Tay, M., et al., *The trinity of COVID-19: immunity, inflammation and intervention*. *Nature Rev Immunol* **20** (6): 363–374. 2020.
94. Blanco-Melo, D., et al., *Imbalanced host response to SARS-CoV-2 drives development of COVID-19*. *Cell*, 2020. **181**(5): p. 1036-1045. e9.
95. Zhou, P., et al., *A pneumonia outbreak associated with a new coronavirus of probable bat origin*. *Nature*. Published online February 3, 2020. 2020.
96. Hoffmann, M., et al., *SARS-CoV-2 cell entry depends on ACE2 and TMPRSS2 and is blocked by a clinically proven protease inhibitor*. *cell*, 2020. **181**(2): p. 271-280. e8.
97. Walls, A.C., et al., *Structure, function, and antigenicity of the SARS-CoV-2 spike glycoprotein*. *Cell*, 2020. **181**(2): p. 281-292. e6.
98. Huang, C., et al., *Clinical features of patients infected with 2019 novel coronavirus in Wuhan*. *China Lancet*. 2020; **395** (10223): 497–506. 2020.
99. Khan, S., V. Godfrey, and M.H. Zaki, *Cytosolic nucleic acid sensors in inflammatory and autoimmune disorders*. *International Review of Cell and Molecular Biology*, 2019. **344**: p. 215-253.
100. Park, A. and A. Iwasaki, *Type I and type III interferons—induction, signaling, evasion, and application to combat COVID-19 cell host*. *Microbe* **27**: 870–878. 2020.
101. Kawasaki, T. and T. Kawai, *Toll-like receptor signaling pathways*. *Frontiers in immunology*, 2014. **5**: p. 461.
102. Kawai, T. and S. Akira, *TLR signaling*. *Cell Death & Differentiation*, 2006. **13**(5): p. 816-825.
103. Cheung, C.Y., et al., *Cytokine responses in severe acute respiratory syndrome coronavirus-infected macrophages in vitro: possible relevance to pathogenesis*. *Journal of virology*, 2005. **79**(12): p. 7819-7826.
104. Law, H.K., et al., *Chemokine up-regulation in SARS-coronavirus-infected, monocyte-derived human dendritic cells*. *Blood*, 2005. **106**(7): p. 2366-2374.

105. Wang, L., et al., *Protective effect of polysaccharides from Celluclast-assisted extract of Hizikia fusiforme against hydrogen peroxide-induced oxidative stress in vitro in Vero cells and in vivo in zebrafish*. International Journal of Biological Macromolecules, 2018. **112**: p. 483-489.
106. Nagahawatta, D.P., et al., *Sargachromenol Isolated from Sargassum horneri Inhibits Particulate Matter-Induced Inflammation in Macrophages through Toll-like Receptor-Mediated Cell Signaling Pathways*. Marine Drugs, 2022. **20**(1): p. 28.
107. Yang, L.-L., et al., *Endotoxin molecule lipopolysaccharide-induced zebrafish inflammation model: a novel screening method for anti-inflammatory drugs*. Molecules, 2014. **19**(2): p. 2390-2409.
108. Liao, M., et al., *Single-cell landscape of bronchoalveolar immune cells in patients with COVID-19*. Nature medicine, 2020. **26**(6): p. 842-844.
109. Zhou, Z., et al., *Heightened innate immune responses in the respiratory tract of COVID-19 patients*, Cell Host Microbes. 2020.
110. Satta, S., et al., *An engineered nano-liposome-human ACE2 decoy neutralizes SARS-CoV-2 Spike protein-induced inflammation in both murine and human macrophages*. Theranostics, 2022. **12**(6): p. 2639-2657.
111. Umar, S., et al., *Inhibition of IRAK4 dysregulates SARS-CoV-2 spike protein-induced macrophage inflammatory and glycolytic reprogramming*. Cellular and Molecular Life Sciences, 2022. **79**(6): p. 301.
112. Barhoumi, T., et al., *SARS-CoV-2 Coronavirus Spike Protein-Induced Apoptosis, Inflammatory, and Oxidative Stress Responses in THP-1-Like-Macrophages: Potential Role of Angiotensin-Converting Enzyme Inhibitor (Perindopril)*. Frontiers in Immunology, 2021. **12**.
113. Ropa, J., et al., *Human hematopoietic stem, progenitor, and immune cells respond ex vivo to SARS-CoV-2 spike protein*. Stem cell reviews and reports, 2021. **17**: p. 253-265.

Concluding remarks

The interested compounds were initially screened using in-silico evaluations and further confirmed their inhibitory potential against SARS-CoV-2 replication and survival. In the first part, 3CLpro and PLpro were identified as therapeutic drug targets against SARS-CoV-2 based on their pivotal role in polyprotein processing. The initial hypothesis was that all these compounds act as competitive inhibitors against 3CLpro and PLpro. Then molecular docking evaluation was performed based on the catalytic sites of these proteases. The best four compounds were selected based on the binding affinity with the active site of each protease enzyme. An in-vitro assay kit further evaluated the desired compounds and cell-based in-vitro evaluation. The outcomes of these results were further solidified using live SARS-CoV-2 viruses and evaluated the inhibitory potential of the cytopathic effect of each compound. Based on all these results, IPA, DPHC, Eckmaxol, and Dieckol were identified as potent inhibitors against SARS-CoV-2 replication and survival in the host cell.

In the second part of the study, the author evaluated the inhibitory potential of these compounds against the SARS-CoV-2 cell entry mechanism. Initial in-silico results confirmed that the high binding affinity of IPA, DPHC, Eckmaxol, and Dieckol did not show higher binding affinity compared to other compounds. Therefore, we selected IPA, DPHC, and Eckmaxol for in-vitro evaluation, and the inhibitory activity of each compound was confirmed. IPA, DPHC, and Eckmaxol's inhibitory activity were further confirmed using the SARS-CoV-2 pseudovirus and zebrafish in-vivo model. These results confirmed the inhibitory activity of IPA, DPHC, and Eckmaxol against the SARS-CoV-2 cell entry mechanism.

In the third part, we investigated the SARS-CoV-2 spike protein-induced cytokine storm and inhibitory potential of IPA, DPHC, Eckmaxol, and Dieckol. The results of the present section revealed that SARS-CoV-2 spike protein induced hyper-inflammation independently from the ACE-2 receptor and TLR-2 receptor-identified spike protein, depending on their structure. Therefore, the TLR-2 inhibitor significantly downregulated the SARS-CoV-2 spike protein-induced inflammation. Results of the gene expressions of cytokines and chemokines revealed that IPA, DPHC, Eckmaxol, and Dieckol significantly down-regulated the SARS-CoV-2 spike protein-induced pro-inflammatory cytokine and chemokine gene expressions and protein expressions. These results were further confirmed by gene expression analysis and macrophage and neutrophil migration analysis of the SARS-COV-2 spike protein-micro-injected zebrafish model.

These results strongly suggested the potential of IPA, DPHC, Eckmaxol, and Dieckol as inhibitors against SARS-CoV-2 replication, survival, and subsequent cytokine storm through a multi-target approach mechanism. Further, DPHC was identified as the most potent compound in the multi-target approach against SARS-CoV-2.

Acknowledgment

I would like to express my gratitude and honor to my supervisor, Professor Jeon You-Jin, Marine Bio-Resource Technology Lab, Department of Marine Life Sciences, Jeju National University. His expertise was vital in formulating the research; his consistent guidance steered me in the right direction. I'm grateful to Professor Jeon for allowing me to conduct my work and for the opportunity created for me at his laboratory.

I would also like to single out Dr. Asanka Sanjeewa, who introduced me to Professor Jeon and Dr. Thilina U. Jayawardena, Ms. N.M. Liyanage, Mrs. H.H.A.C.K. Jayawardhana, who are my long-term colleagues. Assistant, Associate Professors, post-doctoral positions, and all the lab mates are unforgettably mentioned with their dearest support towards my stay and work in the lab environment.

Finally, I must express my profound gratitude to my family for providing unfailing support throughout my years of study. This was accomplished with them.

Though I have not to pin-pointed with names of all the people who helped me, they are remembered, and my gratitude is extended to them.

D.P. Nagahawatta

요약

2019 년 코로나바이러스 감염증 (COVID-19)이라는 SARS-CoV-2 바이러스에 의해 유발된 최근의 대유행으로 인해 세계적인 보건 문제가 제기되었습니다. 이 코로나바이러스는 인플루엔자, 아데노바이러스, 조류 인플루엔자, 중증급성호흡기증후군 코로나바이러스(SARS-CoV), 중동호흡기증후군 코로나바이러스(MERS-CoV)와는 다른 독특한 특징을 가지고 있었습니다. SARS-CoV-2 의 실제 감염 방식은 아직 완전히 이해되지 않았으며, 바이러스가 인간을 주요 숙주로 선택하는 이유와 어떻게 기생적 면역체계를 우회하는지 등이 포함됩니다. 바이러스의 침입 메커니즘은 호흡기계를 통해 재채기와 기침으로 인한 호흡기 도매체를 통해 몸 속으로 들어가는 것으로 발견되었습니다. SARS-CoV-2 는 단백질 캡시드로 덮인 당단백질에 앵커된 가시 단백질로 구성되어 있습니다. 이 가시 단백질은 바이러스가 대상 세포로 침입하는 데 관여합니다. SARS-CoV-2 가 숙주 세포로의 침입은 감염성과 병원성 결정에 있어서 중요한 요소입니다. SARS-CoV-2 의 가시 단백질은 먼저 앵지오텐신 전환효소 2 (ACE-2)라는 세포 표면 수용체에 결합하여 바이러스와 연결됩니다. 이후, 바이러스는 엔도솜으로 들어가며, 마지막으로 바이러스 막이 리소솜 막과

융합합니다. 따라서 ACE-2: SARS-CoV-2 가시 단백질의 상호 작용을 방해할 수 있는 특정 화합물이 있다면 SARS-CoV-2 세포 침입 메커니즘에 대항하여 사용될 수 있는 잠재력을 가지고 있습니다.

SARS-CoV-2의 우수한 약물 표적 중 하나는 폴리단백질 처리에 중요한 역할을 하는 프로테아제인 NSP 3과 NSP 5입니다. 이들은 바이러스의 복제와 생존에 필수적인 기능적 비구조 단백질을 생성하기 위한 역할을 합니다. Nsp5(또는 3CLpro라고도 알려짐)는 복제효소 다발 단백질(1ab)을 11개의 다른 부위에서 가수분해합니다. 그 결과물들은 바이러스의 숙주 세포 내에서의 생존과 복제에 필요합니다. 파파인류 프로테아제(PLpro)는 바이러스 다발 단백질을 분해하고 염증과 항바이러스 우비퀴틴 유사 단백질 수정을 되돌립니다. 따라서 SARS-CoV-2 PLpro를 표적으로 하는 약물은 COVID-19의 치료 또는 예방에 효과적으로 사용될 수 있으며, 바이러스 부하를 감소시키고 기원적 면역 반응을 회복시킬 수 있습니다.

SARS-CoV-2의 감염과 복제는 복잡한 메커니즘으로, COVID-19 치료는 다중 표적 접근법이 가장 적절한 방법임을 시사합니다. 해조류로부터 얻은 생체 활성 성분은 천연물 연구에 새로운 통찰력을 제공해왔습니다. 본 연구는 해조류로부터

분리된 천연물을 사용하여 3CLpro, PLpro 및 SARS-CoV-2 세포 침입 메커니즘을 통해 SARS-CoV-2 를 억제하는 것을 목표로 합니다. 분자 도킹은 3CLpro, PLpro 및 ACE-2 단백질 구조를 기반으로 선택된 천연물을 초기에 스크리닝하는 데 사용되었습니다. 또한, 얻어진 화합물들은 억제 활성을 확인하기 위해 생물학적 실험을 위해 분리되고 사용되었습니다. 우선, 화합물들의 바이러스 세포 침입 메커니즘에 대한 억제력을 평가하기 위해 in-vitro 실험 키트를 사용했습니다. 그런 다음 이러한 결과는 세포 기반 실험을 통해 추가적으로 확인되었습니다. 여기에서 저자들은 ACE-2 가 과발현된 HEK293T 세포와 바이러스 막의 가시 단백질 및 염색체와 발광 효소 유전자로 이루어진 SARS-CoV-2 의사 바이러스를 개발했습니다. 저자는 qPCR 에서 절대 양 측정 방법을 사용하여 바이러스 수량을 계산하는 빠른 방법을 도입했습니다. 이러한 결과는 준어류체를 이용한 in-vivo 모델을 사용하여 더욱 견고하게 확인되었습니다. 또한, 이러한 화합물들의 3CLpro 및 PLpro 에 대한 억제력은 in-vitro 실험 키트를 사용하여 평가되었으며, 이후 소개된 새로운 세포 기반 빠른 방법을 통해 추가적으로 확인되었습니다. 마지막으로, 이러한 화합물들의 가시 단백질 유도 염증에 대한 억제력은 in-vitro 및 in-vivo 모델을 사용하여 평가되었습니다. 이 연구에서 우리는 처음으로 갈색

해조류로부터 분리된 폴리페놀 화합물의 SARS-CoV-2 에 대한 억제 작용의 잠재력을 보고합니다. 이러한 결과는 IPA, Dieckol, DPHC 및 Eckmaxol 이 뛰어난 억제력을 보였음을 보여줍니다.